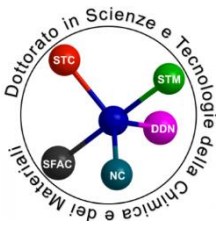

University of Genoa

Doctorate School in Sciences and Technologies of Chemistry and Materials

XXXIII cycle

Ph.D. Thesis

Characterization of advanced materials for low-frequency Vibrational Energy Harvesting (VEH)

Ph.D. candidate

Giulio Paolini

Supervisors

Dr Marco Smerieri

Prof. Luca Vattuone

Table of Contents

1 INTRODUCTION 1.1

2 STATE OF THE ART 2.1

3 VEH WITH MICRO-STRUCTURED ALUMINIUM ELECTRODES 3.1

3.1 ALUMINIUM OXIDE DIELECTRIC LAYERS 3.2

3.1.1 Aluminium samples preparation 3.3

3.2 SAMPLES CHARACTERIZATION 3.4

3.2.1 Characterization techniques 3.4

3.2.1.1 Contact Angle Goniometry 3.4

3.2.1.2 Scanning electron Microscopy (SEM) 3.5

3.2.1.3 X-ray photoelectron spectroscopy (XPS) 3.6

3.2.2 Results and discussion 3.9

3.2.2.1 WCA measurements 3.9

3.2.2.2 Surface morphology 3.11

3.2.2.3 Chemical composition: EDX/XPS characterization 3.12

3.2.2.4 Discussion 3.17

3.3 EXPLOITING MICRO-STRUCTURED ALUMINIUM FOR VEH 3.20

3.3.1 Experimental setup for VEH measurements of Micro-structured Aluminium electrodes 3.20

3.3.1.1 Instrumental apparatus calibration 3.23

3.3.1.2 Magnetic flux effect correction 3.23

3.3.1.3 Beam mechanical resonances and shaker excursion thermal drift 3.24

3.3.2 VEH measurements with micro-structured Al electrodes 3.28

3.3.3 Development of air-tight prototypal device 3.33

3.3.4 Hydrogel drying curves 3.35

3.3.5 Discussion 3.38

4 VEH WITH FLUOROPOLYMER-COATED ELECTRODES 4.1

4.1 PVDF-COATED ELECTRODES 4.3

4.1.1 PVDF 4.3

4.1.2 PVDF solution deposition techniques 4.5

4.1.3 PVDF-coated electrodes preparation 4.7

4.2 FLUOROPOLYMER-COATED ELECTRODES CHARACTERIZATION 4.9

4.2.1 Characterization Techniques 4.9

4.2.1.1 Fourier-transform infrared spectroscopy (FTIR) 4.9

4.2.1.2 Atomic Force Microsocpy (AFM) 4.10

4.2.2 Morphology and Composition 4.11

4.2.2.1 PVDF distribution of phases analysis 4.11

4.2.2.2 Morphological Analysis 4.17

4.2.2.3 Contact angle measurements 4.17

4.2.2.4 Dielectric constant estimation 4.19

4.2.2.5 Discussion 4.20

4.2.3 PVDF on Aluminium foils 4.21

4.2.3.1 Contact angle measurement on PVDF 4.21

4.2.4 PVDF film embedding TiO_2 NPs 4.22

4.2.4.1 Film thickness estimation 4.23

4.2.4.2 ATR FTIR Analysis 4.24

4.2.4.3 Morphological Analysis 4.25

4.2.4.4 Water Contact Angle Measurements 4.28

4.2.4.5 Dielectric constant evaluation 4.28

4.2.4.6 Discussion 4.29

4.3 VEH RESULTS 4.31
4.3.1 PVDF coated electrode with LiCl aqueous solutions at different concentration 4.35
4.3.2 PVDF coated electrode with PAAm hydrogel loaded with LiCl 6.5 M aqueous solution 4.37
4.4 DISCUSSION 4.38

5 PERSPECTIVES AND CONCLUSIONS 5.1

5.1 PERSPECTIVES 5.1
5.2 CONCLUSIONS 5.5

6 BIBLIOGRAPHY 6.1

List of acronyms

AETP: Advanced Engineering ThermoPlastic
AFM: Atomic Force Microscopy
CA: Contact Angle
CE: Contact Electrification
DMSO: Dimethyl sulfoxide
EDL: Electrical Double Layer
EDLC: Electric Double Layer Capacitor
EH: Energy Harvesting
EIS: Electronic Impedance Spectroscopy
ENIG: Electroless Nickel/Immersion Gold
ETFE: Ethylene tetrafluoroethylene poly(1,1,2,2-tetrafluorobutane-1,4-diyl)
EW: Electro-Wetting
EWoD: Electro-Wetting-on-Dielectric
FENG: Fluid Energy NanoGenerators
FEP: Fluorinated Ethylene Propylene
FE-SEM: Field Emission - Scanning Electron Microscopy
FIB-SEM: Focused Ion Beam - Scanning Electron Microscopy
FTIR: Fourier-Transform Infrared Spectroscopy
FTIR-ATR: Fourier-Transform Infrared Spectroscopy - Attenuated Total Reflection
IL: Ionic Liquid
MEMS: Micro Electro-Mechanical System
PAAm: Polyacrylamide
PCB: Printed Circuit Board
PTFE: Polytetrafluoroethylene - Poly(1,1,2,2-tetrafluoroethylene)
PVDF: Polyvinylidene fluoride or polyvinylidene difluoride - Poly(1,1-difluoroethylene)
REWoD: Reverse Electro-Wetting on Dielectric
RTIL: Room Temperature Ionic Liquid
SE*I*: Secondary Electrons of I-type
SE*II*: Secondary Electrons of II-type
SEM: Scanning Electron Microscopy
TE: TriboElectrification
TENG: Tribo-Electric NanoGenerator
VEH: Vibrational Energy Harvesting
WCA: Water Contact Angle
WSN: Wireless Sensor Network
XPS: X-ray Photoemission Spectroscopy

Abstract

Nowadays, sensors are among the most exploited systems in everyday life, with several applications stimulating an increasing amount of research. They generally require external power, thus adding issues such as periodic maintenance and size constraints. A novel technique for energy harvesting (EH) from mechanical vibrations is the Reverse Electrowetting on Dielectric (REWoD). It can provide high power density by exploiting the mechanical modulation of the capacity at the liquid/dielectric interface attaining, without any external bias, power densities of ~μW/cm^2. Compared with other vibrational EH (VEH) techniques, REWoD harvests energy efficiently even from very low-frequency vibrations (< 10 Hz, human motion), and it is one of the most promising technologies for miniaturization. Low-cost materials have been exploited in feasibility and proof-of-concept study for a portable VEH device, using highly hydrophobic Al oxide and PVDF coated electrodes combined with polyacrylamide (PAAm) hydrogels loaded with LiCl solutions. The morphology at the submicrometric scale and the composition of outmost Al oxide layers have been studied as a function of the chemical etching time and correlated with the surface wettability. The etched Al surfaces exhibit binary structures with nanoscale block-like convexes and hollows, providing more space for air trapping. The analysis shows that the change in wetting behaviour correlates with the amount of Al hydroxide at the surface and confirms the essential role of the adsorption of airborne carbon compounds. The hydrophobic behaviour depends, therefore, on the combined effects of surface morphology and surface chemical composition. Alternative PVDF coated Al electrodes have been tested to mitigate the degradation of the hydrogel over time due to the microstructure of the external oxide layer. PAAm hydrogels show no more degradation over time while providing peak power at frequencies lower than 10 Hz for a single hydrogel of ~0.6 μWatt, higher than the ~0.25 μWatt, obtained by using the Al oxide electrodes.

1 Introduction

In the last decades, sensors, either stand-alone or connected in Wireless Sensor Networks (WSNs), are one of the most pervasive technologies in nowadays life [1] and their use is getting everyday more widespread, especially because of nowadays efforts in developing smart cities and Internet of Things (IoT) technologies. The simplicity in both configuration and maintenance allows for such intense usage, and when organized in WSNs, they can reach levels of data processing hitherto unknown, opening a vast scenario of highly enhanced process control and management, and providing at the same time an incentive into improving existing sensors and increase their operational range. Accelerometers represent one of the most common examples of sensors, and they are widespread in several fields, such as automotive, wearable devices, communications, and environmental monitoring. Their response is generated by the movement of a mass, linked to a spring (or a likewise elastic element), when it is accelerated: the inertial mass position over time is determined by a sensor which converts the analytical signal represented by the mass displacement into an electrical signal [2]. A first-approach classification is thus dependent on the kind of sensor dedicated to measure the position of the inertial mass:

- **Strain Gauge Accelerometers:** they exploit the variation of electrical conductivity of a strain gauge due to a change in its geometrical properties. In such devices, an inertial mass is put at the free end of a cantilever beam, while the other end is fixed at the instrument housing with two bounded strain gauges mounted on it. When the mass is forced to move after a stress, it bends both the cantilever and thus the strain gauges, causing their resistance to change in a way that is proportional to the acceleration sensed by the mass. They are quite cheap and sensible but cannot compete in accuracy with other force sensors, like piezoelectric ones, and they are limited in frequency response. Furthermore, they require calibration after installing, and their output is strongly affected by a change in temperature of the strain gauges. Instead of using strain gauges, it is also possible to exploit piezoresistive material.
- **Piezoelectric Accelerometers:** In this category of force sensors, the seismic mass is directly mounted on a piezoelectric element which also works as elastic element and generates a voltage when compressed by the mass motion. There are two types of piezoelectric materials for accelerometers: single-crystal materials like for instance quartz, and ceramic materials like barium titanate and lead metaniobate. The formers are better from the perspective of sensitivity, because of their higher piezoelectric constant, and are less expensive to fabricate, but have the disadvantage of a much shorter operativity life span. Piezoelectric-based accelerometers show an extremely high frequency response (as an example, strain gauges show flat response up to above 200 Hz, whereas piezoelectric reach 10.000 Hz), however, because of the low output signal and high output impedance, they require an amplifier/impedance converter to operate properly.
- **LVDT Accelerometers:** in this case the mass displacement sensor consists of a Linear Variable Differential Transformer, which consists of three solenoidal coils placed next to a tube, a primary one near its centre and two secondary ones near each end of the tube, which hosts a ferromagnetic core working both as inertial mass and as motion sensor. The primary coil is driven by an alternate current, causing a voltage, proportional to the distance of the secondary coil from the position of the ferromagnetic core, to be induced in the secondary coils. Thus, as the ferromagnetic core position changes, the induced voltages in the secondary coils change accordingly, and since the two coils are connected the whole output is the differential of the voltages registered by the secondary coils.

- **Capacitive Accelerometers:** here the seismic mass, suspended over a relatively rigid elastic element like a membrane, consists of a conductive material, and acts as one of the plates of a parallel-plates capacitor (the other is in a set position within the device). In this configuration, inertial mass motion is determined by the variation in the system capacitance occurring in response to changes in distance between the plates. Because of their low fabrication cost, high sensibility, and reduced sizes, they dominate the automotive and consumer electronics markets.
- **Laser Accelerometers:** for purposes in which an extreme accuracy is required, this category of accelerometers works thanks to a laser interferometer which determines the inertial mass position in time, and the relative acceleration is then calculated by a dedicated computer. They are quite expensive and large and must be fixed on ground or on a stable base to operate properly, thus strongly limiting their applicability.
- **Gravitometers:** a special category of devices dedicated to local gravitational field measurements. Since gravity and acceleration effects are the same, an accelerometer is unable to distinguish them: for instance, if a vibrational noise would affect a measurement, this contribution would remain hidden within the signal output. In the case of gravitometers, those spurious effects are counteracted by very effective suppression of vibrations and by suitable signal processing.

  All the accelerometer typologies shown hitherto require an external power supply to operate (for piezoelectric-based devices, power supply is needed at least for the amplifier/impedance converter), generally provided by batteries. However, this implies maintenance issues as well as size constraints when designing force sensors; a feasible solution to this problem is exploiting the sensor itself as its own power source, by converting the vibrational energy into electrical power. The latter solution obviously implies relevant issues related to Energy Harvesting (EH). The main techniques to transduce mechanical motion into electrical energy can be enlisted as follows [3]:
  - **Electromagnetic EH:** such technique relies on the electromagnetic induction generated by oscillating a magnet, linked to a spring, near a coil whose ends may collect the electromotive force induced by the magnet motion. To optimize the efficiency of electromagnetic energy harvesters, large magnets and coils are needed, meaning that although this technique is quite interesting on the energy generation point of view, it shows significant scalability drawbacks.
  - **Piezoelectric EH:** piezoelectric effect results into electric charge accumulation, within a solid material, in response of a mechanical strain. The reverse process also occurs, meaning that piezoelectric materials generate internal stresses in response of an electrical field. Since this charge accumulation arises at opposite sides in the piezoelectric element, it is possible to connect it to an external circuit, thus harvesting the electric energy relative to a change in piezoelectric element sizes. Generally, piezoelectric material are rigid crystals with high resonance frequencies (> 1 kHz), and their transduction efficiency is quite low, yet they are used even for low frequency EH, by using very large piezoelectric elements (as for example, in sidewalks to collect the energy from human steps).
  - **Magnetostrictive EH:** magnetostrictive effect is the strain of a ferromagnetic material, due to an external magnetic field, along the field direction (on this regard it could be considered as the magnetic version of piezoelectricity). The opposite of such effect, known as Villari effect, is exploited in magnetostrictive EH: after a mechanical strain, alignment of the ferromagnetic domains within the magnetostrictive element produces a built-in magnetization, thus transducing mechanical energy into magnetic energy: cyclic mechanical stress applied to magnetosctrictive material leads to a cyclic magnetization. Since this effect is obtained over time because of Faraday-Neumann induction law, a coil wound around the magnetostrictive

element experiences an induced voltage, which is proportional to the cycling frequency. Such energy is then converted into electrical energy thanks to the coupling with the external electrical circuit. The impedance of magnetostrictive Eh is quite low making this technique quite efficient into transducing mechanical energy [4]; unfortunately, miniaturizing such technology to integrate it in microelectronics is still an issue.

- **Electrostatic EH:** here, energy collection is obtained by exploiting the unbalance between variable capacitors, which produces a voltage proportional to the change in the capacitance of the system. In the case of a parallel plate capacitor, the capacitance C may be expressed as

$$C = \frac{\varepsilon A}{d}$$

Eq. (1.1)

where ε is the dielectric constant of the dielectric medium between the plates, A is the overlap area between the plates, and d the separation distance between them. From such expression, it is straightforward to observe that capacitance changes when changing the geometrical properties of the system, namely the separation distance d and the overlap area A, as shown in Figure 1.1.

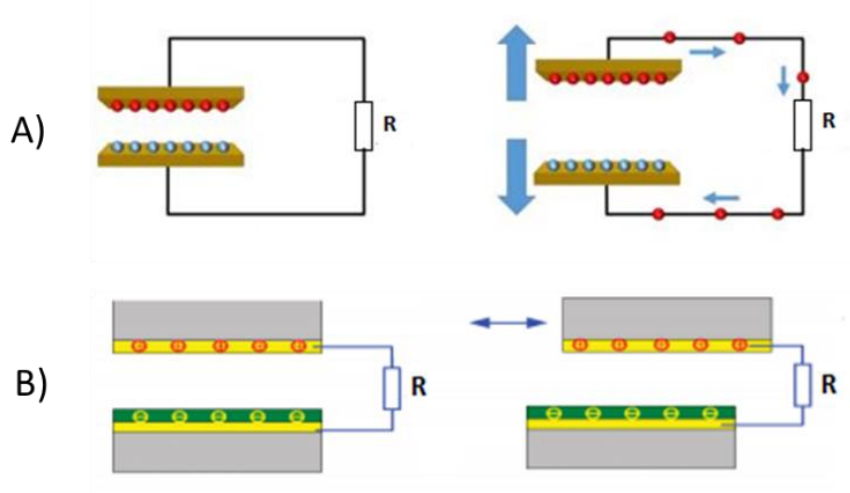

Figure 1.1 – Examples of Electrostatic EH. In A) the capacitance is changed by tuning the separation between the plates (in the right panel, electric current is depicted), in B) same result is achieved by tuning the plates overlapping area.

According to the general definition of capacitance, namely

$$C = \frac{Q}{V}$$

Eq. (1.2)

where Q is the charge amount stored within the capacitor, V is the electric potential. Since charges are unable to move, Q is constant: a change in system capacitance leads thus to a variation in the electric potential V, causing a current exploitable by an external circuit. A widespread implementation of electrostatic energy harvesters in several technologies is likely thanks to their low costs, long lifetimes, and to the possibility of integrating them in Micro Electro-Mechanical Systems (MEMSs).

In this PhD activity, quite recent techniques for harvesting low frequency vibrational energy are exploited to develop a self-powered accelerometer. These techniques involve the methods of TriboElectrification (TE) as well as the mechanical modulation of the interfacial area of Electrical Double Layers (EDLs), exploiting them both as bias source and EH elements.

TE is a long-time known, and yet poorly understood phenomenon, in which charge redistribution occurs between two originally uncharged materials, with different electrical properties, by means of

friction, and can be considered as due to the concomitant contribution of tribology and Contact Electrification (CE) processes [5]. The latter is an actual physical effect, in which two different materials develop a charge separation at their surface when brought into contact. Even though CE represents one of the most fundamental processes at any interface, a complete knowledge on its mechanism and the exact nature of the charge transfer is still lacking, not only because it is complicated by the concomitant friction process, but also because it occurs for all condensed phases, making quite difficult to generate a single model capable of describing CE. In recent years, a strong interest over TE-based EH (see further below) led to several studies on CE-related charge transfer [6]: Xu et al. [7] determined that in the case of solid-solid CE, charge transfer is mainly, if not entirely, ruled by electron transfer, and also that an energy barrier is associated to the release of the tribocharge induced at the surface. Modified surface states models, in which the presence of surface or defect states in between valence and conduction band is postulated, were then proposed to describe the CE mechanism for metal-insulator and insulator-insulator interaction, as depicted in Figure 1.2: here, metal electrons are conformed to Fermi-Dirac distribution, implying a certain population at $E>E_F$ at a temperature T_1 higher than absolute zero (Figure 1.2a). At contact such electrons can transfer into the dielectric surface states (Figure 1.2b), and at separation (Figure 1.2c) the resulting charge redistribution would produce an electric field, causing some of the electrons (e.g. those at $E>E_F$) trapped within the surface states to flow back into the metal (Figure 1.2d). In case of very high temperature, for most of the trapped electrons would be quite simple to be released from the dielectric.

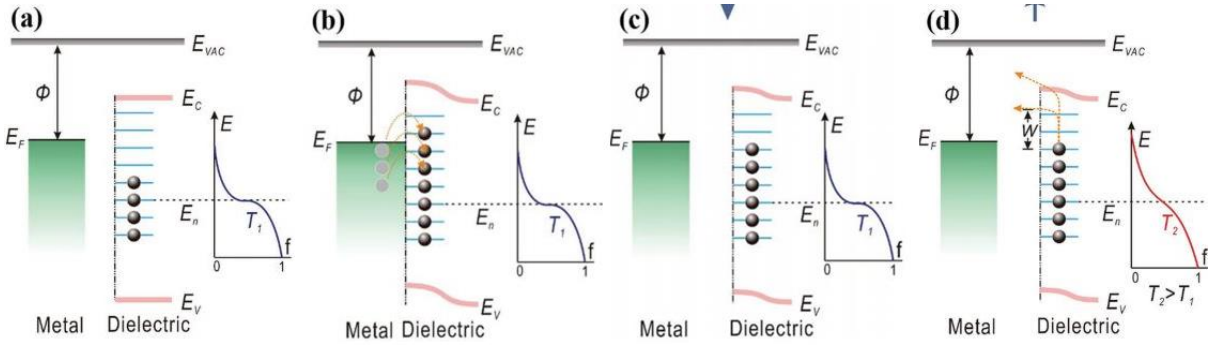

Figure 1.2 – Modified surface states model for explaining the charge transfer during and after CE for the case of metal-dielectric (semiconductor). The CE for a metal and a dielectric a) before contact, b) in contact, and c) after contact. d) Charge release. Φ, metal work function; E_F, Fermi level; E_{VAC}, vacuum level; E_C, conduction band; E_V, valence band; En, neutral level of surface states; f(E), Fermi–Dirac distribution probability; W, potential barrier; T1 and T2, temperature. Images and captions taken from [7].

This model is consistent with the fact that the tribocharge detected at the dielectric surface has a decay consistent with the thermionic emission law, and also that the tribocharge is electron-transfer related (since ions follow Boltzmann's distribution, an increase in the temperature would have produced an increase in the detected tribocharge); however, such models cannot be applied for polymers or composite materials [6]. A more general mechanism has then been proposed by Wang [6] and shown in Figure 1.3: here, electrons are considered localized into specific atomic or molecular orbitals. When two atoms are forced to approach at smaller distances than their bond length, the electron clouds overlap causes their electronic structures to "merge" into a single asymmetric double potential well, which allows electrons from one species to occupy energy levels at lower energy of the other species (such transition would imply the release of a photon, a feature yet unverified). At separation, some of the charges may be released, depending on the thermal energy.

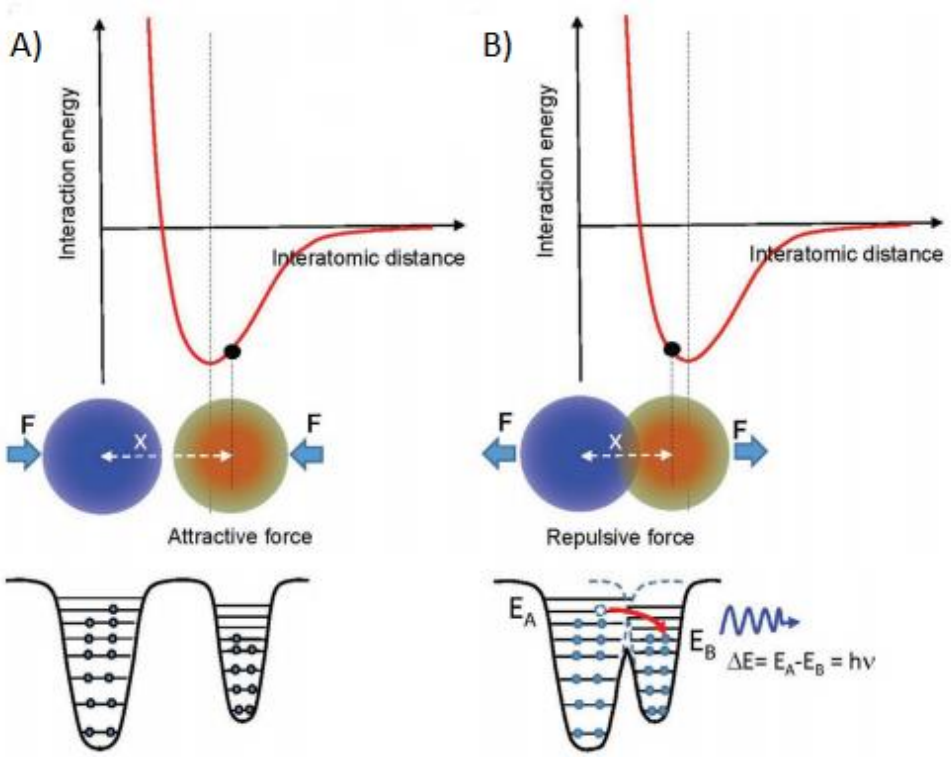

Figure 1.3 – Schematics of the Wang Transition occurring during CE. Upward the interatomic interaction potential for 2 different atoms is shown, in the case A) the atoms are at distances longer than their bond length, and B) when forced at distances shorter than their bond length. Below, the potential energy well model of the atoms is shown, for the same cases. Image taken from [5].

The solid-liquid case is more complicated instead, since both electron- and ion-transfer affect the CE phenomenon: Lin et al. [8] were able to distinguish those two contributions to the surface charge induced during CE between ceramic surfaces and aqueous solutions, and determined that the first is related to electron-exchange between liquid and solid, the latter refers to surface reactions producing ionic species. They also found that ion-transfer is dominant for hydrophilic materials, whereas CE over hydrophobic materials is ruled mostly by electron-transfer (see top panel of Figure 1.4); in both cases an increase of the electron-transfer contribution with an increase of the Water Contact Angle (WCA) is observed, but this increase is remarkably stronger for hydrophobic materials, suggesting that materials with low WCA allow for stronger interactions with water, making the surface ionization reactions more likely to occur. Further, it was also observed that CE charge transfer polarity is not always the same, but is strongly material dependent, as shown in the bottom panels in Figure 1.4: when contacted with deionized water at room temperature, MgO contemporarily acquires positive ions and electrons at the same time, whereas AlN acquires negative ions and loses electrons, suggesting that the two charge transfer phenomena are independent of each other.

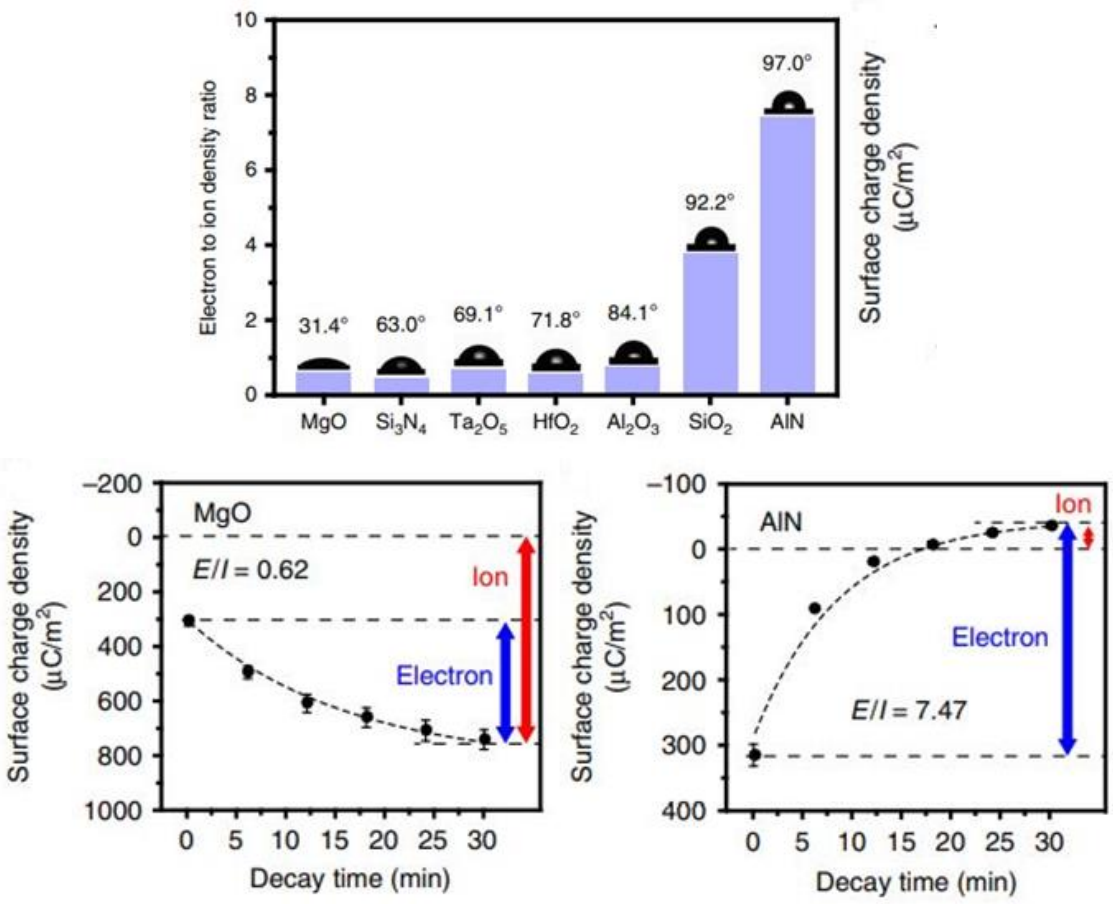

Figure 1.4 – Top panel shows the ratio between electronic and the ionic contributions to CE-related surface charge for several insulators contacted with deionized water at room temperature as a function of surface wettability (expressed by their WCA). Bottom panels show in detail the CE measurements for MgO and AlN respectively. Images taken from [8].

CE is considered to play a major role in the formation of Electric Double Layers (EDLs). Also known as Electric Double Layer Capacitors (EDLCs) because of the model used to describe them, EDLs are charge accumulations arising at surfaces when exposed to a liquid (commonly, electrolytic solutions) and are generally formed by negative charges adsorbed at the surface from the solution and inducing a layer of counter-ions in the liquid nearby [9].

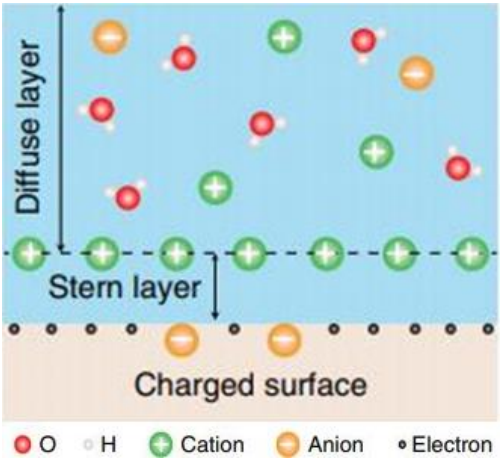

Figure 1.5 – Basic EDL schematization. Image taken from [8].

As shown in Figure 1.5, EDLs can be quite naively schematized as composed by three layers, namely (*i)* the charged surface, (*ii)* a Stern Layer of fixed counter-ions, and (*iii)* a Diffuse Layer of free ions, in which the co- and counter-ions concentrations gradually reach the values of the bulk solution, because of a competition between coulombian forces and thermal motion. More advanced models take into account the possible presence of co-ions already in the layer next to the surface [10], or ion hydration shell effects [11]; extended models to take into account EDLs arising at electrode/electrolyte interfaces in case of biochemical/biological solutes also exist [12]. Generally, the formation mechanism is considered to involve just the adsorption at the solid surfaces of ions from the solution, which then induces a shell of counter-ions. Wang et al. [6] proposed, on the contrary, a two-steps mechanism to describe EDLs formation: when a liquid gets into contact with a "virgin" (*e.g.* not tribocharged) surface, its molecules and ions will impact onto the surface, the local pressure generates an electron-transfer process due to the overlap between electron clouds (ion-transfer happens as well at this phase). In the second step, ions with opposite charge with respect to the surface migrate towards the latter, generating thus the EDL.

In the last decade, a rapidly increasing interest has been devoted into developing TE and EDLC based devices, as sensors as well as Vibrational Energy Harvesters (VEHs), not only because of harvestable powers, that may reach even 10^3 W/m^2 depending on the technique and geometry exploited (see further below), but also for the scalability of involved techniques (allowing for integration into wearable devices) and for its possible impact in the field of renewable energies (allowing to harvest energy just from water droplets).

2 State of the art

From the studies conducted by Lippmann [13] in 1875, it was discovered that it is possible to alter the capillary climb of mercury by applying a voltage between mercury and an electrolytic solution. Such effect, initially named electrocapillarity, was believed by Lippmann to be due to a change in the solid/liquid interfacial tension γ_{SL} caused by the extra charge induced in the system upon the voltage application. In further studies [14] the effect was instead named Electro-Wetting (EW), e.g. the change in the wettability of a conductive surface when the Water Contact Angle (CA) is modified by appling a voltage between the surface and the water droplet. However, voltage applications up to few hundred millivolts caused electrolytic decomposition of the solution, making EW hard to exploit in practical applications [15]. Berge [16, 17] overcame such limitation in 1990 by just inserting a thin dielectric film between metal and electrolytic droplet, as shown in Figure 2.1.

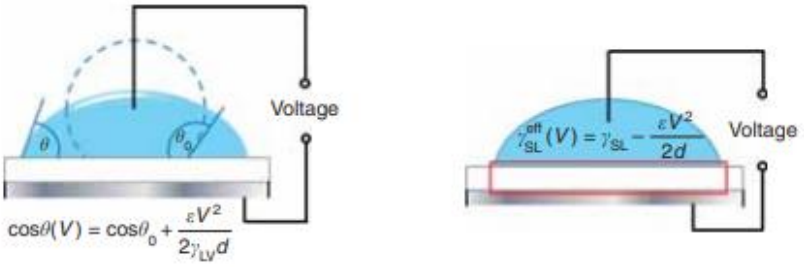

Figure 2.1 – On the left, schematic representation of EWoD principle with its governing equation. On the right, a schematization of the process according to the effective-capacitance model, in which the dielectric layer is schematized as part of the interface. Image taken from [18].

This method, named Electro-Wetting-on-Dielectric (EWoD), allows to increase applied voltages up to values of hundreds of millivolts. Berge also gave EWoD governing law, known as Lippmann-Young equation:

$$cos\vartheta(V) = cos\vartheta_0 + \frac{\varepsilon V^2}{2\gamma_{LV} d} \qquad \text{Eq. (2.1)}$$

where ε is the dielectric constant of the dielectric film, V the applied voltage, γ_{LV} is the liquid-vapor interfacial tension and d is the dielectric film thickness. Here, the last term in right member is called Electrowetting Number and expresses the ratio between the applied electrostatic energy and the system liquid-vapor interfacial tension [19]. Eq. (2.1) may be derived by many approaches, based on different working principles; the most widely accepted are the thermodynamic approach, the energy minimization approach, and the effective-capacitance approach (see Figure 2.1); in this latter approach the dielectric film is modelized as part of the interface and its two sides, namely those facing electrode and droplet, as capacitor plates. Ever since the '90s, applicative studies over the EWoD principle entered a phase of rapid development: as an example, liquid microlenses [20, 21] are recalled, which exploit EWoD for tuning focal length. EWoD-based devices were also developed in the fields of electronics [22, 23], biomedicine [24, 25], chemistry [26], and more recently, in devices designed for EH. Indeed, in 2011 Krupenkin & Taylor [27] proposed a novel mechano-electrical transduction method which exploited EWoD in a reverse fashion, thereby named Reverse Electro-Wetting-on-Dielectric (REWoD) by its inventors. By means of connecting a conductive liquid and a dielectric-coated electrode to an external circuit which applies a constant voltage, and mechanically forcing the liquid to change its contact area on the electrode, a variation in the capacity at the liquid/electrode interface produces an excess charge on the external circuit, and thus a harvestable current. Krupenkin & Taylor proposed

three different working geometries for liquid actuation, namely (a) electrode vertical vibration, (b) electrode lateral shear, and (c) in-channel droplet movement, respectively presented in Figure 2.2.

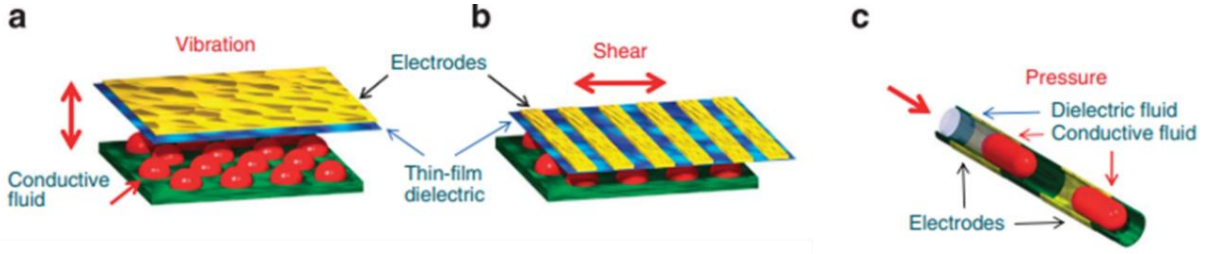

Figure 2.2 – The three working geometries for REWoD EH proposed by Krupenkin & Taylor, namely (a) electrode vertical vibration, (b) parallel shear, (c) pressure-driven microfluidic channel actuation. Image taken from [27].

By using a quite simple analytical model, schematizing the liquid/electrode interface as a variable-capacitor, and while neglecting negative influences on energy generation due to the wetting/dewetting process (such as contact line hysteresis and charge trapping in the dielectric) a theoretical power generation proportional to the square of bias voltage, as well as to the capacitance relative at the maximum liquid/electrode interfacial area, is obtained [27]:

$$P = \frac{5}{4} V_{Bias}^2 C_0 T^{-1} [1 - \tanh\left(\frac{1}{2}(1 - \log(\omega R C_0))\right)]$$

Eq. (2.2)

where V_{bias} is the bias voltage, $C_0 = \varepsilon_0 k A h^{-1}$ is the maximum capacitance of the REWoD unit, A is the maximum droplet/electrode overlap area, h is the dielectric film thickness and k its dielectric constant, and $\omega = 2\pi T^{-1}$ is the capacitance oscillation frequency, with T its characteristic period, and R the load impedance. By means of conductive liquids like mercury or Galinstan™ and combining thin dielectric films of Ta_2O_5 (for high dielectric properties that enhance the interfacial capacitor) and Cytop™ (a highly hydrophobic fluoropolymer exploited to mitigate contact line pinning), power generations of about 10^2 W/m^2 were observed on single droplets in the vertical vibration geometry, and a theoretical harvestable power of 10^3 W/m^2 is expected from devices exploiting REWoD. Subsequently, Moon et al. [28] demonstrated an analogous method for AC power generation by means of plain water as liquid droplets and without the need of external voltage supplier. The contact of water over an electrode generates an EDL at that interface, and when this system is sandwiched by another electrode, coated with a dielectric layer, a minor part of the charge accumulated on the water/electrode interface flows at the water/dielectric interface. If such system is connected to a resistor, it can be described by the circuital scheme proposed in Figure 2.3A, in which the two interfaces are modelled as EDLCs connected in series. The relative capacitances at interfaces formed by the liquid bridge with the electrodes are assumed to scale proportionally with the contact areas, namely:

$$C_T(t) \cong \varepsilon_0 A_T(t) \left(\frac{d}{\varepsilon_p} + \frac{\lambda_D}{\varepsilon_d}\right)^{-1} \cong \frac{\varepsilon_0 \varepsilon_p}{d} A_T(t)$$

Eq. (2.3)

$$C_B(t) \cong \frac{\varepsilon_0 \varepsilon_d}{\lambda_D} A_B \cong constant$$

Eq. (2.4)

where ε_p, ε_d are the dielectric constants of PTFE and water droplet respectively, λ_D is the Debye length expressing the width of charge layer accumulated at the top interface, and d is the dielectric film thickness, A_T and A_B are the top and bottom interfacial area, respectively. In this case $d/\varepsilon_p >> \lambda_D/\varepsilon_d$,

allowing for the approximation made in Eq. (2.3) to be valid, and since bare Indium Tin Oxide (ITO) was used for the bottom electrode, A_B is nearly constant because of water contact line pinning, whereas an appreciable variation of A_T when mechanically modulating the water bridge is achieved by covering the top electrode in a thin hydrophobic PTFE layer.

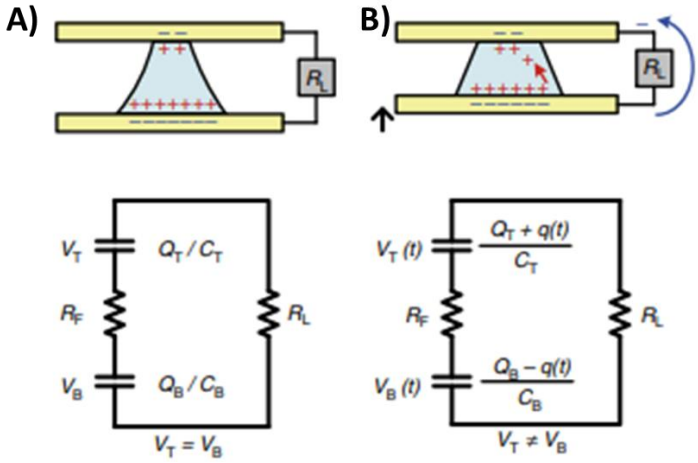

Figure 2.3 – Schematic diagram of the EH unit (above) and its corresponding circuit model (below), as proposed by Moon et co-workers. In A) the system is shown at its equilibrium, in B) is shown the system when an external force causes the electrodes to approach one another, thus changing the contact area at the top electrode. Taken from [29].

A simple resistor-capacitor model is used to describe the system, so that the equivalent electric circuit is expressed by a non-linear differential equation:

$$(R_L + R_F)\frac{dq(t)}{dt} = V_B(t) - V_T(t) = \frac{Q_B - q(t)}{C_B} - \frac{Q_T + q(t)}{C_T(t)}$$

Eq. (2.5)

where R_L and R_F are the load and liquid bridge resistances, respectively. In the stationary case V_B=V_T, and no current flows on the external circuit; as the vibration starts, $C_T(t)$ increases (decreases) accordingly when electrodes are approaching (departing), causing $V_T(t)$ to decrease (increase), thus producing a voltage difference $\Delta V(t)$ across the electrodes in order to relax EDLCs unbalance. If the system is oscillated at a certain frequency *f,* EDLCs at the interfaces will mutually charge and discharge in different phases of the oscillation period, thus causing a collectable alternate current to flow in the external circuit. Such process is described by a dimensionless relaxation time

$$N = \frac{2\bar{\tau}}{T}$$

Eq. (2.6)

where $\bar{\tau} = \frac{1}{T}\int_0^T \mathrm{RC(t)}$ with $C(t) = (1/C_B + 1/C_T(t))^{-1}$ and $R = R_L + R_F$. The relaxation is the charge exchange process between the two capacitors: when the ratio between the circuit time constant and the half-vibration period is low, so that $\tau \ll T/2$ and $N \ll 1$, the system has enough time to re-equilibrate itself, implying low $\Delta V(t)$ across the plates and thus low harvestable currents on the external circuit. As $\tau \gg T/2$, no time is given to the system to relax completely, and power generation is increased accordingly. Electrical power expresses the electrical energy transmitted by a circuit per unit time, and it is measured in Watt (W). In Moon's work, from a 40 µl water droplet average electrical power in the order of tens of nW could be harvested, and 1.5 µW with a power density of 0.3 µW/cm^2 were measured with a load resistance (R_L) of 10 MΩ at 30Hz by using an array of 25 water droplets, corresponding to about 1ml of water. Such values cannot match powers harvested in [27], but were achieved without external bias, making this technique viable for developing self-powered electronics;

at the same time, as remarked by the author itself its operativity is limited by i) the capillary length of water, namely the maximum radius at which the droplet maintains hemispherical shape, which implies a constraint on droplet size, ii) the evaporation of the liquid, and iii) the vibration frequency, since at high frequency hydrodynamic effects cause deformations of the water droplet.

This novel technique immediately attracted much interest, and many tried to overcome the limitations expressed by Moon et al [28, 29]: Kong et al. [30] attempted to exploit Ionic Liquids (ILs) for the liquid bridge. Discovered in 1914 by Paul Walden, Ionic Liquids (ILs) are liquid mixtures of ions only, mainly consisting of organic ions, and became a major area of research in chemistry starting from the end of the XXth century, not only because of their wide range of fascinating properties, but mainly because of the possibility to combine different ionic species, allowing for the synthesis of several classes of ILs, each suited for specific purposes. In ref. [30] Room Temperature Ionic Liquids (RTILs) were chosen since they show relatively good stability from electrochemical perspective, non-toxicity, and most important of all, they are highly inert to evaporation and remain liquid in a wide range of temperature.

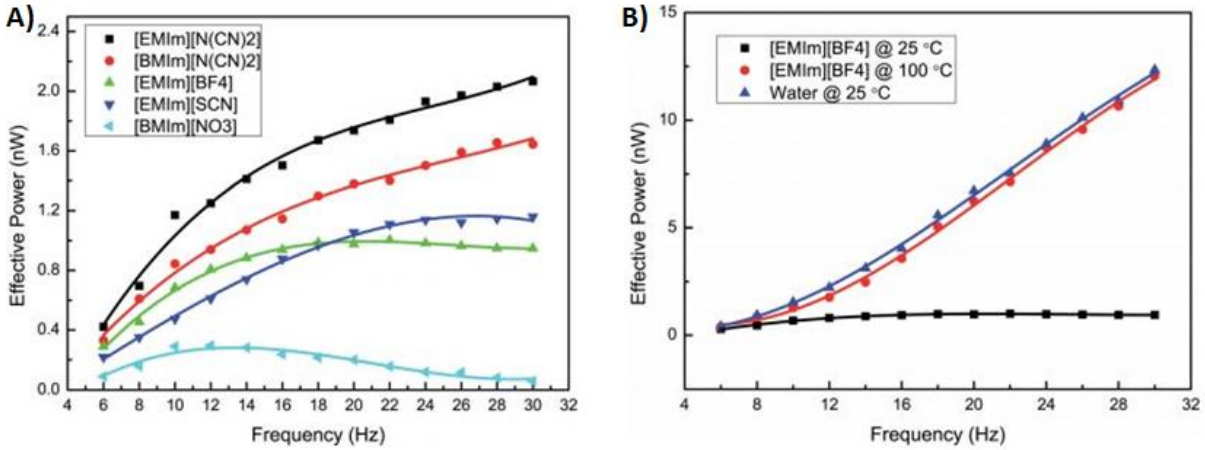

Figure 2.4 – A) Effective power vs vibration frequency for several common ILs, taken at room temperature, load resistance R_L=30 MΩ, vibrational amplitude L=0.35 mm, and liquid bridge volume 15 μL. Dots refer to experimental data, the solid lines refer to fitted results. B) Comparison of power outputs for [EMIm][BF_4] and water liquid bridges volume, taken at R_L=30 MΩ, L=0.35 mm. Images taken from [30].

Figure 2.4A shows power generations as a function of vibrational frequency for several Imidazolyum-based ILs. Measured powers are in the range of nanoWatt units, and data show good agreement with the electrical circuit model (represented by the solid lines): power output increases as a function of the charge density at the top interface, which in the specific case of ILs liquid bridge is strongly related to the structural properties of the ionic species involved and the IL viscosity, as shown by the comparison between [EMIm][$N(CN)_2$] and [BMIm][$N(CN)_2$]. At parity of anionic species, the shorter alkyl chain of the EthylMethyl-Imidazole with respect to that of the ButhylMethyl-Imidazole allows for greater charge storage at the top interface, and at the same time, reduces liquid viscosity. In Figure 2.4B a comparison between water and IL liquid bridges is offered, showing that power outputs are comparable, especially when the IL bridge operates at high temperature, because of a reduced ion association within the IL when increasing the temperature [31], and the temperature-dependant viscosity reduction.

To overcome the evaporation issue addressed by Moon, hydrogels and ion gels were proposed as a replacement for the liquid bridge, namely 3D colloidal systems consisting of a cross-linked polymer network matrix capable of embodying and holding large amounts of water, aqueous solutions and ILs, because of hydrophilic groups in the polymer backbone. In particular, IL and electrolyte based gel,

namely ion gel, were extensively studied in the fields of energy harvesting [32], energy storage [33], sensoristics [34] and wearable electronics [35], for their high ionic conductivity, fast and intense response to a wide range of stimuli, and their biocompatibility.

Wu et al. [36] made a comparison on water-based and hydrogel-based bridges, for EH purposes and as a force sensor, due to the stiffness of the hydrogel, which makes the top electrode/hydrogel system to work as a spring/mass system.

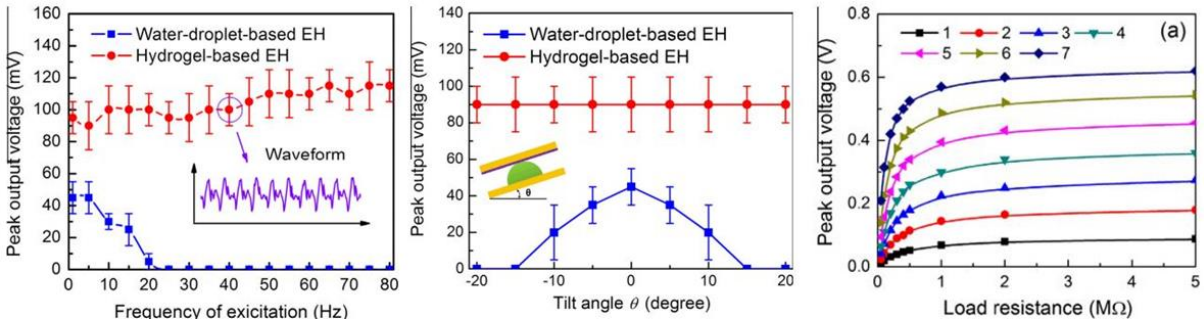

Figure 2.5 – On the left, a comparison of performance for water and hydrogel based EH, as a function of the excitation frequency (inset presents the measured waveform). On the centre, a similar comparison, here as a function of the tilt angle. On the right, a characterization of the peak-to-peak voltage output, as a function of the load resistance R_L, for hydrogel-based EH operated at 60 Hz (inset label indicates the number of hydrogels in the array). Images taken from [36].

In Figure 2.5 are resumed the main improvements introduced by exploiting hydrogels instead of liquid droplets. First, the mechanical properties as well as the limited volatility of the hydrogel allows to extend the operational bandwidth (here, up to 80 Hz) and time [37]. At the same time, an increased voltage output is observed, which is related to an increased variation of the interfacial area ΔA_T at the top electrode when the electrodes vibrate [36]. Also, a characterization of performance as a function of the tilt angle of the system shows that hydrogel-based EH is not subject by the geometrical constraints of water-based energy harvesters, which gradually decrease their operativity when tilted from the horizontal orientation. Further, a demonstration of the scalability effect of this technique is presented in the right panel in Figure 2.5: power outputs as high as 1 µW were measured with a load resistance of 0.1 MΩ, for a 7 hydrogels array under a 60 Hz vibration frequency. For arrays of more hydrogels, such increase in the output was no longer observed, and this was explained by the fact that a slight dispersion of hydrogel size produces a “desynchronization” effect on the output performance.

Recently, Allegretto et al. [38, 39] investigated the transduction mechanism introduced by Moon et al. [28, 29]. Instead of applying Eq. (2.5) for the circuital schemes of Figure 2.3, they rearranged it and derived a linear approximation model in the frequency domain, expressed by:

$$\frac{\boldsymbol{V_{OUT}}(j\omega)}{\boldsymbol{V_{sense}}(j\omega)} = \left(\frac{j\omega R_L C_T^0}{j\omega C_T^0(R_I + R_L) + 1}\right)$$

Eq. (2.7)

with

$$\boldsymbol{V_{sense}}(j\omega) = \boldsymbol{I}(j\omega)(R_I + R_L) + \frac{\boldsymbol{I}(j\omega)}{j\omega C_T^0}$$

Eq. (2.8)

where ω is the angular frequency of the vibration, j the imaginary unit, R_I and R_L the liquid and load resistance, respectively, C_T^0 the capacitance at top electrode at rest, $\boldsymbol{I(j\omega)}$ is the current across the circuit. The model was derived assuming that the variation in top interfacial area (and thus capacitance) during operation small with respect to the value at rest. Such model provides the possibility to determine the relationships between output performance and certain parameters of the EH unit, providing itself useful in designing new energy harvester.

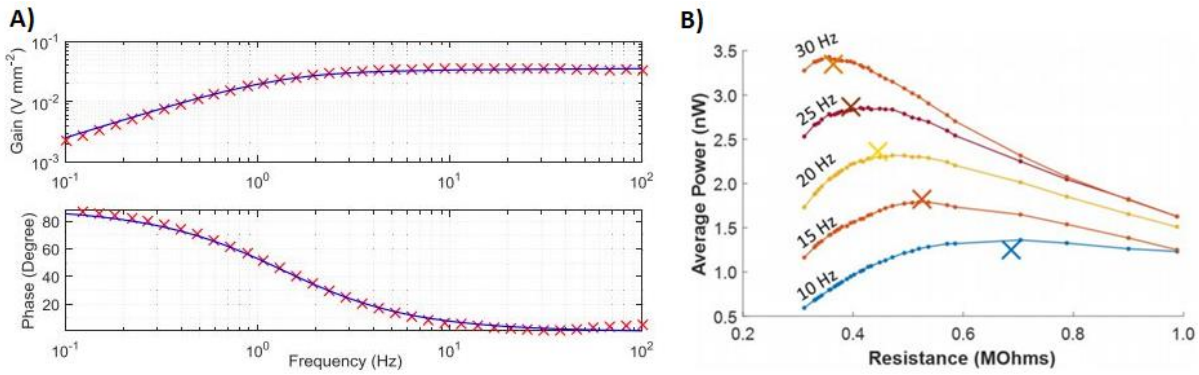

Figure 2.6 – A) Magnitude (upward) and phase (below) response of EIS characterization for a standard transducer with a 40 µL water bridge (as the one shown in fig. 8). Red crosses are experimental results, blue line is the simulated response. B) Average power transfer for a 40 µL as a function of load resistance for different vibration frequencies. Dots indicate experimental results, the crosses indicate the prediction of the Max Power Transfer Resistance according to Eq. (2.10). Images from [39].

This model can estimate the threshold frequency at which the magnitude response stops increasing linearly and flattens, thereby named knee frequency, and the resistance value at which the maximum power is transferred at the load, respectively as:

$$\mathrm{f_{knee}} = \frac{1}{\mathrm{C_T^0(R_I + R_L)}}$$

Eq. (2.9)

$$R_{MaxP} = \sqrt{\frac{1}{(\omega C_T^0)^2} + R_I^2}$$

Eq. (2.10)

As shown in Figure 2.6A, the Electronic Impedance Spectroscopy (EIS) response is in good agreement with the simulated response with the linear model in [38], and the increase in the magnitude of the response was explained by the fact that at low frequencies the change in interfacial area are so slow that the top capacitor can discharge the voltage unbalances on the liquid, leading to small currents flowing across the load resistance. A similar consistency between model and measurements is observed in Figure 2.6B. In Figure 2.7 a comparison between the simulated response for Moon's model

and the one derived by Allegretto [38, 39], showing that models agree until the knee frequency, after which they start diverging quite consistently, especially at high $\Delta A/A_T^0$ where Moon's model predict a linear increase in the signal amplitude, yet to be verified [38].

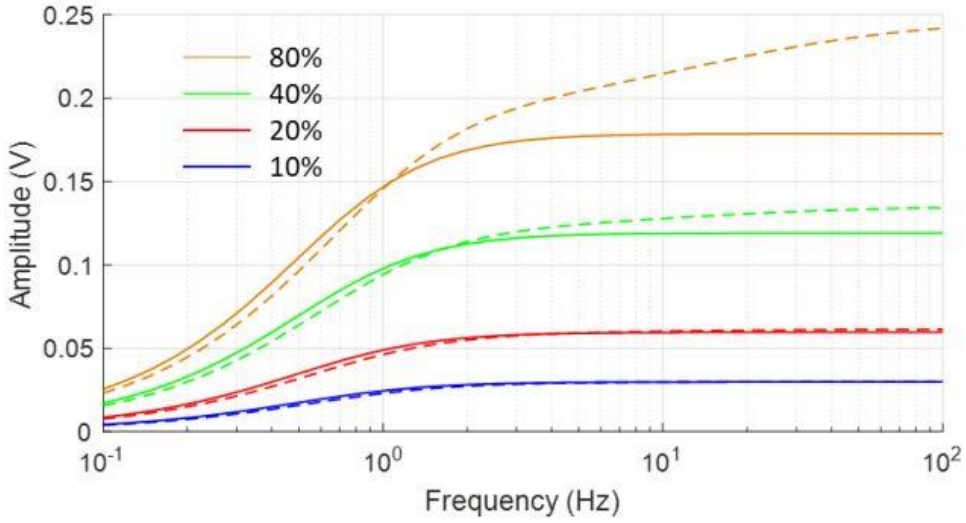

Figure 2.7 – Comparison between analytical model for the signal amplitude in the frequency domain, for different $\Delta A/A_T^0$ ratios, expressing the maximum surface area variation during operation with respect to the value at rest. Dashed line refers to Moon's model, solid line refers to the linear approximation model proposed by Allegretto et al. Image from [38].

Further, Allegretto [38, 39] tried to investigate the origin of the bias voltage, in the attempt to understand whether the self-biasing mechanism proposed by Moon et al. [28, 29], or the PTFE dielectric film coated on the top electrode play a role in the biasing process. Indeed, it is known that PTFE tends to negatively charge at the surface when exposed to aqueous solution [40], and this behaviour is related to the adsorption of hydroxide ions at the surface. By developing an accurate method to measure the charge at the bottom interface, even if he could not confute the EDL theory for the biasing mechanism proposed in [29], he yet found some interesting indications that the PTFE layer actually takes part in the energy harvesting processing. In the left panel of Figure 2.8, it is shown that changing the electrode material or the concentration of the electrolytic solution produces no effect on V_{bias}, which is unexpected in the EDL theory, since both those parameters would affect the capacitance at the bottom interface, and thus V_{bias}. In the right panel, it is instead shown how the pH value of the solution produces a strong effect on V_{bias}, not only on the magnitude but also in the sign. This is an indication that hydroxide concentration in the solution has a prominent role in the biasing mechanism.

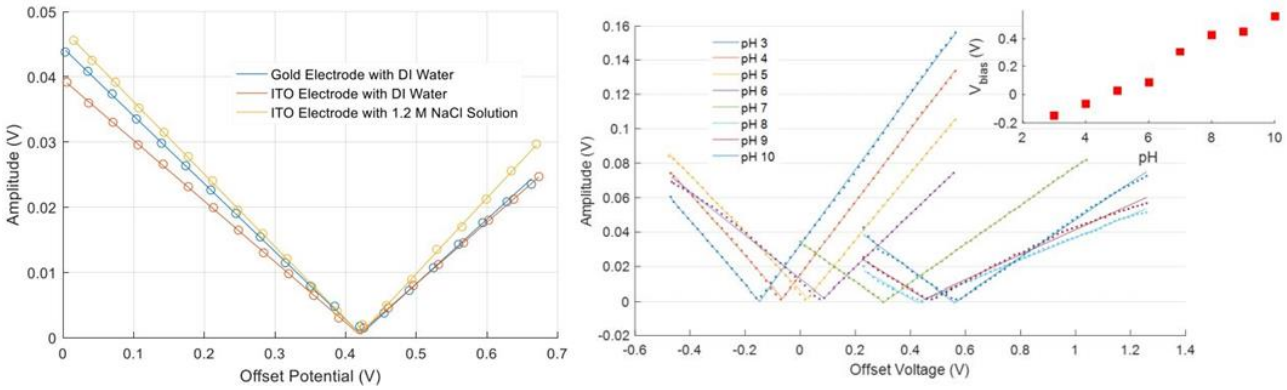

Figure 2.8 – On the left, V_{bias} determination for different liquid bridges and electrodes. On the right, the V_{bias} determination for solutions at different pH (inset represents V_{bias} as a function of pH). Images from [38].

Almost contemporarily to Moon et al. [28, 29], a new class of energy harvesters was introduced, namely Tribo-Electric NanoGenerators (TENGs) [41]. Those devices combine the effects of CE and electrostatic induction [42] and their low-cost and easy fabrication, design versatility, thus making them an excellent tool into harvesting irregular, randomly oriented and distributed vibrations. In Figure 2.9 a schematic representation of the models underneath the four operative modes for TENGs is presented:

a) **Vertical contact-separation (CS):** when brought at contact, the two dielectric materials develop a charge distribution at the surface, which is balanced until the materials are separated. At separation, the tribocharged surfaces will induce a variation in the potentials at their respective electrodes, causing a current to flow on an external load. Since an opposite current would flow when the materials are contacted again, an AC output is obtained in a harvesting cycle. This class of TENGs proves excellent in harvesting energy from cyclic or impulsive motion.

b) **In-Plane Lateral Sliding (LS):** instead of a vertical displacement, the dielectric materials which compose the triboelectric pair are separated by a lateral (e.g., parallel to surfaces interface) displacement, thus the TE process occurs because of rubbing instead of contact. Such displacement produces a potential difference proportional to the mismatched area of the dielectric surfaces. In case a single dielectric is used, the electrode acts as triboelectric material (see Figure 2.9b). Since it works on rubbing instead of contact, it enhances the TE process, allowing such method to be exploited for high-performance TENG design.

c) **Single-Electrode mode:** the system proposed in Figure 2.9c could be schematized as an electrode connected to the ground, with a dielectric layer decoupled from it and allowed to move freely; from a starting position, in which dielectric layer are in contact, a displacement of the latter causes the electrode to behave as a distance-variable as well as area-variable capacitor, whose unbalance with respect to the ground is compensated by a current. The cycle is completed by contacting again the triboelectric pair. Although this method has the lowest energy conversion efficiency of them all, because of electronic screening at the primary electrode [43], it has the advantage that the dielectric layer has no physical restraints with respect to the electrode. This feature makes single-electrode mode TENGs suitable for EH from random oriented and distributed sources of environmental energy, such as air flows [44], rain drop [45], or to be implemented for developing displacement vector sensors [41].

d) **Free-Standing:** this operative mode can be resumed, as shown in Figure 2.9d, as a pair of symmetrical electrodes below a free-standing (thus, not connected to the circuit) dielectric layer, already electrified by a TE process, capable of moving horizontally with respect to them. Such movement produces an asymmetrical charge distribution on the electrodes pair, and thus a voltage drop between them. The main advantages of such design is that provides the highest device durability [46], since the dielectric does not contact the electrodes, and also high energy conversion efficiency; indeed, it was mainly applied for EH [46, 47] and self-powered sensors [48].

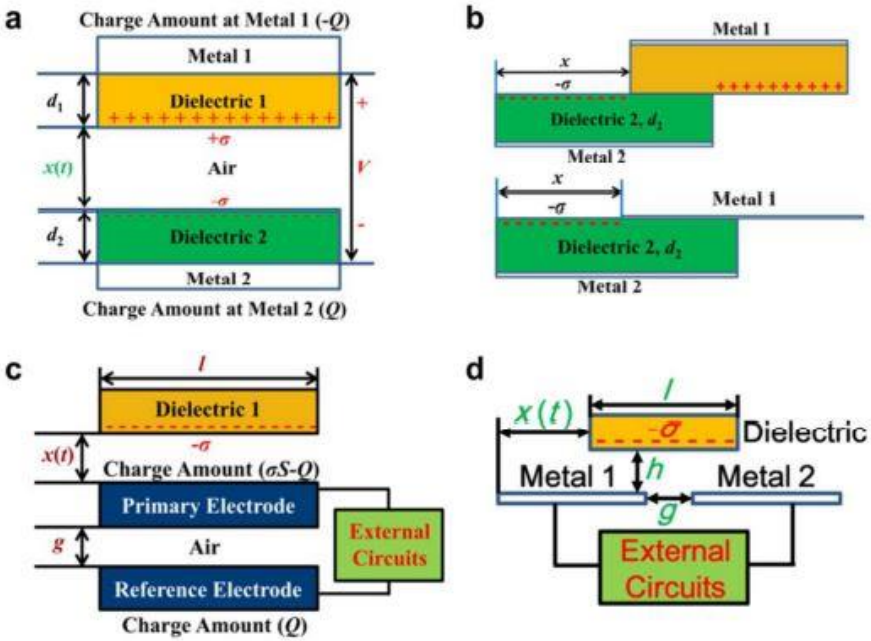

Figure 2.9 – Representation of the theoretical models for TENGs operative modes: a) Vertical Contact-Separation mode; b) In-Plane Lateral Sliding mode, upward the triboelectric couple is formed by two dielectric materials, below by a dielectric and a metal; c) Single-Electrode mode; d) Free-Standing mode. Image taken from [41].

After the works of Krupenkin and Taylor [27] and Moon et al. [28, 29], much interest was dedicated into scavenging energy from water, leading to the creation of a TENG subclass, known as Fluid-based TENGs (FluTENGs) or Fluid Energy NanoGenerators (FENGs) [49], intensively characterized in last years for their applicability in marine environments, due to their excellent behaviour in scavenging irregular and low-frequency vibrations, providing a powerful tool in the fulfilment of the Blue Energy Dream [50, 49], namely the strategy focused into developing large scale power generation networks and WSNs into seas and oceans. In 2014, a single-electrode TENG for drop and flowing water EH was proposed [42]; it was designed to collect both kind of energy a water drop may carry, namely the electrostatic energy related to the triboelectrification occurring when the drop hits the device, and the mechanical energy acquired during its falling down. As shown in Figure 2.10A, such device consists of a Cu thin film electrode supported on PMMA and coated on a thin, superhydrophobic PTFE layer (WCA=169°); the proper nature of the generated triboelectricity was still uncertain, whether it was related to CE occurring between the drop and the air, the pipe walls, or the PTFE dielectric layer. As shown in Figure 2.10B, experimental power output reach values as high as 145 μW for a 5 MΩ load resistance and proved able to collect energy also from flowing tap water [42]. Also, a study on the relationship between the drop falling height and the charge induced at the electrode, and shown in Figure 2.10C: an increase of such charge is indeed observed while increasing the falling height until a saturation in the induced charge occurs at about 20 cm. This confirm that part of the kinetic energy acquired during the fall by the drop is converted into electrical energy via a TE process.

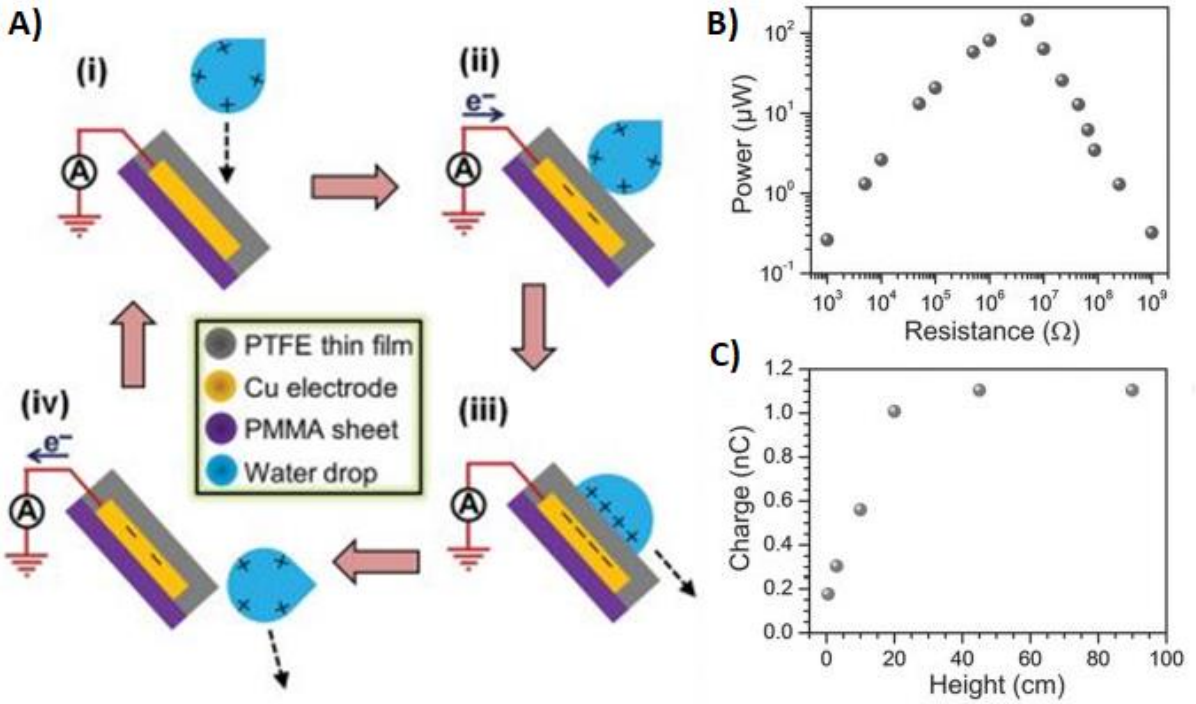

Figure 2.10 – A) Proposed working mechanism for the water-based TENG, assuming the triboelectricity is generated because of CE occurring at the drop when it is released from the dispensing pipe, or by rolling friction with air during the fall. B) Experimental output power as a function of the load resistor, for the water-based TENG, for a 30 μL drop falling from a height of 90 cm. C) Characterization of the influence of the falling height on the charge induced on the water-based TENG. Images taken from [42].

Subsequent studies on FENG focused mainly on water-based TENG, especially on packed structures such as buoyant balls [51], cylinders as well as cubes [52], or even U-shaped pipes [53], for environmental monitoring as well as EH purposes, with harvested powers in the μW/cm^2 range. Nahian et al. [54] conducted a study on Flu-TENGs, in particular comparing vertical contact-separation (CS) and in-plane lateral sliding (LS) operative modes: despite the LS mode was found to induce higher amounts of surface charge with respect to CS mode (see insets in Figure 2.11), the latter was found to generate higher power densities, as high as 212 nW/cm^2, against the 84 nW/cm^2 measured on the LS Flu-TENG. Since such devices exploit TE process, their power outputs are inherently limited by the surface charge the triboelectric couple may develop during the contact. To overcome such limitation, it was tried to couple TENG devices with other technologies, such as piezoelectric [55, 56], electromagnetic [57] or pyroelectric [58] generators. Yu and co-workers [59, 60] found a more exotic solution instead: they created a single-electrode TENG generating a single dielectric layer composed by two regions of different materials (here, Cytop™ and PTFE) and a water droplet as a free-standing electrode. As the droplet slides over the two regions, it triboelectrifies them at their saturation value, and delivers to an external circuit the excess charge induced in the water, proportional to the difference in the induced charge (thus, the difference in the EDLCs the drop forms with the dielectric) at the two dielectric materials, namely:

$$Q = \sigma_C A_C - \sigma_P A_P$$

Eq. (2.11)

where Q is the induced charge, σ is the surface charge density, A is the contact area, and the subscripts C and P refer to Cytop™ and PTFE, respectively. The device proposed in [59] could generate a peak-to-peak voltage of 42 V for a 400 μL water droplet at 0.25 Hz, and 115 V at 2.5 Hz when an external bias of 8 V was applied.

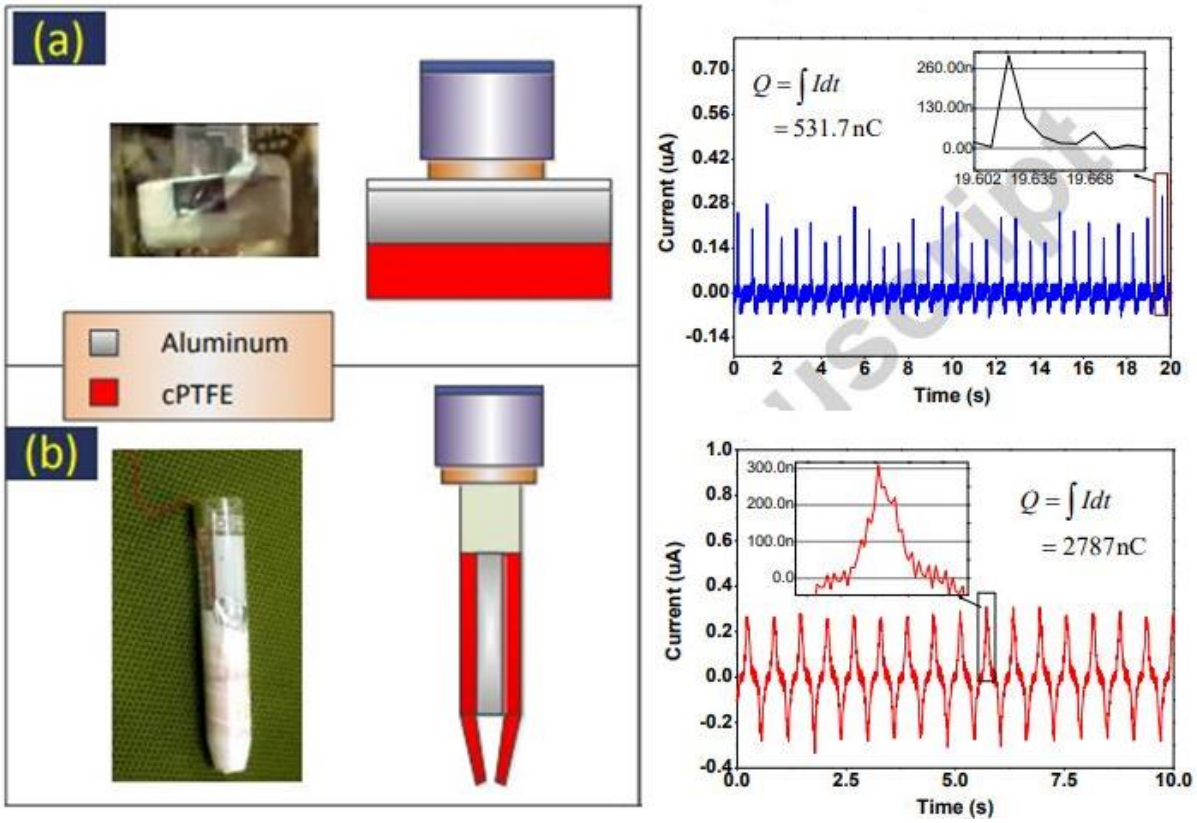

Figure 2.11 – (a) On the left, picture and design scheme for the CS Flu-TENG unit. On the right, its ouput current when contacted with DI water (inset shows the induced surface charge for a single cycle, in this case 586,2 μC/m²). (b) On the left, picture and design scheme for the LS Flu-TENG unit. On the right, its ouput current when submerged within DI water (inset shows the induced surface charge for a single cycle, in this case 995 μC/m²). Images taken from [54].

Further, by connecting more EH units (here, the difference in the capacitors on the regions of the unit is determined by the different thicknesses of the same material, namely Cytop™) in an appropriate design (such as the one shown in Figure 2.12A, the same authors [60] were able to develop a system of variable capacitors that could switch from a "duplicative" configuration (corresponding to switch SW1 closed and switches SW2, SW3 open in Figure 2.12B), in which all sink capacitors of the system are connected in series between them and in parallel with the source capacitor (Config. 1 in Figure 2.12C), to a "distributive" configuration (corresponding to SW1 closed and SW2 and SW3 open in Figure 2.12B) in which all the capacitors are connected in parallel (Config. 2 in Figure 2.12C). By doing so, when an external actuation makes the drop slide back and forth from one side of the EH units to its opposite, the repetitive change between the two configuration causes the charge in the system to vary at each cycle accordingly to the relationships $Q(i+1) = \gamma Q(i)$, with $I = i\text{-}th$ cycle and γ is the exponential growth factor, equal to:

$$\gamma = 1 + (n-1)\frac{\alpha\beta - n}{(\alpha + n)(\beta + n)} < n$$

Eq. (2.12)

Where n is the number of the sink elements in the generator, $\alpha = C_0'/C'$ is the ratio between the source capacitance and the sink capacitances (when $C' = C_1' = C_2' = \ldots = C_n'$) in the distributive configuration, and $\beta = C/C_0$ is the ratio between the sink capacitances (when $C = C_1 = C_2 = \ldots = C_n$) and the source capacitor in the duplicative configuration. As evident from Eq. (2.12), to increase the charge in the system at each cycle the condition $\alpha\beta > n$ must be satisfied; in this case, the capacitances in the two configurations depend on the thicknesses of the Cytop™ layers in the two different regions of the EH unit.

It is also worth mentioning that for a fixed αβ value, there is an optimal number of sink capacitors that maximizes *γ*. In Figure 2.12D and Figure 2.12E the output voltage as a function of the harvesting cycle for different source capacitances for n=2 and n=3, respectively, is shown: the value of the source capacitance does not affect the maximum voltage, but it affects the number of cycles required to reach the maximum output (of course, the exponential growth cannot be infinite but is limited by the amount of excess charge that can be induced on the drop, which is a mainly function of the size of the drop). In this work, output voltages as high as 168 V (after 7 cycles) and 56 V (after 6 cycles) were measured over a three-drops generator (Figure 2.12A) loaded with mercury and water drops, respectively, of 300 µL each, but most important of all, an energy conversion efficiency of 12,2% and 7.9% were estimated for mercury and water, respectively, a value which is orders of magnitude higher than those reported in the literature [60].

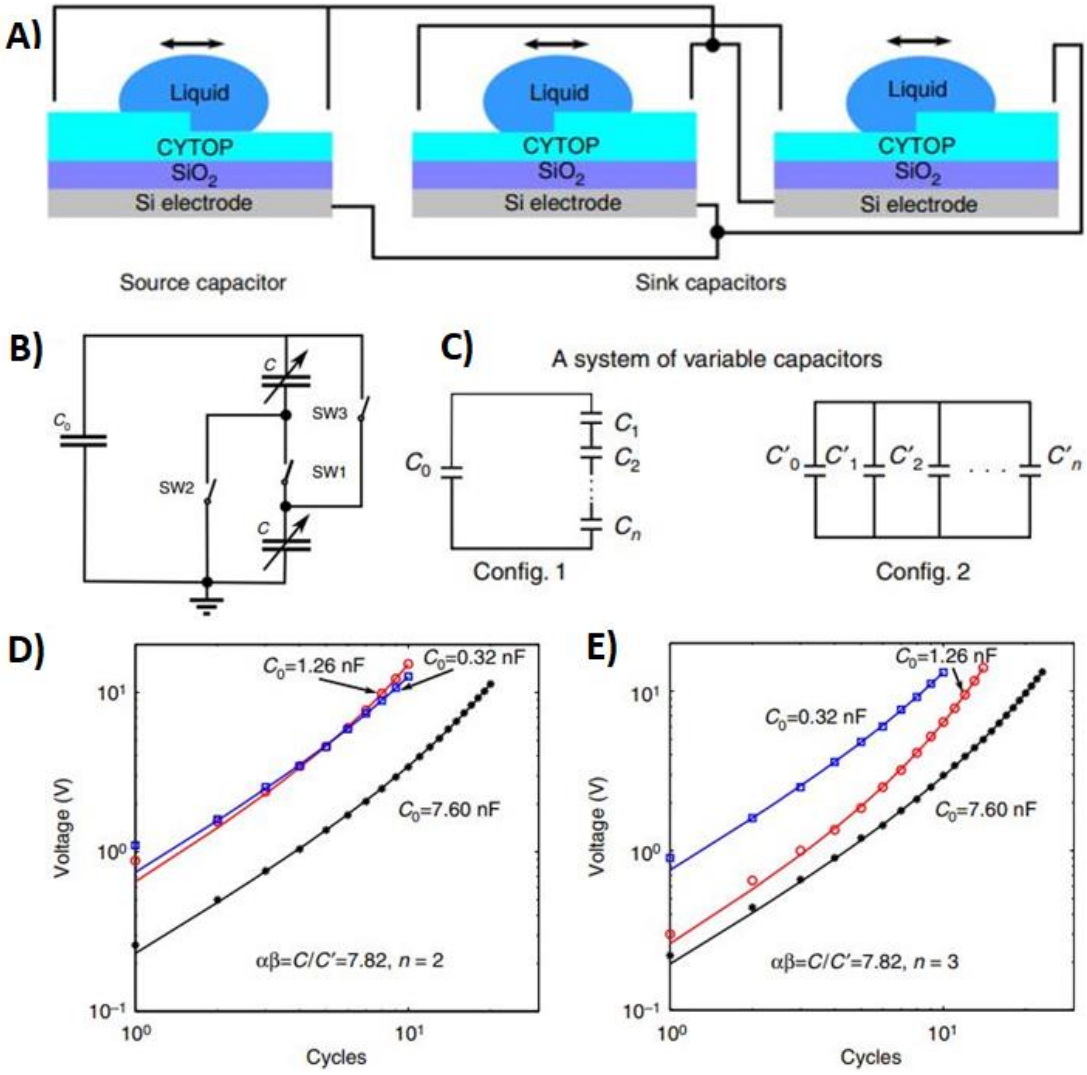

Figure 2.12 – A) Schematic model for a Three-elements (one source and two sinks) generator, in the case the source element is an EH unit where the thinner and thicker side of the triboelectric layer are switched in position. B) Equivalent circuital scheme at rest. C) Equivalent circuital scheme for duplicative (on the left) and distributive (on the right) configurations. D) Voltage output as a function of working cycles, for a generator with two sink elements and different commercial capacitors as source. E) Voltage output as a function of working cycles, for a generator with three sink elements (loaded with a 150 µL mercury drop each) and different commercial capacitors as source (C_0). Images taken from [60].

In conclusion, since the ground-breaking work of Krupenkin and Taylor [27], the efforts into developing new devices for water EH were immediately enhanced, leading to a quite large number of surveys on such topics in the last decade, as highlighted in Figure 2.13.

Figure 2.13 – The research work related to REWoD EH, up to this year. Taken from Web of Science online database.

Thus far, energy outputs from such devices are in the order of units of $\mu W/cm^2$ for the purely triboelectric energy harvesters, and even in mW/cm^2 range for the piezo/triboelectric hybrid energy harvesters. Such values allow for those technologies to be already implemented in low power demanding modern electronics, such as RFID tags or LEDs (see Figure 2.14).

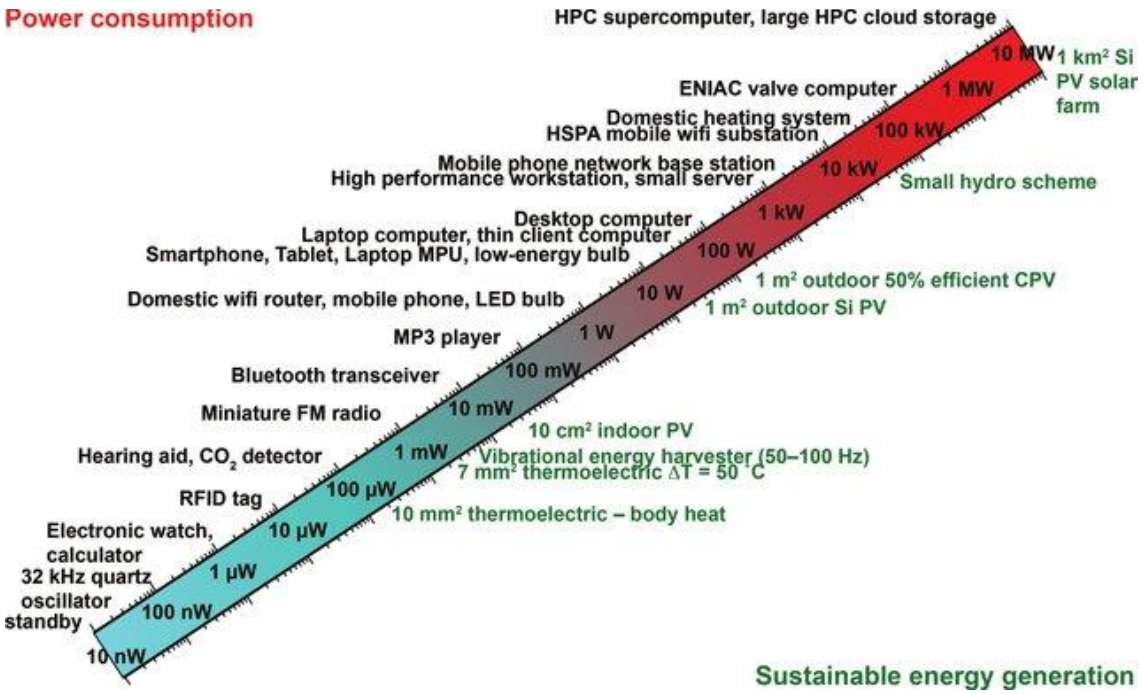

Figure 2.14 – Chart showing the power requirement of many common life electronic devices and the energy range of harvestable powers for many EH techniques [61].

3 VEH with micro-structured aluminium electrodes

The present PhD project is focused on exploiting the already discussed methods and techniques, to study low-cost materials suitable for self-powered devices based on REWoD which could be used, accordingly to specific purposes, as force sensor, as accelerometer, or as vibration energy harvester. To develop device prototypes, commercially available low-cost materials were chosen. Despite the techniques proposed by Krupenkin & Taylor [27], Moon et al. [28], and Wang et al. [41] involve different working mechanisms, they all postulate the presence of an EDLC at the liquid/dielectric interface, as expressed in Eq. (2.3), reported here for the sake of clarity:

$$C_T(t) \cong \varepsilon_0 A_T(t) \left(\frac{d}{\varepsilon_p} + \frac{\lambda_D}{\varepsilon_d} \right)^{-1} \cong \frac{\varepsilon_0 \varepsilon_p}{d} A_T(t)$$

The main parameters in governing EDLC capacitance, and thus the energy collection, are all ruled by the dielectric layer properties, such as the thickness (d), the dielectric properties (ε_d) and the hydrophobic properties which influence $A_T(t)$.

Since for these devices power output scales with the difference between the maximum and minimum capacitance level during one harvesting cycle, it clearly appears that the dielectric layer properties such as the layer thickness d and the dielectric constant ε_p play the major role in governing the energy harvesting process. However, Eq. (2.3) does not consider explicitly wettability (if not partially in the time-dependent Contact Area $A_T(t)$ term) and triboelectric properties which take part in generating the EDLC. Indeed, almost all literature in water-droplet EH exploits fluoropolymers as dielectric layer, at least for the interface in direct contact with the fluid (in many cases, the dielectric layer is composed by an oxide coated with a thin fluoropolymer film): they not only shine for their low surface energy [62], and thus high WCA (*e.g.* close to 110° on Teflon™), but also for their being the most negatively tribocharging materials.

Surface wettability has duplex nature: it mainly depends on the physical-chemical nature of the surface, such as chemical species and electric polarizability, and on its structural properties. Indeed, surface treatments which induce structuration at micro- or nano- scale may strongly affect the spontaneous tendency of a surface to interact with a certain liquid: a well-known example comes from superhydrophobic fractal surfaces [63], consisting of surfaces presenting scale-invariant roughness.

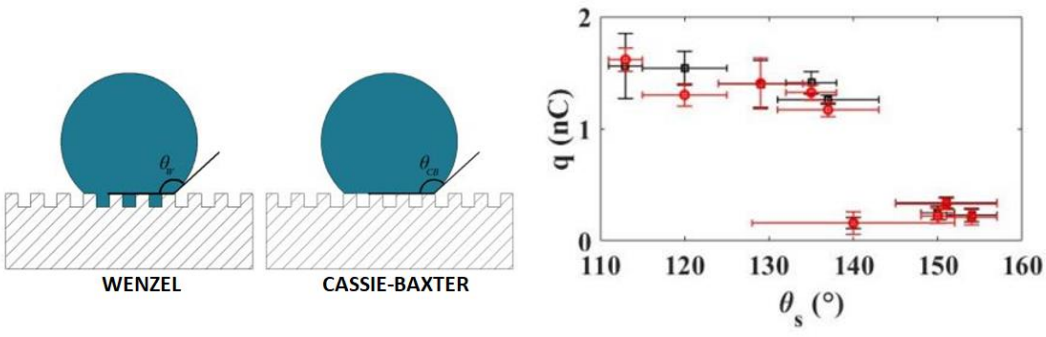

Figure 3.1 – On the left, the wettability states for liquids on textured surfaces (image taken from [64]). On the right, measurement of the tribocharge generated by a 50 µl water droplet sliding over Fluorinated Ethylene Propylene (FEP) films, as a function of their Static WCA. Black squares refer to charge measured by a Faraday cup, red circles refer to current measurements (image taken from [65]).

Helseth & Guo [65] determined how micro-scale surface roughness plays an important role in governing the TE process: they polished Fluorinated Ethylene Propylene surfaces with abrasive grits at different, and as shown in the right panel of Figure 3.1, they observed a general decrease of the tribocharge generated for water droplets sliding on the treated surface, due to a decrease in the effective liquid/solid contact area. Such decrease becomes stronger near the superhydrophobicity region (WCA>150°), which was related to a transition from a Wenzel wettability state, in which the drop can still maintain contact with most of the surface despite the roughness, to the Cassie-Baxter wettability state (also known as "fakir" state), in which surface roughness is such that the liquid cannot fully cover the surface because of air sacks forming within pores or cavities in the texture, and stays thus suspended over the surface "edges" (see left panel in Figure 3.1).

3.1 Aluminium oxide dielectric layers

Due to its excellent mechanical properties, Aluminium usage is widespread and ranges from aerospace (indeed, it was a crucial resource for aviation during World Wars) and naval industries, to biomedical and house devices. As already stated, it spontaneously reacts with Oxygen to produce a thin oxide layer which protects the bulk from further corrosion in most environments but fails in this purpose when in humid and saline ones [66]. Indeed, bulk aluminium spontaneously grows a few nm passivating layers of Al_2O_3 at the surface, a material with excellent chemical, mechanical, electric, and thermal properties [67]. Also, it is a material easy and cheap to process: several techniques are indeed available nowadays to control layer thickness, crystallinity grade, corrosion resistance [68], surface morphology, wettability [69, 70]. To improve corrosion-resistance, several methods to grow controlled oxide layer were developed, and some of them also involve a change in the wettability properties of the surface. Generally, aluminium oxide super-hydrophobicity is obtained by means of so-called "two-steps" processes [71]. Here, the first step involves mechanical as well as electrochemical surface treatments, such as abrasive polishing, electrochemical discharging, etching, anodization, as well as plasma and laser treatments, which purpose is to increase the surface roughness. Then, in the second step the surface free energy is reduced by means of applying thin coatings of hydrophobic species, such as fatty acids or their salts, silanes and of course, fluoropolymers. More recently, under economical as well as environmental sustainability urges, it became of interest to find alternative solutions for Aluminium super-hydrophobicity that do not require the applications of low surface energy chemical species, enabling thus to modify the surface chemically and morphologically in a "single-step" process, whereas in the "two-steps" process the surface roughness modification is generally performed to increase the adhesion of the hydrophobic coating on the surface. Moazzam and co-workers [68] tried to determine how alterations of surface morphology and free energy at a molecular scale correlate with corrosion-resistance properties of Aluminium alloys: by applying a facial one-step approach for Aluminium super-hydrophobicity, as proposed by Chen et al. [69], they obtained micro-textured surfaces in which etched structures composed of rectangular building blocks alternating with planar areas where the corrosive process was much less intense. In both these, as well as other studies performed on analogous systems [72, 73], the wettability properties of the surfaces were correlated to micro/nano-scale morphologic features. In other works, a correlation between chemical composition and wettability behaviour was surveyed yet paying attention mainly to bulk composition instead of surface one.

Since wettability is a strictly superficial phenomenon, the chemical composition at the surface is a necessary information to fully rationalize the interaction occurring at the liquid/solid interface; yet such study is lacking. In this activity, superhydrophobic surfaces of Al alloy were produced and characterized both on the morphological and compositional perspective, by means of microscopic and spectroscopic characterization techniques, respectively.

3.1.1 Aluminium samples preparation

Preparation of the Al samples was conducted following the one-step method as in [69]: aluminium (Al 6060 with a nominal composition of Si and Mg) platelets and disks were cleaned with acetone and distilled water by ultrasonication for 10 minutes. They were then treated with aqueous solutions of 1 mol/l NaOH for 5 minutes at room temperature. Thereafter, they were immersed in a mixed acid solution of hydrochloric and acetic acids with ratio of volumes $V_{H2O} : V_{HCl} : V_{CH3COOH} = 20 : 10 : 1$. Different etching time were tested while keeping all other experimental conditions constant in order to elucidate its effect on surface modification, thus producing the set of samples S_1-S_5 described in Table 3-1. After treatment, each sample was ultrasonically rinsed with distilled water several times and, finally, dried at 120 °C in air for at least 2 hours. Untreated aluminium sample S_0 was taken as reference for wettability, morphological analysis and for chemical characterizations.

Sample	Etching time [min.]
S_0 (reference Al)	0
S_1	4
S_2	4.5
S_3	5
S_4	5.5
S_5	6

Table 3-1: list of the surveyed samples.

3.2 Samples characterization

3.2.1 Characterization techniques

3.2.1.1 Contact Angle Goniometry

The samples wettability was defined by measuring the static contact angle on an OneAttension Theta optical tensiometer, proposed in the left panel of Figure 3.2. Such instrument is capable of acquiring measurement of static, dynamic and roughness-corrected WCA (since WCAs are affected by surface morphological properties, with this latter measurement modality it is possible to determine the contribution of the surface chemical composition alone).

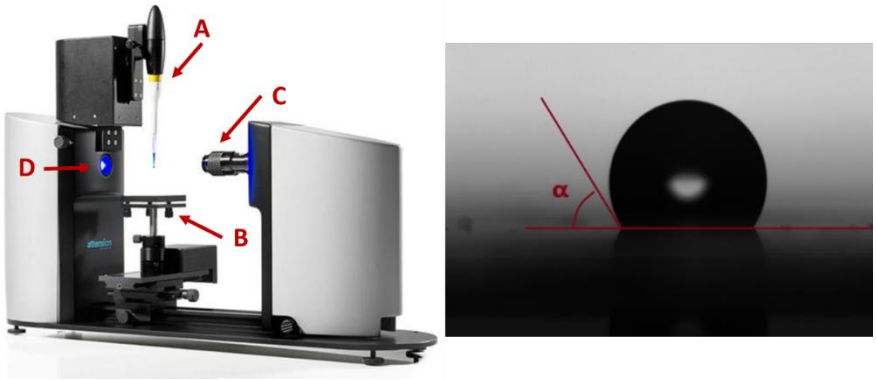

Figure 3.2 – On the left, the OneAttension Theta optical tensiometer used for WCA measurements: element A is the syringe pump used to deposit the liquid drops on samples, element B is the sample supporter, element C is the optical camera for image recording, and element D is a backlight. On the right, an example of the images recorded, showing the WCA, namely the complementary to the angle comprised between the surface plane and the tangent line to the droplet profile at the triple contact line (indicated as α).

To measure the static WCAs, a droplet of known volume is deposited on the sample surface by means of a syringe, and the camera starts recording its spreading on the surface. The WCA value is then calculated by the OneAttension software which identifies both the surface plane and the tangent line at the triple contact line, as shown in the right panel of Figure 3.2.

In this work, average static WCAs (or equilibrium WCAs) were collected depositing 3 µl while monitoring their shape during time for 60 s. For each sample, measurements were performed in at least four different positions at room temperature. The WCA value was calculated using tangent line method.

3.2.1.2 Scanning electron Microscopy (SEM)

The samples morphology was examined using a Hitachi TM3000 benchtop SEM microscope implemented with a probe for energy dispersive X-ray analysis (EDX) and a Zeiss CrossBeam FIB-SEM, proposed in Figure 3.3. Scanning Electron Microscopy with Field Emission source (or FE-SEM) is a versatile technique used in many industrial laboratories, as well as in research and development.

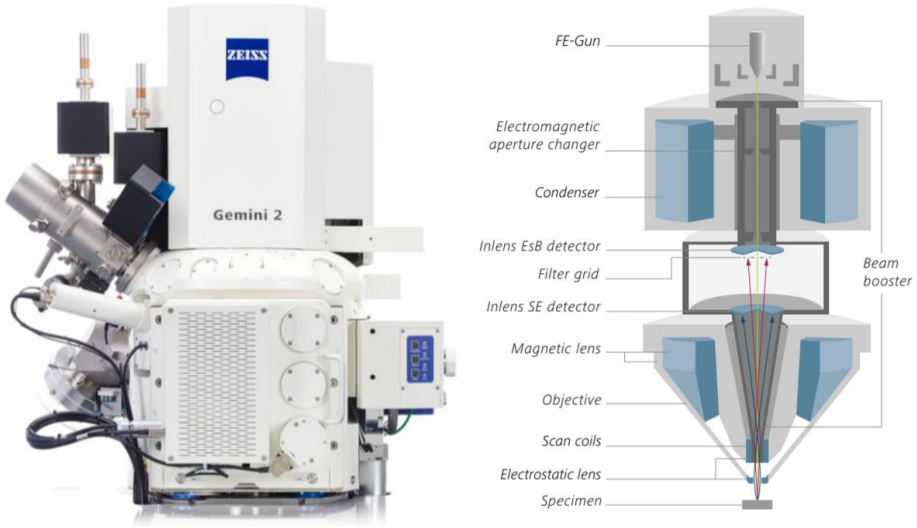

Figure 3.3 – Zeiss Crossbeam Gemini 2 FE-SEM: image and detail of lens column with Condenser lens and, Inlens EsB detector and Inlens SE detector indicated. [source: www.zeiss.com]

Because of its high resolution, large depth of field and frequent combination with X-ray microanalysis, FE-SEM is often used in materials science (including polymer science) to investigate microscopic structures or differentiate different phases from each other. The operation of SEM is based on a focused electron beam that scans line by line the surface of the sample, hosted within the vacuum column of the microscope. This operation produces a 2D image of the surveyed surface, based on the interactions between probe beam and sample. Two types of FE-SEM analysis modes were used in this work. The first is based on the detection and processing of secondary electrons of the *II*-type (SE*II*) [74], which are generated after interactions of probe electrons with a large volume within the sample bulk. This mode displays low-resolution topographical information, suitable for rapid sample scans. The second measurement mode exploits I-type Secondary Electrons (SE*I*), high-energy electrons produced within a thin region close to the surface and detected by the In-lens type sensor. The latter mode produces images with higher contrast and resolution, as shown in the comparison proposed in Figure 3.4, but is much more time consuming.

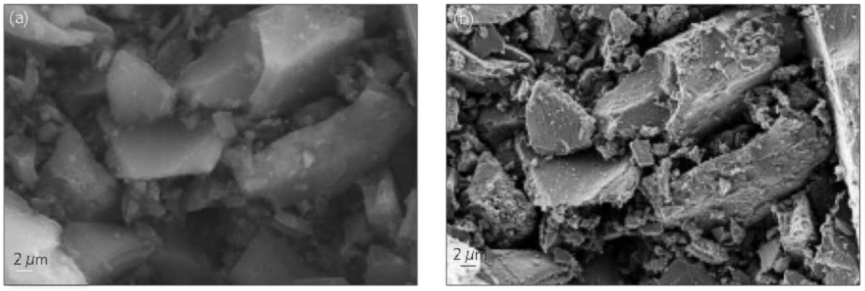

Figure 3.4 – Comparison between SEM images of Pd sample on C-based catalyst [75], obtained by analysis of SEII electrons detected by a classical Everhart-Thornley sensor (left) and SEI electrons detected by an Inlens sensor (right).

3.2.1.3 X-ray photoelectron spectroscopy (XPS)

Surface composition was investigated by X-ray Photoemission Spectroscopy (XPS), a surface sensitive technique based on the analysis of photoemission of core electrons induced by X-rays.
The sample is exposed to a beam of "soft" x-rays (namely, with energy in the 10^2-10^3 eV [76]), typically using Al K_α and Mg K_α lines. The photons can be absorbed from an atom of the sample, which is excited. From the excited state different processes can occur, like photoemission, Auger processes, electron-hole pair creation and anelastic processes.

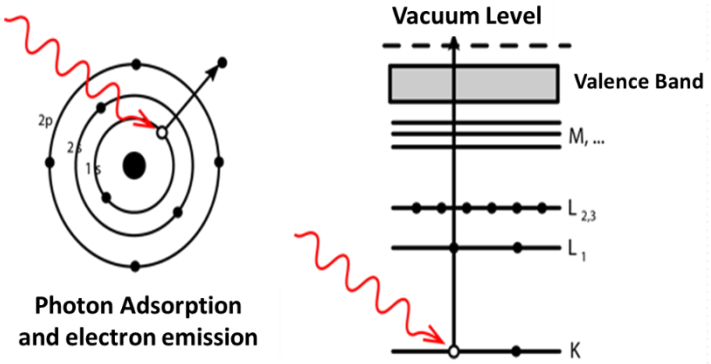

Figure 3.5 – Photoemission process: the photon (red) is adsorbed and a core electron from the K band (namely, the 1s core shell) is emitted.

In a photoemission process, depicted in Figure 3.5, the excitation energy given by the photon is directly used to promote an electron from a core level to the conduction band, above the Fermi level. If the electron has enough kinetic energy to overcome the work function of the material, it can escape from it. From simple energy conservation it follows that the kinetic energy E_k for the electron is:

$$E_K = h\nu - E_B - \phi$$

Eq. (3.1)

Where E_B is the binding energy of the electron, φ is the work function of the material and $h\nu$ is the energy of the electron. Since $h\nu$ and φ are known parameters, from the measure of E_K it is possible to obtain direct information on the binding energy of the atomic level from which the electron was photoemitted. This provides information on the atomic species present at the surface of the sample as each atomic species is identified by precise value of the binding energies of its electrons.
The electrons living in the valence band are weakly bounded to the nucleus and thus are strongly influenced from the chemical environment near them. On the opposite, the core electrons do not feel such a strong effect and show only a small variation (of the order of a few eV) of their binding energy, labelled as chemical shift or core level shift. Accurate measurements of this chemical shift provide information on the chemical environment the different atoms feel around them and can be used, for example, to distinguish graphitic carbon bonded to form the graphene layer (which has C1s E_b=285 eV) from the carbidic carbon forming nickel carbide (C1s E_B=283 eV). [77]
XPS is a surface science technique not because of the X-rays, which can penetrate the sample for hundreds of atomic layers, but because of the mean free path of the photoemitted electrons (having energy of 10^2-10^3 eV) is limited to few atomic layers: only the electrons photoemitted in proximity of the surface can reach it and be detected. The surface sensitivity can be enhanced by changing the angle of detection of the photoemitted electrons: the more grazing with respect to sample surface, the higher the surface sensitivity. XPS is a quantitative technique: the intensity of the photoemission peaks is indeed proportional to the number of atoms of a certain specie excited by the beam, once considered the sensitivity factors for each detected species.

A schematic drawing of an XPS spectrometer is reported in Figure 3.6 (a): the most important parts are the X-ray source (Omicron DAR400) and the hemispherical analyser (Omicron EA125).
The DAR400 source produces the X-rays by accelerating electrons emitted by a hot filament against an anode placed at the tip of the gun. The anode is divided into two sections which are coated with aluminium and magnesium respectively, to emit photons having two possible energy values: hν=1486,6 eV corresponding to the $Al_{K\alpha}$ band and hν=1253,6 eV corresponding to the $Mg_{K\alpha}$ band. Since the source is non-monochromatized, the X-ray radiation has a natural line width of 0.85 and 0.70 eV, respectively for the emission lines, and this is the main limiting factor for the energy resolution of the XPS spectra.

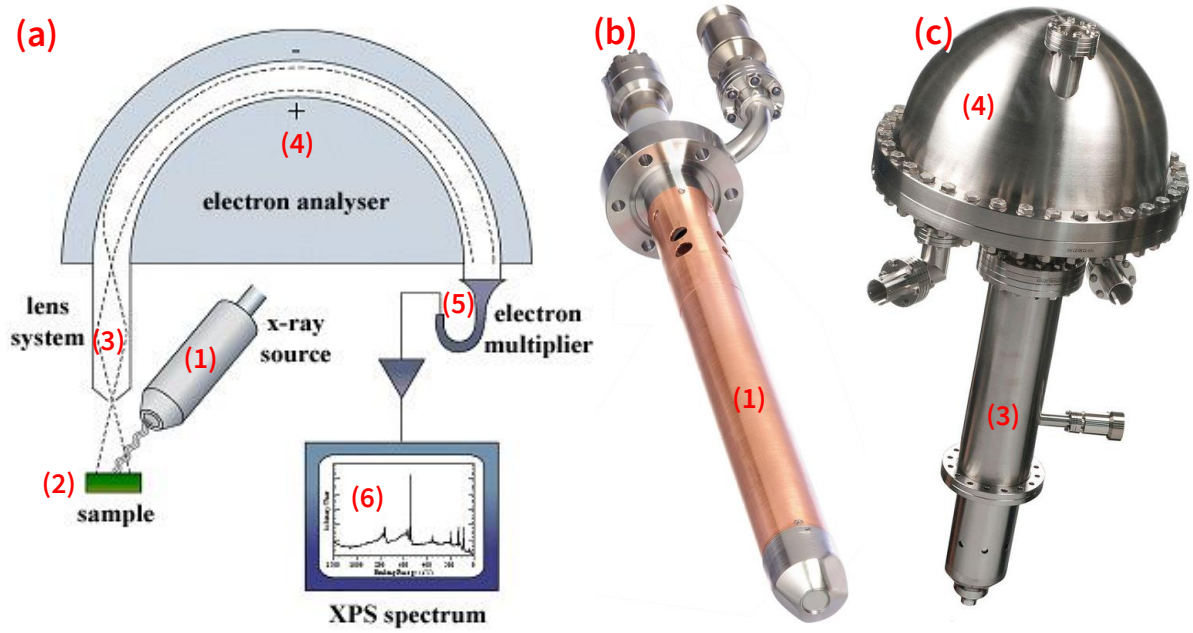

Figure 3.6 – (a) schematic drawing of an XPS spectrometer. Different parts can be identified: (1) the X-ray source, (2) the sample, (3) the electrostatic lens system focussing the photoemitted electrons into the (4) hemispherical electron analyser and only those having a desired energy value can reach the (5) electron multipliers being converted into detectable current pulses which are counted and recorded by the (6) data acquisition system. – (b) a picture of the Omicron DAR400 X-ray source and of the (c) Omicron EA125 hemispherical analyser installed on the Spectroscopy Chamber.

The availability of two different photon energies is a common characteristic of XPS X-ray sources because it straightforwardly allows to distinguish between photoemission and Auger peaks: indeed, comparing spectra recorded at different photon energies, photoemitted electron peaks have always the same E_B, whereas Auger electrons, having the same E_K, correspond to apparently different binding energies in spectra as a function of E_B.
A set of electrostatic lenses collects, focuses, and accelerates the photoemitted electrons towards the hemispherical analyser. A set of slits is available at the entrance of the analyser, which can be used to filter out part of the electrons reducing the collection spot size if more spatial resolution is desired.
Only electrons having the desired E_0 energy value can pass through the analyser to reach the detection system, consisting in five channeltrons. The energy resolution of the analyser can be set by changing the *pass energy* ΔE, that is the energy range (around E_0) of the electrons which are allowed through the analyser: the lower ΔE, the higher is the resolution ($E_0/\Delta E$), but at the expense of the counts number. The value of ΔE = 22 eV was chosen as the best compromise.

An example of an XPS spectra for a graphene film on Ni(111) is reported. The red curve is XPS scan with wide energy range 0-1000 eV, used to investigate the presence of all the chemical species. The main features are quickly identified: an intense doublet is due to the nickel substrate (853 eV) and the three Auger peaks between 650 and 800 eV. No peak is detected around 530 eV which means that no oxygen is present on the sample while the small peak at 285 eV is the fingerprint of the graphene layer.

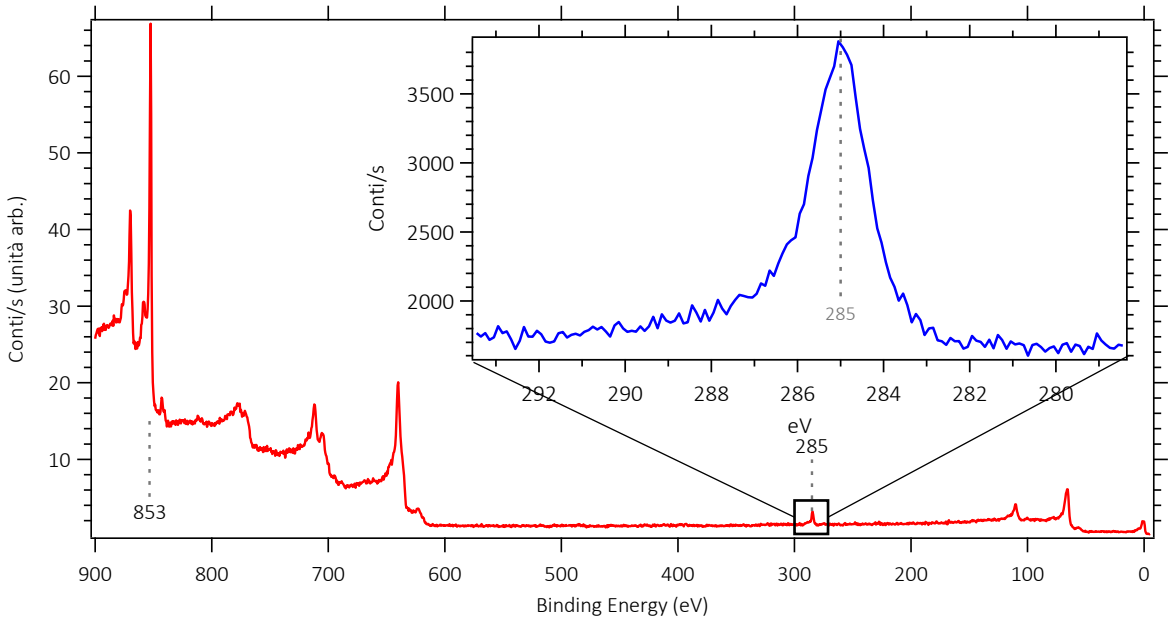

Figure 3.7 – Example of a XPS spectrum: a wide energy scan (red) and a high-resolution section centred on the C1s peak (blue)

Having identified the chemical species of interest, high resolution scans can be collected for shorter energy ranges, obtaining spectra like the inset in Figure 3.7, centred around the C1s region which can be analysed more in detail. The peak position, centred at 285 eV allows the unambiguous identification of graphitic carbon, which testifies the presence of the graphene film.
The XPS spectra must be calibrated using known reference values which must not show any significant core level shift during the experiments. In this case the reference value is the main peak of nickel ($Ni2p_{3/2}$ = 853 eV) since most of the signal comes from the bulk of the sample and is not influenced by the presence of the graphene layer or other species.

Surface chemical composition was investigated by X-ray photoemission spectroscopy (XPS, by Physical Electronics). The instrument is hosted in an ultra high vacuum (UHV) chamber with base pressure below $5 \cdot 10^{-8}$ mbar and equipped with a load-lock system for fast entry of the sample. XPS spectra were acquired with a monochromatized $Al_{K\alpha}$ X-ray source (photon energy $h\nu$=1486.6 eV); photoemitted electrons were collected at an emission angle of 45° from the surface normal, with a spot size diameter of approximately 100 μm. An electron gun was used for charge neutralization during all measurements.

3.2.2 Results and discussion

3.2.2.1 WCA measurements

Figure 3.8 shows a collection of WCA measurements for the S_1-S_5 sample set, recorded for 3 µL water droplets one minute after droplet spilling, a time lapse sufficient to allow droplets to reach their equilibrium WCA (ϑ_e).

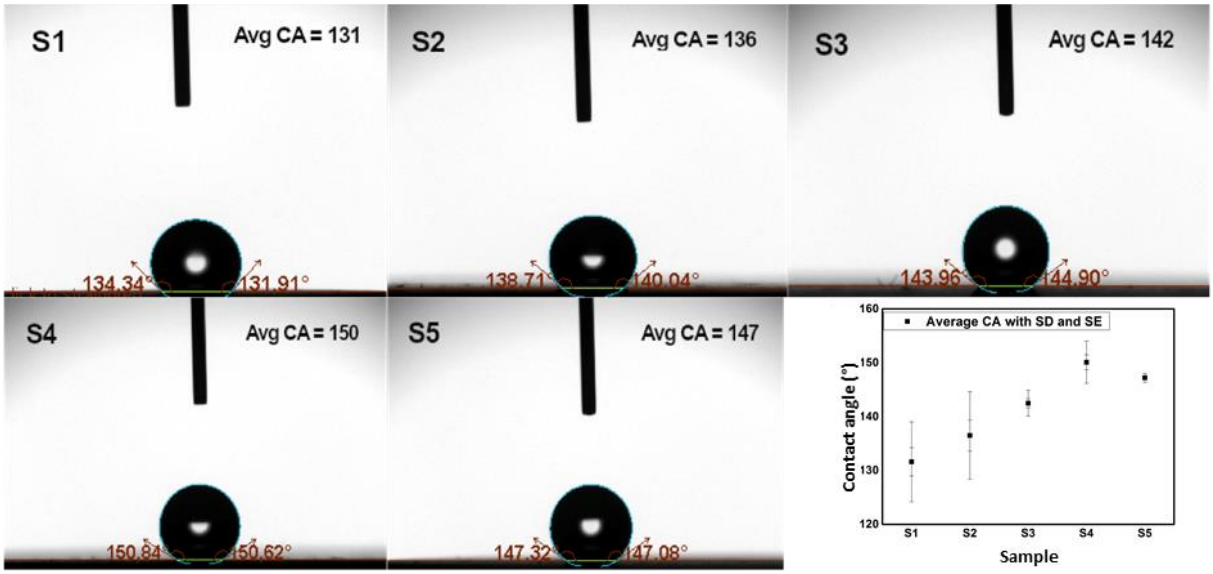

Figure 3.8 – Optical images of water droplets on Al samples S1 to S5 during WCA measurements. In each panel, the small arrow and numbers adjacent to the droplet are the WCA measured on both sides for that particular droplet; the average WCA value for that sample is written in the top-right corner of each panel. Bottom-right panel: average water contact angles for samples S1-S5 with standard deviation and standard error. Image and caption taken from [70].

For each sample, WCA was recorded in four different positions: the averaged value of the equilibrium WCA for each sample is reported in its respective panel of Figure 3.8 and summarized in the bottom-right panel in the same figure, along with the standard deviation and standard error, as well as in Table 3.2. Aluminium spontaneously shows hydrophilic behaviour, since the oxide layer they form at the surface presents a WCA value of ~75° [69]; the averaged equilibrium WCAs (ϑ_{avg}) recorded for samples S_1-S_5 insist in the 130°-150° range as a function of treatment time, confirming that chemical treatment modified the surface, making it hydrophobic. It is noted that samples S_1 and S_2 show larger standard deviations from the average value than the other samples. Therefore, they are less uniform than surfaces exposed to longer treatment times, as furtherly underlined from the WCA time evolution reported in Figure 3.9. On the contrary, almost constant WCA values are measured on samples S_3, S_4 and S_5, which can thus be considered good hydrophobic surfaces with uniform properties. According to the measured WCA values, S_4 is the most hydrophobic among investigated samples and its WCA value (150°) is at the lower edge of super-hydrophobic regime. These measurements suggest that WCA variation is caused by surface micro/nano-texturization occurring at the surface and its fraction with respect to the total surface area, as a result of the etching process. In particular, the high WCA recorded for sample S_4 is related to the ability of that surface to form air pockets within etched region, which prevents the water to stay suspended in the flatter, less etched regions, thus avoiding complete contact to the aluminium surface. It will be shown in the following sections how surface chemistry also plays a role in this respect.

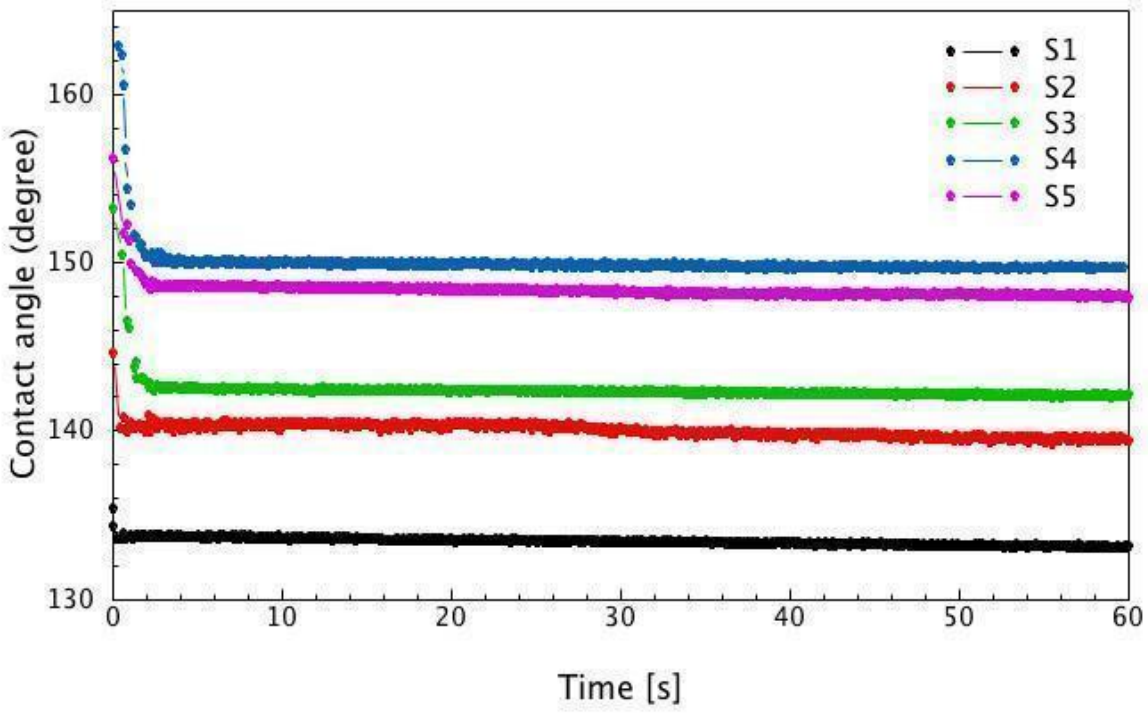

Figure 3.9 – Contact angles time evolution for etched aluminium samples from S1 to S5. Image taken from [70].

In Figure 3.9 the time evolution of water droplets spreading over the samples is presented, each trace corresponding to one of the four equivalent measurements taken to determine ϑ_{avg}. These measurements indicate that WCA is not constant in time; indeed, from a starting condition (t=0 s, ϑ_s), WCA decreases during the measurement until it reaches the equilibrium value ϑ_e. Such balance is reached in few seconds (less than 5), and the contact angle stays constant thereafter. However, as resumed in Table 3.2, both the starting (ϑ_s) and equilibrium (ϑ_e) values show the same direct proportionality with respect to the etching time, and thus with surface morphologic and compositional properties, as commented above.

Sample	Etching time [min.]	Starting CA ϑ_s [°]	Equilibrium CA ϑ_e [°]	Average CA [°]
Reference Al	0	-	-	75
S_1	4	135	133	131
S_2	4.5	145	139	136
S_3	5	153	142	142
S_4	5.5	163	150	150
S_5	6	156	148	147

Table 3.2: Contact angle of samples S1 to S5. Column 2 reports the etching time. The values reported for the starting WCA and equilibrium WCA are extrapolated from the traces reported in Figure 3.9. The average WCA results from at least 4 measurements at different positions on each sample after 60 s time lapse.

3.2.2.2 Surface morphology

A low magnification SEM image of sample S_1 is presented in Figure 3.10. It can be clearly seen that, after etching with acid solution, the entire Al surface is rough. Similarly, to what previously reported [68], such roughness, composed of unevenly distributed micropores and 'protuberances', highlights a texture in which the presence of crevice-like structures relates to not etched and etched areas. Since non-etched areas are still the majority of sample surface, this indicates that etching process with the acid solution, the one inducing the micro-structuring, is too brief.

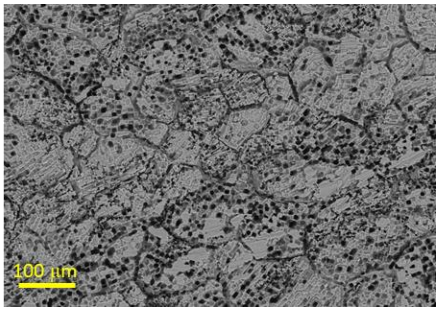

Figure 3.10 – SEM image at low magnification of samples S1 (recorded with electron beam energy of 20 keV).

Figure 3.11a reports a high-resolution image of the same surface and confirms that the etched aluminium surface is formed by irregular protuberances that appear like building blocks of rectangular plateaus. Increasing the etching time (Figure 3.11b – Sample S_2), the surface shows a higher degree of etching. In the SEM image it is possible to highlight flat islands (not etched - left part of the image) and blocky areas responsible for the hydrophobic properties of the surfaces. Sample S_3 (Figure 3.11c) presents a higher fraction of etched surface; blocky surfaces are detected even if their overall aspect is slightly less sharp than for the previous sample. The morphology of the S_4 sample (Figure 3.11d) is very similar to the previous one, with a texture due to the presence of amorphous etched islands and more blocky areas. Sample S5 (Figure 3.11e) still shows amorphous islands and blocky areas morphology. The structures of the blocky areas look like sample S_4 and are "sharper".
Building block shaped structures increase in number and become smaller with the etching time. This could provide more space to trap air and lead to the increased contact angle (as shown in Table 3.2). However, as the etching time exceeds a critical value (S_4 sample), the building block shaped structures are destroyed by excessive etching and large holes form in these microstructures.

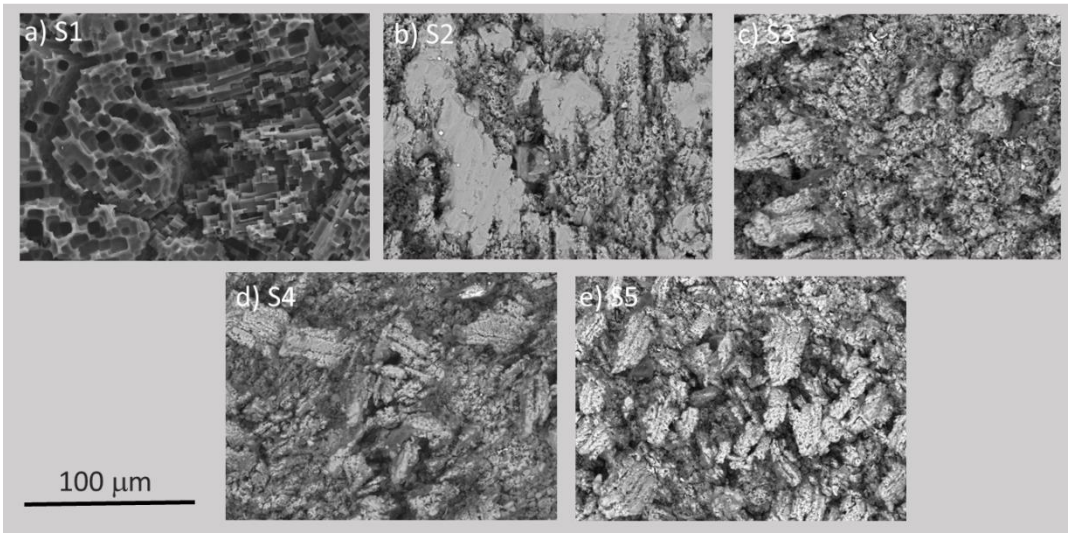

Figure 3.11 – High magnification SEM images showing details of the micro-structured surface obtained after chemical etching of the Al alloy S1 to S5. The image in panel a) is acquired using a 20 keV electron beam, the other images with a 15 keV one.

3.2.2.3 Chemical composition: EDX/XPS characterization

First, EDX analysis is discussed: it detected the majority elements typical of the bare Al6060 alloy for all the samples surveyed (see summary in Table 3.3) [78]. The presence of oxygen is justified since a thin (2-4 nm) and protective glassy oxide film forms instantaneously on aluminium in contact with air. This is due to the highly electronegative character of the metal and to its strong affinity for oxygen. The carbon present is adventitious carbon, which deposits and binds to surfaces from free carbon compounds in the atmosphere [79]. It is noted that for all treated samples the amount of oxygen is lower than that for the Reference Al sheet, while the level of C is significantly higher for samples S_4 and S_5 than for all the other samples analysed. The former effect may be related to the micro-structuring process, which removes part of the native oxide layer, whereas the latter is unexpected and incompatible with any contamination from the measuring apparatus. It is most probably related to the high surface area exposed by the micro-structured samples which is capable of adsorbing carbon-based contaminants from the solution. The remaining elements on the surface are the result of the chemical treatments and sample handling; except for O and C, none of the other contaminants (either Mg, Si, Ag, Na, Cl) exceeds 1% in atomic concentration.

Sample	**wt % - at%**		
	Al	**O**	**C**
Reference Al	77.0 – 62.3	8.8 – 12.0	14.2 – 25.7
S1	86.4 – 76.2	1.5 – 2.2	10.2 – 20.2
S3	77.8 – 63.1	5.2 – 7.1	15.7 – 28.7
S4	60.1 – 41.4	3.0 – 3.5	35.1 – 54.3
S5	52.5 – 35.0	8.6 – 9.6	36.2 – 54.1

Table 3.3: Composition of samples S1, S3, S4 and S5 as determined by EDX. Both the percentage in weight and in atomic concentration is reported. Data measured for an Aluminium sheet are reported as reference.

The surface chemistry of the samples was also characterized by XPS. XPS spectra were analysed using the KolXPD software. Binding energies (E_b) were calibrated on the Al 2p line of metallic Al, set at 72.6 eV according to literature values [80]. The XPS peaks were fitted using Voigt functions after subtracting a Shirley background. Several components were necessary to fit the spectra: 3 components for the Al 2p and O 1s regions, 4 for the C 1s and Si 2p and one for the N1s line and WCA 2p doublet. The FWHM is set equal for all peaks in the same region except for metallic Al, which is narrower than the corresponding Al oxide and Al hydroxide components. First, in Figure 3.12 the survey spectra of the pristine Al alloy (S_0) and of the S_2 sample are compared, *e.g.,* the sample exposed to a relatively short treatment. Both spectra are dominated by the O 1s, C 1s and Al 2p/Al 2s signals, though the relative intensity of the corresponding peaks is different. As anticipated in the previous section, these elements are expected for an Al alloy exposed to ambient pressure and/or treated in liquid solution. In addition, traces of Si (Si 2p at E_b~100 eV), Ca (Ca 2p doublet around 350 eV) and N (N 1s line at E_b~400 eV) appear in the spectra. It is worthwhile mentioning the presence of a very small Cl-related peak (Cl 2p at E_b~200 eV) only for the treated sample, which can be easily explained as the consequence of dipping it in the solution with HCl.

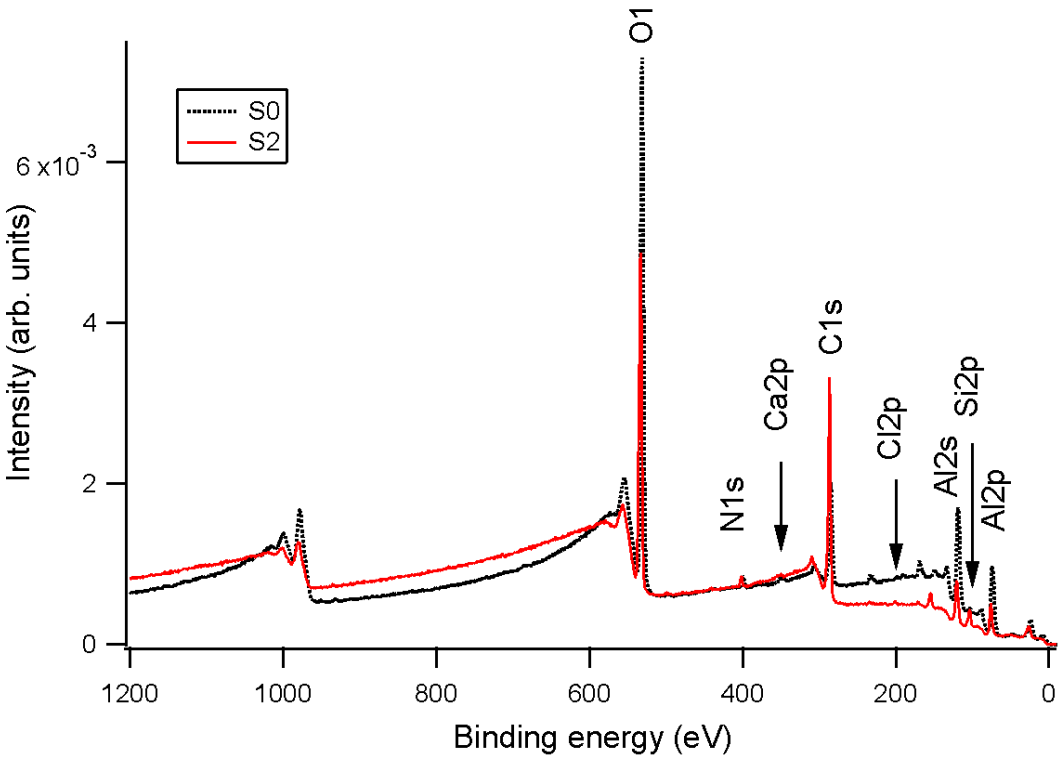

Figure 3.12 – Comparison between the survey spectra of the S0 and S2 samples. Assignment of the main photoemission lines is indicated.

A more detailed inspection of the high resolution regions corresponding to these lines (Figure 3.13) confirms that the chemical treatment has deeply affected the composition of the surface. Starting from the Al 2p region, the spectrum consists of two main features, the first being at low energy, precisely at 72.6 eV, and corresponding to metallic aluminium, in accordance with what observed in literature [81, 82]. The second peak can be deconvoluted into two components at 74.7 eV and 75.5 eV for the pristine S_0 sample. They were assigned to aluminium hydroxide and aluminium oxide, respectively, by comparison with the literature. Indeed, Al and Al oxide are found, respectively at 72.8 eV and 75.5 eV, both for pure Al sample oxidized in vacuum [83] and for $Al_{70}Pd_{21}Mn_9$ quasicrystals oxidised in air [81]. On the other hand, metallic aluminium is reported at 72.6 eV both in old studies [82] as well as in recent databases [84]. Aluminium oxide hydroxide (AlO(OH)) and aluminium hydroxide ($Al(OH)_3$) are characterised, on the contrary, by a binding energy lower than the one of Al_2O_3 and compatible with the observed line at 74.7 eV [85].

The corresponding O 1s components are found at E_b=531.8 eV and 533.0 eV. The former is in good agreement with the value expected for Al_2O_3, which is reported at different E_b in the range between 531 eV and 532.5 eV depending on the kind of sample and sample treatment [82, 83, 86]. The latter energy, on the contrary, is associated with aluminium hydroxide [87]. Both in the Al 2p and in the O 1s region, the Al_2O_3 and $Al(OH)_3$ components upshift and change their relative amount as a consequence of the chemical treatment. In addition, a new component grows at higher E_b (534.9 eV), which is tentatively assigned to O atoms bound to Si, either in oxide or hydroxide compounds [80]. This behaviour indicates that the chemical treatment has affected the surface composition of the sample. This is confirmed also from inspection of the other high resolution regions. The C1s spectrum consists of four components, the most intense of which is at 285.3 eV for S_0 and at 286.2 eV for S_2. both lines were identified as adventitious carbon. This contaminant species is usually observed around 284 eV for samples exposed to environment conditions but is found at ~286 eV for Al since it is mainly due to

adsorption of airborne organic compounds [79, 88]. The second component is found at E_b=287.2 eV for both samples, a value suitable for carbonates [89, 90]. As expected, the level of contamination is larger for the S_2 sample because of the chemical treatment which, on one hand, increases the specific surface area and, on the other hand, exposes the surface to C-containing species. Two additional minor contributions around 288 eV and 290 eV are present with almost vanishing intensity for S_0 and in small amounts for S_2. These binding energies are suitable for C atoms bound to oxygen or halogen atoms. Also, the Si 2p region is fitted with four peaks, corresponding to Si atoms in Si^0 (E_b=98.6 eV) and in increasing oxidation states. The presence of Si is expected since it is present in small amounts in the Al alloy; however, since the Si content at the surface is much higher for the treated sample, a possible accumulation due to the corrosion of the other metallic elements may have occurred during surface micro-structurization. Since the surface energy of SiO_2 (287 mJ/m^2) is larger than the one of Al_2O_3 (169 mJ/m^2) [91], it is speculated that the presence of Silicon dioxide at the surface is energetically disfavoured and that it appears due to etching and remains because the mobility is not high enough. Finally, Ca and N are present in traces. Their origin is probably related to exposure to the air/liquid environment. Indeed, the observed upshift upon the chemical treatment suggests the contact with a more oxidative environment.

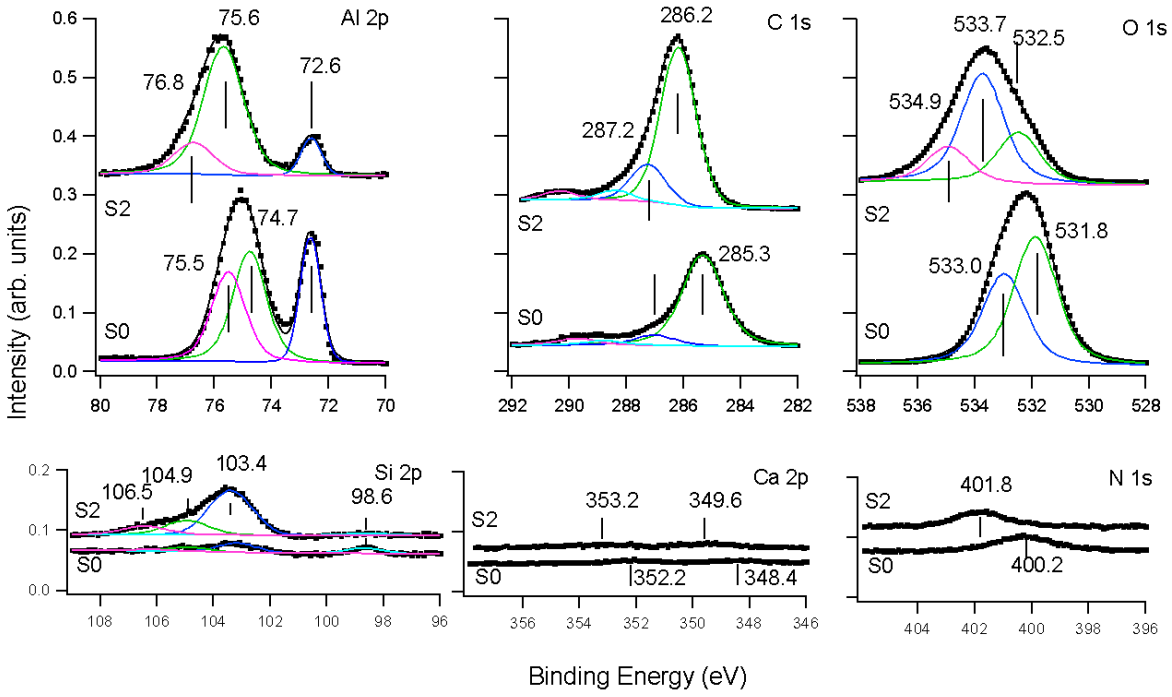

Figure 3.13 – XPS spectra of the Al 2p, C 1s, O 1s, Si 2p, Ca 2p and N 1s regions for the S0 and S2 samples. In each panel, the top spectrum is upshifted for sake of clarity. The different components resulting from the best fit to the data are reported for each spectrum.

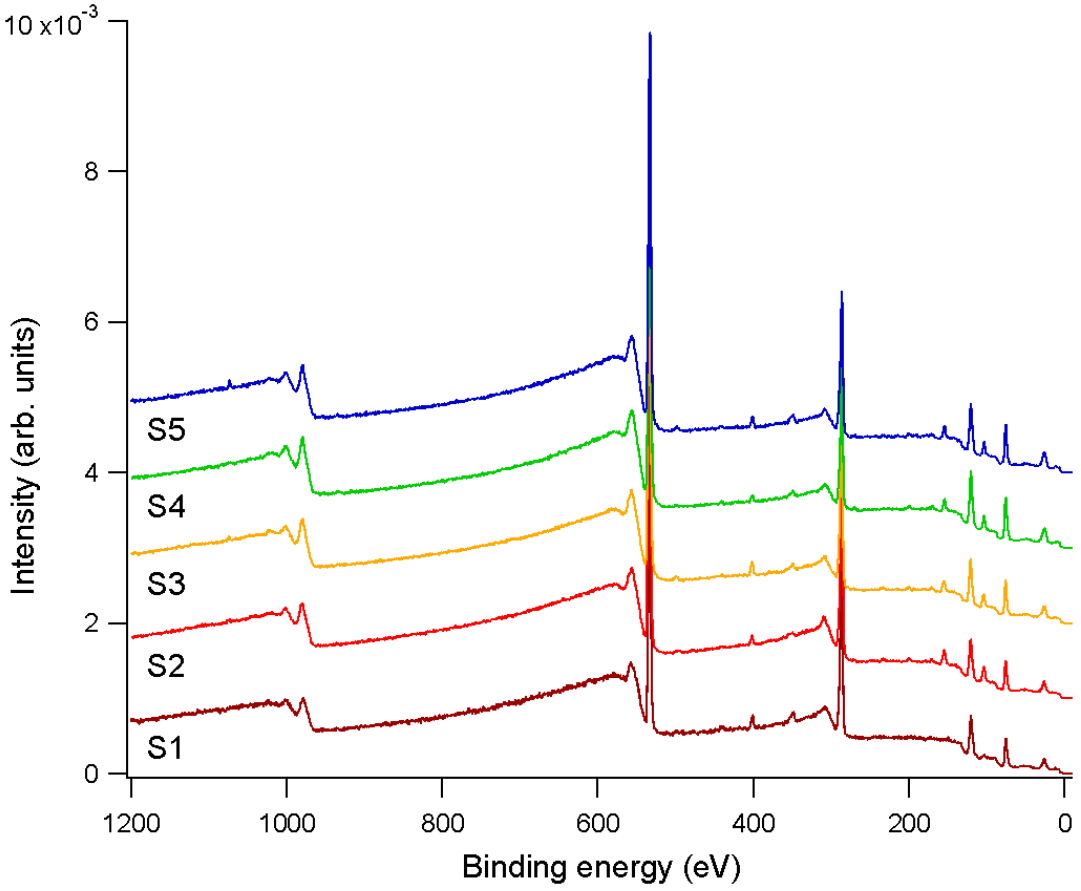

Figure 3.14 – Survey XPS spectra of sample S1 to sample S5. The traces are upshifted for sake of clarity.

Figure 3.14 and Figure 3.15 show the XPS spectra relative to S_1-S_5 samples, namely the evolution of the spectra parametric with increasing etching time. The survey spectra appear very similar and present all the characteristics already discussed for sample S_2. The only difference is the absence of the Si and Cl signals for S_1, which is more like S_0 on this account; this suggests that the corrosion process is mild in this case, coherently with SEM observation and with the smaller WCA measured on the same sample. More information can be gained by inspection of the high resolution regions of Figure 3.15. As evident at a first inspection, the components already discussed in Figure 3.13 are present in each region (except for the O 1s component corresponding to SiO_x species for S_1). For S_1, the binding energy values for the Al 2p and O1s lines related to Al oxide and hydroxide are only slightly higher than those found for the pristine S_0 sample. They further upshift for sample S_2, especially the component around 76 eV ascribed to Al_2O_3, and remain then approximately stable for the other samples. This is not surprising since the E_b(Al 2p) of Al_2O_3 is reported in literature at slightly different values [81, 85, 92], depending on the sample conditions and preparation. The observed behaviour confirms that the S_1 sample is only slightly affected by the chemical treatment and maintains therefore a surface composition more like the one of the pristine samples, while surface modifications become more relevant after a critical treatment time. Furthermore, the relative weight of the different components in the Al 2p, O 1s, C 1s and Si 2p regions changes for the different preparations, as reported in Figure 3.16 and discussed in the next section.

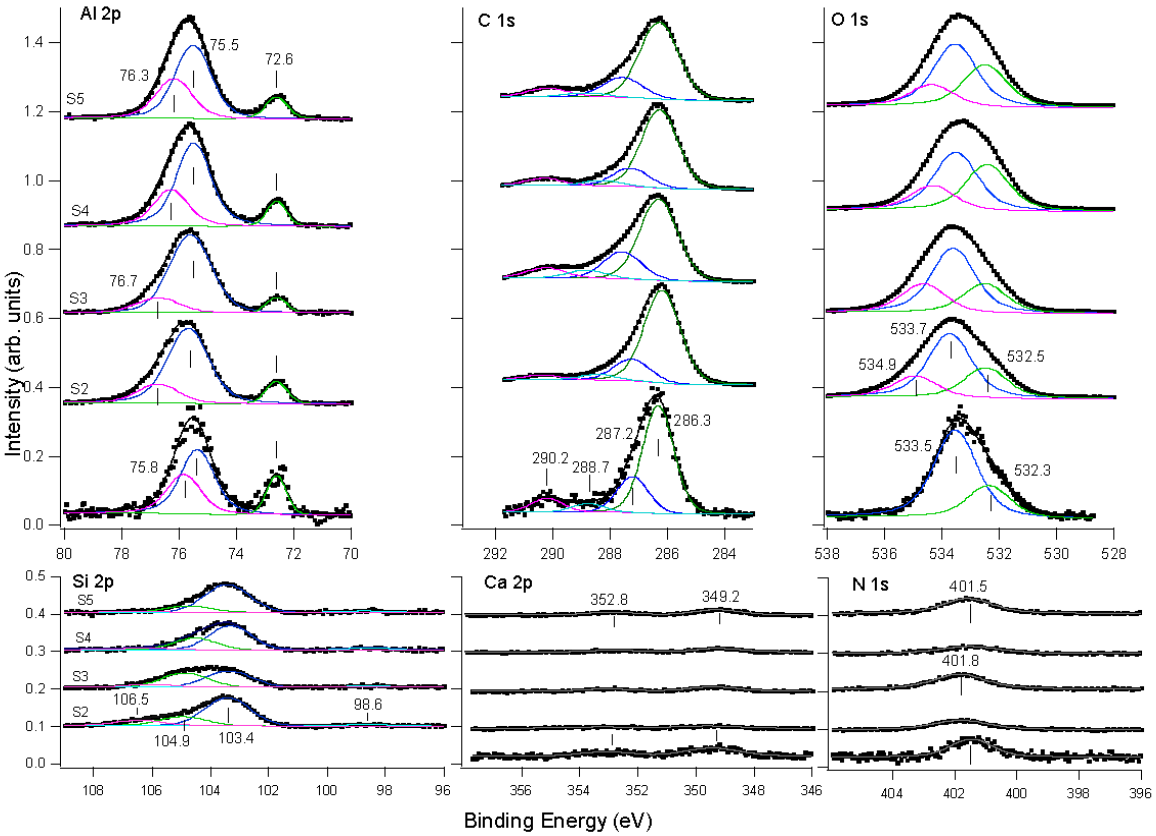

Figure 3.15 – XPS spectra of the Al 2p, C 1s, O 1s, Si 2p, Ca 2p and N 1s regions for samples S1 to S5. In each panel, spectra are upshifted for sake of clarity. The different components resulting from the best fit to the data are reported for each spectrum.

3.2.2.4 *Discussion*

Before drawing any correlation between the hydrophobicity properties of the samples and their morphology and surface composition, it is necessary to put further attention on the evolution of the XPS spectra with etching time.

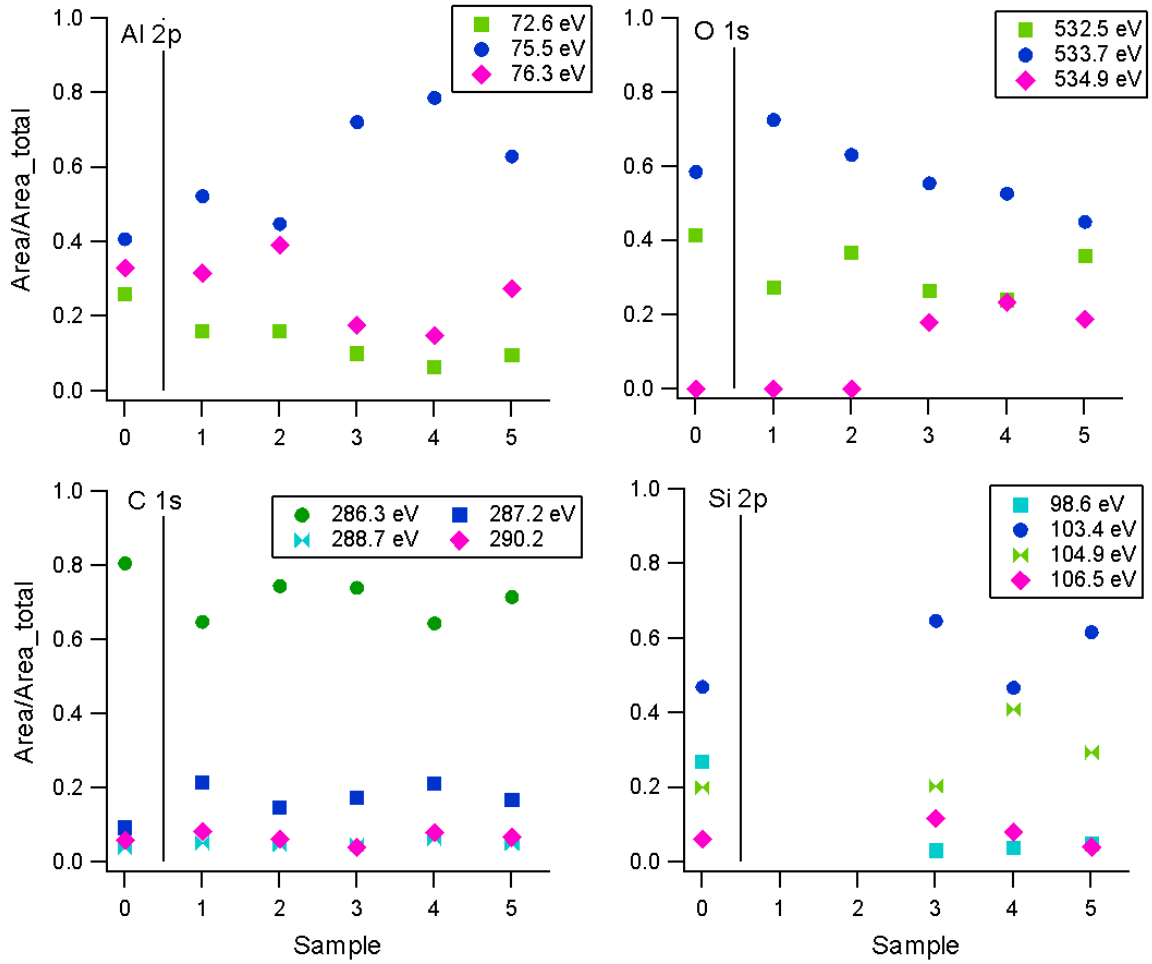

Figure 3.16 – Relative amount of the different Al 2p, O 1s, C 1s and Si 2p components calculated as a fraction of the total area of the corresponding region after background subtraction. In each panel, the number in abscissa refers to the sample number, the vertical line marks the separation between the pristine (S_0) and the treated samples. The different lines are indicated in the caption by their average E_b value.

The four panels of Figure 3.16 report the relative amount of the different components resolved in the Al 2p, O 1s, C 1s and Si 2p regions, respectively, weighted with respect to the total peak area of that region after background subtraction. It is concluded that:

1) Most of the Al atoms are in oxidized (76.3 eV) or hydroxylated (75.5 eV) state, as expected for a surface exposed to air and chemical treatment. The amount of $Al(OH)_3$ increases with etching time up to S4, while it reduces slightly for S5. Metallic Al (72.6 eV) is maximum for S_0 but it is always the least intense component. This is reasonable considering the high surface sensitivity of the XPS technique, which probes only the first few atomic layers below the surface.
2) The behaviour of the O 1s component at 532.5 eV, assigned to Al_2O_3, is in perfect agreement with the corresponding Al 2p curve. The 533.0 eV one, related to oxygen in hydroxide groups, on the contrary, is not in good correspondence with the trend of the 75.5 eV line. The reason for this

discrepancy can be twofold. One hypothesis is that the 75.5 eV peak is the unresolved contribution of $Al(HO)_3$ and AlOOH, with a relative amount which moves in favour of the second compound with increasing treatment time. Alternatively, the 75.5 eV component is the unresolved contribution of $Al(HO)_3$ and more complex Al-Si-O compounds, so that the O1s intensity due OH groups bound to Al reduces when the one related to O atoms and/or OH groups bound to Si increases.

3) By comparison of sample S_0 with the treated samples, it is observed that the amount of carbonate-related contaminants (287.2 eV) is approximately double for the latters. This suggests that the process saturates already after the shortest etching time.
4) The relative amount of adventitious carbon (E_b=286.3 eV), anticorrelates with the one of carbonates. As expected, it is the dominant signal in the C 1s spectrum since Al alloys are well known to react with the organic compounds present in the atmosphere [79] and all samples were analysed after staying in air for several days following etching.
5) In the Si 2p region, the Si^0 component at 98.6 eV reduces dramatically upon anodization (compare S_0 and S_1), while the 103.4 eV and 104.9 eV increase with a non-monotonous behaviour, presenting a minimum and a maximum, respectively, for S_4. The weight of the Si component at 104.9 eV is reasonably correlated with the O1s component at 534.9 eV so that it is reasonable to assign them to oxidised Si and O bonded to Si. Since SiO_2 is expected at 103.5 eV, it is speculated that such moiety can have transferred electrons to the surrounding elements, such as Cl impurity. The interest for this assignment is not purely academic since also the relative amount of the 534.9 eV component correlates with the WCA behaviour and may therefore have an influence on it.

It is interesting to compare the surface composition emerging from XPS analysis with the outcome of EDX measurements summarized in Table 3.3. In doing this, the different penetration depth and spot size of the two techniques must be considered. EDX probes the sample up to a depth of ≈1 μm and provides therefore information on the bulk composition of the sample. On the other hand, the spot size is limited to a few μm^2 so that the information is very local. The data reported in Table 3.3 result from an average over different spectra measured at relevant spots of the sample, not showing the same morphology and thus possibly not equivalent. XPS, on the contrary, detects electrons coming from the first 5-10 atomic layers but collects them from an area of ≈100 μm diameter. It is a very surface sensitive technique, but the information is averaged over a macroscopic area of the surface. First, it is remarked that the major contaminant detected by both techniques is carbon. The origin of such intense signal at the surface is clearly related with the interaction of the samples with free organic compounds in air (it is already evident for S_0) and with the etching treatment (since it increases for the etched samples). This adventitious carbon layer contributes to the C 1s intensity and screens the Al signal from Al atoms underneath. The presence of a significant C contamination in the bulk is more difficult to explain. While the increase in C concentration for the most etched surfaces was discussed in section 3.2.2.3, the presence of a significant fraction of C atoms also in the Reference Al sheet is more puzzling and harder to justify only with contamination at the surface. It can be, at least partially, due to C incorporation, which is a phenomenon typical of all metals, tough in different amount depending on the atomic species (*e.g.* very high for Ni and low for Au) and on the treatments applied. Considering the minor contaminants, it is observed that Na, WCA and N are so small in both EDX and XPS measurements, that they can be only those present at the surface; their origin is thus ascribed to sample treatment and handling. It is recalled that etched samples have a large specific area so that the relative weight of the signal arising from the surface in EDX spectra increases. The interpretation is

different for those elements which are part of the alloy, in particular Mg and Si. A small amount of Mg is detected in EDX spectra of anodized samples, but it is visible in XPS spectra only for S_0 (small peak around 89 meV, assignable to the Mg 2s line), suggesting that Mg is efficiently removed from the surface by etching. The opposite holds for Si, which tends to accumulate at the micro-structured surface.

In conclusion, hydrophobic behaviour of the samples has been related with surface morphology and composition. This study confirms the correlation between the sample micro-structurization and its capability of trapping air, thus leading to WCA increase.

The analysis of the correlation coefficients between WCA and the different components at the surface allows to conclude that:

1. Hydrophobicity correlates with treatment time ($R = 0.99 \pm 0.7$)
2. Hydrophobicity anti-correlates with the relative amount of metallic Al (XPS lines at E_B=72.6 eV, $R=(-0.94 \pm 0.17)$)

Furthermore, [79] demonstrates that the hydrophobic behaviour of Al surfaces is related to the adsorption of organic compounds from the surrounding atmosphere onto the oxidic surface. This consideration perfectly fits with data since the samples were measured several days after micro-structuring and present a huge amount of carbon contamination at the binding energy values suitable for C atoms bound to H, N and O. These findings highlight the correlation between samples wetting behaviour and their compositional as well as morphological properties. A scheme is reported in 5.2.

3.3 Exploiting Micro-structured Aluminium for VEH

In this chapter, power output for electrodes with thin aluminium oxide layers will be discussed. Such part of the PhD has been performed as part of the POR-FESR Asse 1.1.3 project from Regione Liguria, held by a local innovative start-up company exploited in collaboration with CNR-IMEM to develop an Energy harvesting device based on the REWoD principle exploiting cheap and commercially available materials. The micro-structured Al electrode showing the highest WCA value (sample S_4), in accordance with 3.2.2.1, has been selected for further energy harvesting characterization as well as for the development of a laboratory-scale VEH device. Several electrolytes have been investigated, such as DI water, salines solutions and hydrogels.

3.3.1 Experimental setup for VEH measurements of Micro-structured Aluminium electrodes

Prior to that, a suitable experimental setup was prepared as in Figure 3.17: a signal generator (A) produces an input sinusoidal wave, sending it to the shaker control electronics (B) which forces and controls the periodic motion of the shaker (C), and thus of the bottom electrode. The top electrode is fixed on a supported slit, its height being tuneable thanks to a micrometric caliber. The voltage drop occurring along measurement at the two electrodes is collected by a single cable (which also works as resistor load in this setup) and acquired by an oscilloscope. Further, the oscilloscope also acquires the input signal generated by the element A, both as a trigger signal to determine the time shift between generated signal and acquired output, and to determine the experimental height excursion of the shaker.

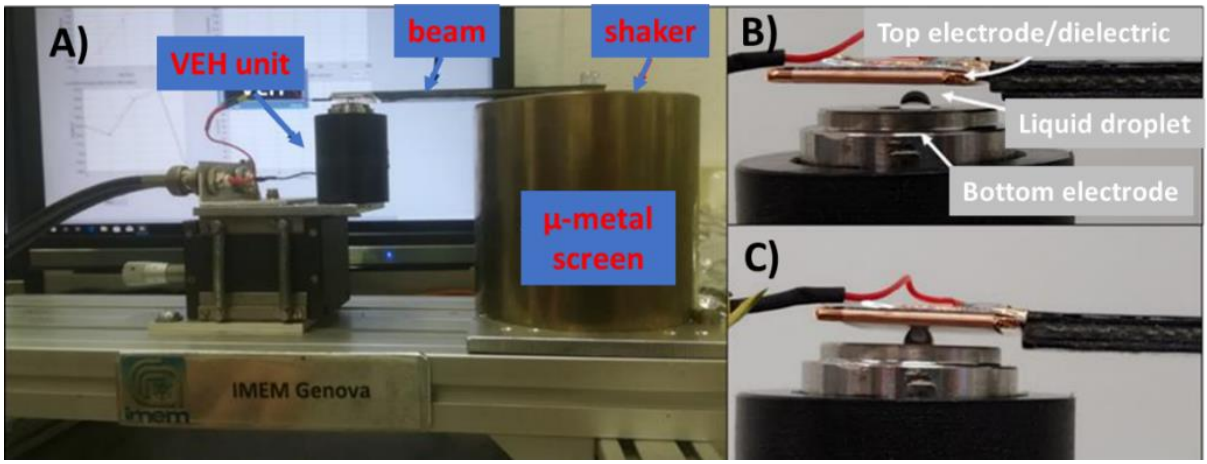

Figure 3.17 – VEH measurement setup: REWoD Unit connected with a beam to the shaker, which is not visible as it is inside the μ-metal screen (A). Closer view of the REWoD unit without the liquid bridge between the electrodes (B) and in presence of the liquid bridge (C). The control electronic is formed by the signal generator (D) the shaker control electronics (E) and the digital oscilloscope (F), used for the signal acquisition.

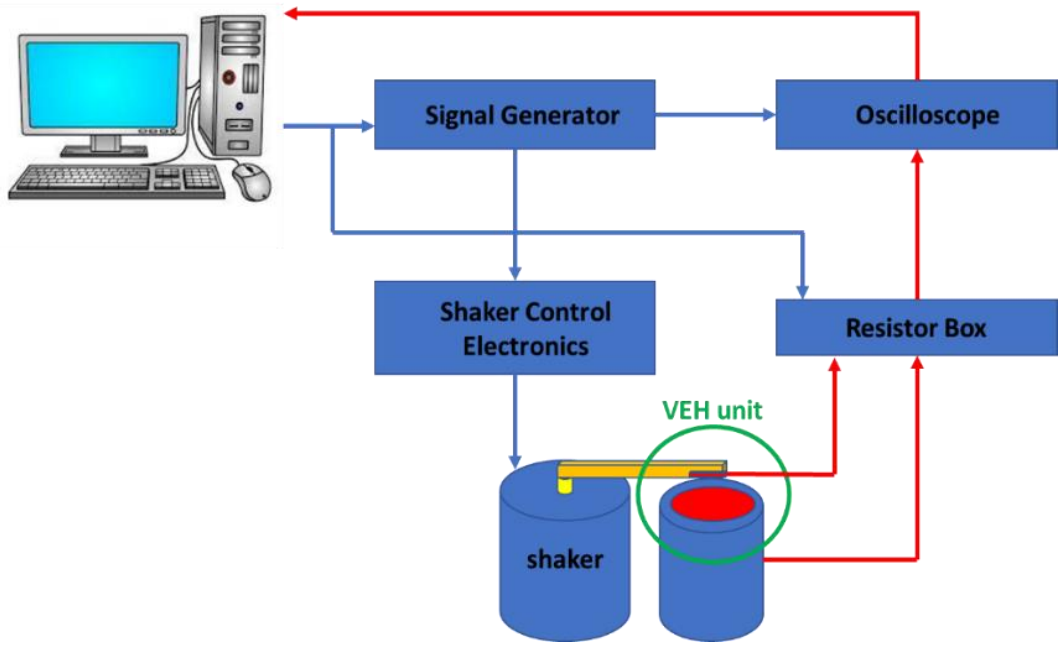

Figure 3.18 – VEH measurement setup diagram of the connections.

A scheme of the connections for the VEH setup is shown in Figure 3.18: in this configuration the upper electrode still oscillates in phase with the shaker, while the lower electrode (orange) is fixed. A μ-metal screen has been places around the shaker, thus suppressing the magnetic field in proximity of the REWoD unit. The height of the lower electrode is tunable by means of a micrometric positioner which allows to preset the distance at rest between the electrodes. A power amplifier (Figure 3.17E) can be used to control and adjust the vibration amplitude of the upper electrode. The REWoD unit is decoupled from the axis of the shaker, the vibration generated by the latter is transmitted to the REWoD unit by means of a beam mounted perpendicular to the axis of the shaker (Figure 3.17A). In this configuration, the upper electrode is oscillated by applying a low-frequency sinusoidal signal in from 1 to 20 Hz. To minimize changes in the position of the drop, placed between the two electrodes, a sinusoidal signal is preferred with respect to more “impulsive” ones, as for instance the “sawtooth” or the square wave signals, to allow for a continuous movement of the electrode, to which a R_{LOAD} load resistor is connected. A resistor box with 7-decade resistors (from 1 Ω to 10 MΩ), controlled by the acquisition Labview software has been used as a variable resistor load (not shown in Figure 3.17). The output signals of the REWoD unit are then visualized and collected by a digital oscilloscope (Figure 3.17F), allowing a shorter acquisition time, that avoid indeed variations in setup beheaviour due to the evaporation of the liquid during the measurement.

The system is able to acquire in real time the potential difference between the top and bottom electrodes, and from this it is possible to determine the instantaneous power transferred to the load, of which an example is shown in Figure 3.19.

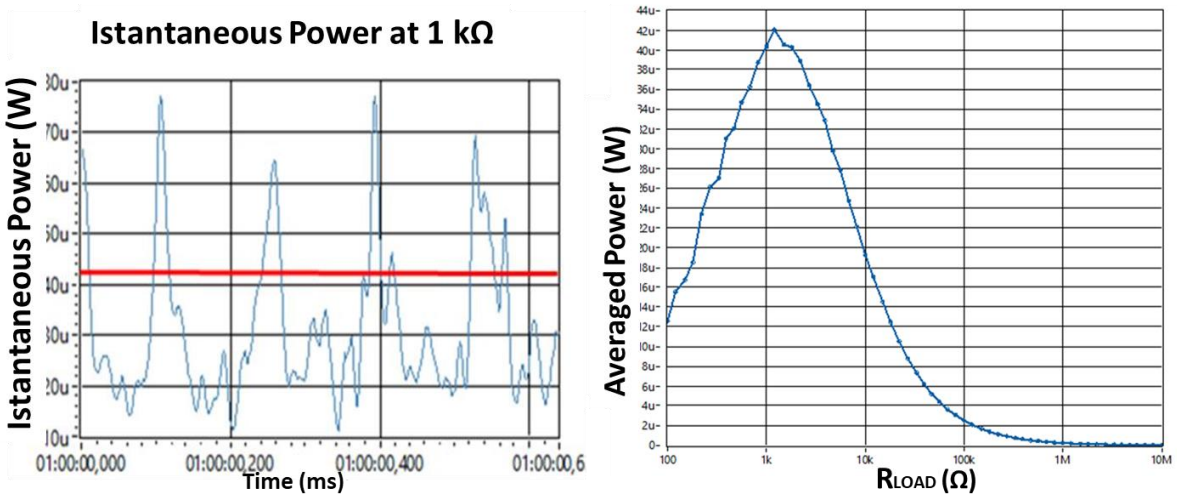

Figure 3.19 – On the left panel, an example of instantaneous power, in accordance with Eq. (3.2). The red line in the panel indicates the averaged power, in accordance with Eq. (3.3). On the right, a measurement of the average power as a function of the load resistance is shown.

Electrical power expresses the electrical energy transmitted by a circuit per unit time, and it is measured in Watt (W). Instantaneous power, transferred to a resistor component is given by

$$P_i(t) = V_L(t) \cdot I_L(t) = \frac{{V_L}^2(t)}{R_{LOAD}}$$

Eq. (3.2)

with $I_L(t)$ being the corresponding instantaneous electrical current flowing along the load. In the case of periodic electrical energy pulses of period T, the averaged (or effective) value of power, namely

$$P_{avg} := \frac{1}{T}\int_0^T P_i(t)dt = \frac{1}{T} \cdot \int_0^T \frac{{V_L}^2(t)}{R_{LOAD}} \cdot dt = I_{RMS}^2 R_L = \frac{V_{RMS}^2}{R_L} = V_{RMS} I_{RMS}$$

Eq. (3.3)

is a more useful information for practical purposes, such as powering electrical devices. In the case of sinusoidally alternating current circuits, electrical power transfer may undergo periodical changes of direction. Since current $I_L(t)$ is a time-varying function, the average electrical power P_{avg} dissipated by a load resistance R_L over time can be determined with the root mean square value of $I(t)$ function, which represents an effective constant current yielding the same power dissipation as P_{avg}.
The digital oscilloscope (D) is used to measure directly the voltage $V_L(t)$ at the ends of the R_L and, by applying this procedure while sequentially changing the load resistance R_L, it is therefore possible to characterize the energy output of the REWoD unit more accurately, identifying the conditions that maximize power transfer to the load (see right panel in Figure 3.19).

Signal acquisitions are performed by the multi-channel digital oscilloscope, computer controlled by a special program in a LabVIEW frame.

3.3.1.1 Instrumental apparatus calibration

Several issues with the VEH measurements setup have been addressed

A) Magnetic disturbance
B) Mechanical resonance of transmission beams
C) Shaker excursion drift, caused by shaker overheating

3.3.1.2 Magnetic flux effect correction

One of the first problems arising with the new configuration of the experimental set up was the detection by the acquisition system of the electromagnetic field generated by the coils actuating the shaker pin. This effect had not been previously observed, since the air-tight cylinder shown in fig. 3A was provided with a metal grid which acted as a shield against signal disturbances of an electromagnetic nature (*e.g.* the 50 Hz mains). The latter was therefore measured, both along the axis of the shaker pin and perpendicular to it, with a Lakeshore Gaussmeter probe, and the results of this measurement are shown in Figure 3.20:

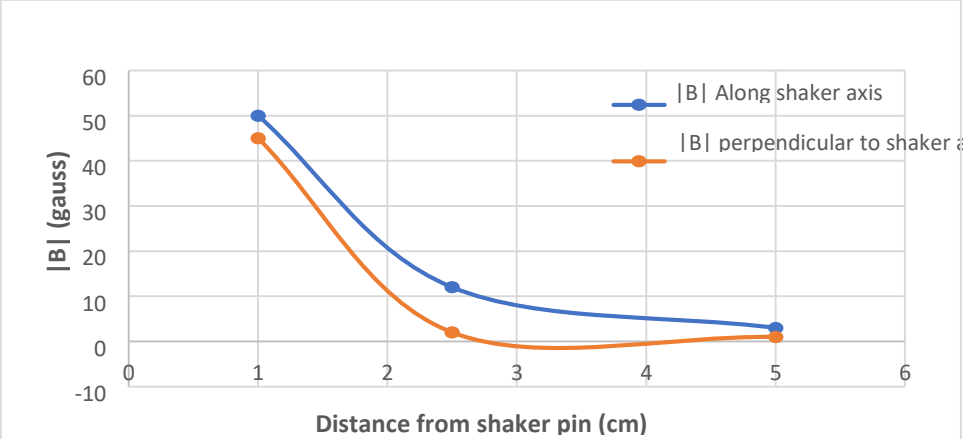

Figure 3.20 – Experimental output of the magnetic component (in modulus) of the electromagnetic field generated during shaker operativity; blue and orange line refer to the magnetic component along the axis of the shaker, and perpendicular to that axis, respectively.

The measurement was carried out by imposing 500 mV on the shaker at the input (corresponding to about 2.8 mm of excursion of the pin, with respect to a maximum available of about 3 mm) and 5 Hz of oscillation frequency. From the graph in Figure 3.20 it can be observed that the magnetic field assumes considerable values close to the shaker, and then reduces to values comparable with earth's magnetic field at about 5 cm from the pin. In addition, in the direction perpendicular to the axis of the shaker, the magnetic field is slightly lower than the one along the axis direction, at the same distance from the pin. This is reasonable because, being outside the axis of the coil that drives the shaker, only a portion of the coil contributes to the field.

At first, long beams to transmit periodic motion of the shaker were used to solve the problem, yet this introduced new problems. The magnetic disturbance issue was definitely overcame by applying a μ-metal cylinder (visible in Figure 3.17), implemented in a second moment due to the need to reduce the weight and size of transmission beams, caused by the instability of the shaker performance due to mechanical resonances of the beams themselves, and the overheating of the shaker during use, which made it difficult to control the beam excursion. The latter issue was related to the presence of the μ-

metal cylinder itself, since it blocked the air vents of the shaker, neglecting thermal moderation of the shaker during operativity.

3.3.1.3 Beam mechanical resonances and shaker excursion thermal drift

Another issue that arose when upgrading the apparatus, was the incapability of finely controlling the pin excursion during the operation of the apparatus: in particular, such excursion appeared to vary unpredictably upon changing excitation frequency, thus causing inconsistencies in sequential measurements. At first it was hypothesized that this effect was due to inertial effects of the mass linked to the pin itself. Further, when driving the apparatus, the transmission beams showed mechanical resonances in the 5-15 Hz frequency range, caused primarily by the length of the beams. Both such issues compelled for lighter and more rigid beams, so that inertial and resonance effects could be reduced, allowing for controllable and reproducible shaker excursions.

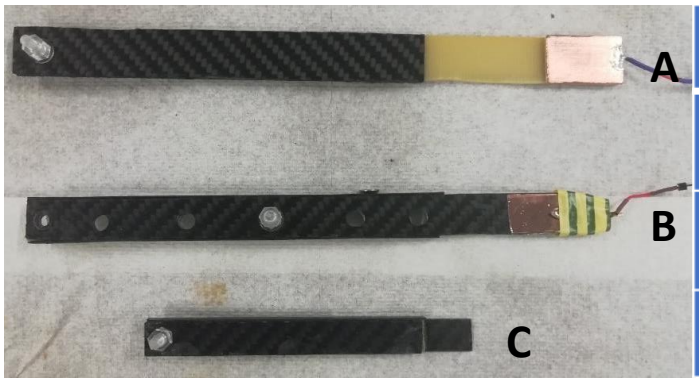

Beam	Weight (gr); Size (mm)
A	26,2 ; 220x18x4,6
B	17,4 ; 180x17x4,1
C	9,4 ; 117x12,5x4,1

Figure 3.21 – On the left, picture of the three transmission beams tested to characterize shaker excursion. On the right, a table describing their properties of interest, namely weight and size.

In Figure 3.21 are shown the beams designed for characterizing the effect produced on shaker excursion by mechanical resonances and inertial effects, along with a chart expressing their properties of interest. Those beams were produced by sandwiching a Vetronit (1306 G-11-H) of density 1.9 g/cm^3 core (3 mm thick for Beam A and 2,5 mm thick for beams B and C between 2 carbon fiber reinforcement platelets, mainly implied because of their strong directional properties. Indeed, by shaping several platelets of such material, a massive (value unfortunately not known being this a prototypical composite material, also obtained by implying an adhesive to attach) resistance could be added to the Vetronit along the covered side. For beam A, the longer one, only 2 opposite sides of the Vetronit were covered Also, beam B was drilled several times, so that to reduce its weight and, hopefully, avoid possible “sail effects” (which actually didn’t show up even for non -drilled beams in a remarkable way), while beam C had additional carbon fiber reinforcements, making it reinforced on 4 sides instead of only 2, as it is the case for beams A and B. that latter solution proved extremely good, in the sense that the 4-fould carbon fiber reinforcement was such that Vetronit core was blocked by 2 couples of strong, vibration-resistant, platelet, instead of only one, rendering it extremely vibration-tough.
To characterize the shaker excursion, a potential difference of 2 V was applied to the bottom electrode, and the beam was equipped with a bare electrode. Since the bottom electrode position, relative to the top one, could be tuned by a micrometric caliber, it was possible to set a desired distance from the top electrode. Then, upon starting the shaker, it was possible to tune its excursion by varying the current driving it, until the oscilloscope detects 2 V for the top electrode, which is the signal corresponding to the contact between the electrodes. In this way, it is possible to determine the half-run (from the starting position, the top electrode moves up and down, so the half-run is measured) as a function of

the voltage measured at the output monitor of the shaker control electronics, which is proportional to the current driving the shaker.

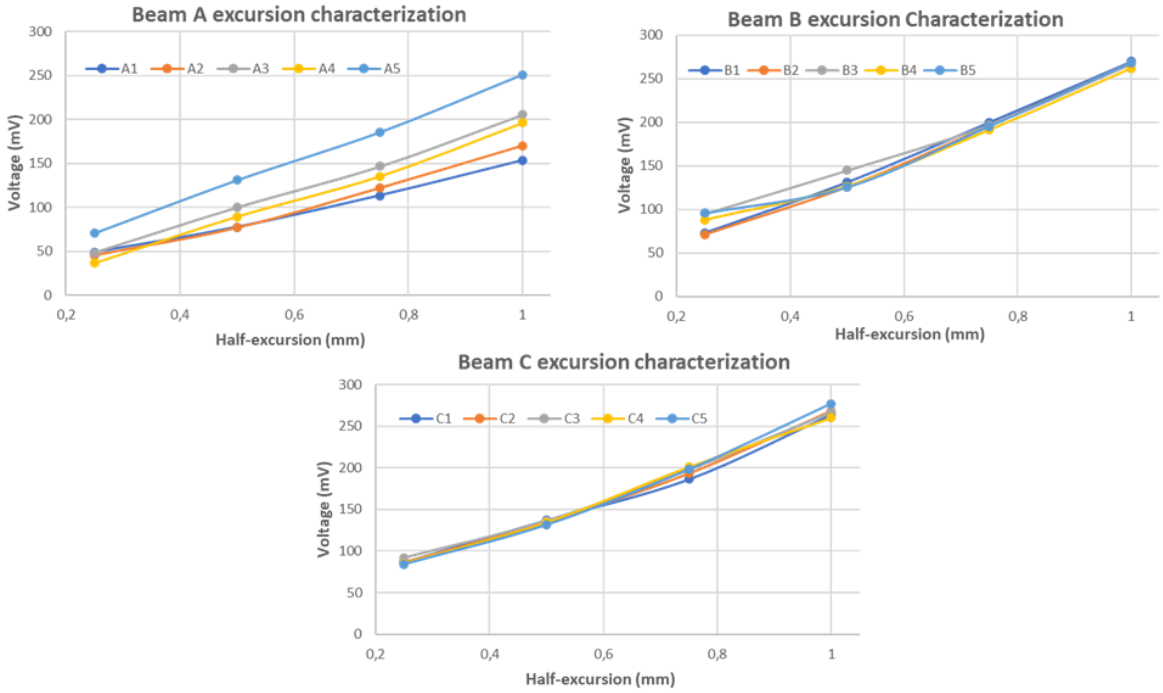

Figure 3.22 – Characterization of shaker excursion as a function of the driving current, for the designed beams at 5 Hz. For each beam, 5 measurement runs have been performed.

In Figure 3.22 the voltage detected by the output monitor as a function of the shaker half-excursion is shown. It is immediately apparent that the beam with larger size, and thus with higher weight, shows the more unstable behaviour, whereas beams B and C exhibit a more reproducible, and more important, also a more coherent behaviour. Such behaviour is also confirmed by the resume graphic in the left panel of Figure 3.23, expressing, for each beam, the averaged value of the voltage output relative to a certain half- excursion, along with a table expressing the relative standard deviations for the respective averaged voltage value:

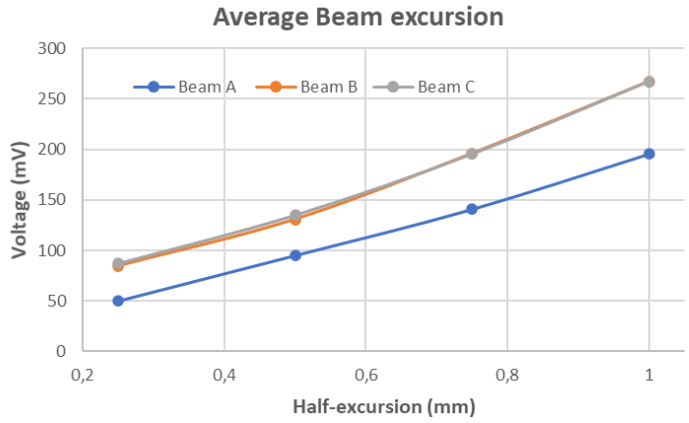

Half-excursion (mm)	St. Dev. A	St. Dev B	St. Dev. C
0,25	12,6	11,8	3,1
0,50	22,3	8,2	2,2
0,75	28,1	3,1	5,7
1,00	37,4	3,1	6,2

Figure 3.23 – On the left, the voltage value as a function of the desired half-run at 5 Hz, averaged over the 5 measurement runs shown in Figure 3.22. On the right, a table containing the standard deviations for each averaged point.

Again, from Figure 3.23 it is evident that beams B and C have the same output signal as a function of the excursion. As apparent from the table in Figure 3.23 the standard deviation for each measured point decreases when switching from beam A to either beam B or C: this indicates that the latter

proved to be mechanically resistant to resonances at frequency as low as 5 Hz, as highlighted by the fact that for beam A, standard deviations increase especially at higher excursions, namely where the so-called swing effect is stronger because of the higher distance of the experimental point to the shaker pin. Here, mechanical resonances increase in intensity because of the Swing effect, where little desynchronizations from the mechanical forcing of the shaker causes the oscillation angle of the beam to increase strongly, just as in normal-life swings.

From such characterization it was hypothesized that the overheating of the shaker could have affected excursion measurements: indeed, for beams A and B, an increase in the current necessary to obtain a certain excursion is observed when performing subsequent measurements. Such overheating effect was unnoticed before enclosing the shaker within the μ-metal cylinder, suggesting it was caused by the cylinder blocking the shaker air intakes. In particular, this would explain the high standard deviation for beam B at 0,25 mm half-excursion, since between acquisitions a certain rest time allows the apparatus to thermalize with the environment. Since such rest time was not monitored, it is likely that the different temperature at which the measurement was started produced the higher dispersion of the voltages measured for the 0,25 mm half-excursion. To determine if the shaker overheating affected the measurements, beam C excursion was characterized at different frequencies, by applying a different procedure: before each measurement, the shaker was actuated at the relative frequency for 30 minutes, to let the apparatus, reach the maximum overheating.

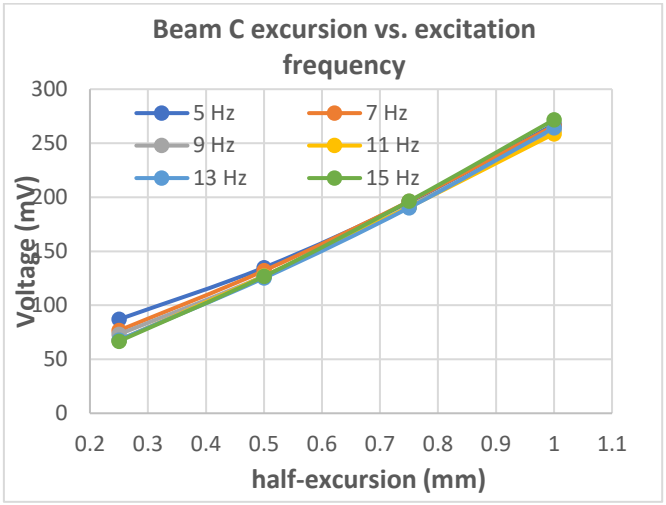

Half-excursion (mm)	5 Hz	7 Hz	9 Hz	11 Hz	13 Hz	15 Hz
0,25	3,1	3,8	1,9	1,2	2,5	0,6
0,5	2,2	1,8	1,9	1,3	0,7	1,6
0,75	5,7	2,7	3,5	2,5	1,9	1,2
1	6,2	2,9	4,0	2,8	2,0	0,7

Figure 3.24 – On the left, characterization of shaker excursion as a function of excitation frequency for Beam C. The run at 5 Hz is taken from Figure 3.23, and it is performed without the precaution to let the apparatus vibrate at the desired frequency for 30 minutes before each measurement. Each curve represents the average over 5 measurements. On the right, standard deviations referring to the averaged points in the left panel.

In Figure 3.24, the experimental output of such characterization is offered: again, a good consistency is observed, indicating that excitation frequency does not affect the shaker excursion, at least not directly. Indeed, by looking at the standard deviations for the 5 measurement runs taken for each frequency, it is observed that the precaution to let the apparatus work for several minutes before the measurement, produces a further decrease in standard deviations, and that effect is more relevant at higher frequencies. This could be reasonable considering that at higher frequencies, the motion of shaker and beams produces a higher interaction of the shaker with surrounding air, making less intense, or at least slowing down the temperature effect.
In conclusion, from the tested beams it was possible to argue that:

- For beam A, both its weight and size, in particular the longitudinal one, affect the excursion of the shaker. The weight appears to affect the rapidity with which the shaker overheats, as suggested by the fact that excursion calibration has different slopes, indicating different behaviours from one measurement to another. For what concerns the length of the beam, upon oscillation the free extreme starts to mechanically resonate, causing it to have a higher excursion than that at the bounded extreme, as indicated by the fact that the contact between bare electrodes happens at lower input currents with respect to beams B and C.
- Beams B and C showed no significant mechanical resonances at 5 Hz, indicating that the mechanical and dimensional properties chosen were sufficient to prevent them. However, for such beams overheating may still affect their excursion as can be observed by the fact that certain calibration runs show a change in the slope during measurements.
- From the calibration of the shaker excursion as a function of the excitation frequency, namely the runs for beam C at 7-15 Hz, it is speculated that frequency also plays a role in moderating the overheating effect: indeed, standard deviations for the input currents at which a certain excursion is obtained, reduces with the increase in excitation frequency. This is reasonable, considering that a higher oscillation frequency produces a higher interaction with surrounding air, and thus, thermal stability.

3.3.2 VEH measurements with micro-structured Al electrodes

The subsequent step regarded the choice of the materials. For the electrodes, again Aluminium was chosen: its low cost, combined with the possibility to tune the properties of its oxide layer, its biocompatibility and, last but not least, the hydrophilic [69, 70] nature of the oxidized surface (which increases the difference of the interfacial areas at the two electrodes), make this material a good choice from several point of views. For the dielectric coating several options were considered, including commercially pre-treated aluminium surfaces, and functionalized surfaces prepared in laboratory, generating the sample set shown in Figure 3.25, namely:

- A: Aluminium (6061 Al alloy) covered by a thin layer obtained by stretching a commercial Teflon™ tape with starting thickness of 76 µm.
- B: Aluminium (6061 Al alloy) covered with a dispersion of Teflon™ nanoparticles in liquid applied via spin-coating method at rotational speed of 1000 rpm
- C: Aluminium (3000 series) covered by a commercial anti-adhesive layer in Teflon™
- D: Aluminium (6060 Al alloy) with micro-textured alumina layer, after the chemical treatment described in 3.1.1.
- E: Anodized Aluminium surfaces commercially available.

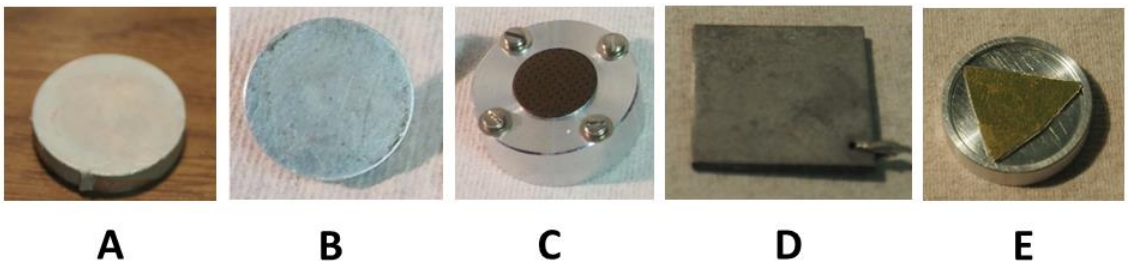

Figure 3.25 – Examples of Al electrodes with different dielectric coating.

From literature analysis the best option for a VEH device suitable for wearable and movable electronics is best achieved with hydrogels instead of droplets, merely because they remove most of the geometrical constraints to EH units, making them more suitable in the optics of developing a prototype for VEH [37]. Commercially available hydrogels, loaded with aromatic molecules and water, were selected; several Al electrodes were produced to work as bottom electrodes, with cavities (hemispherical in case of whole hydrogels, flat for hemispherical ones) suitable to hold hydrogels. The latter solution proved extremely important to pin hydrogels position during measurements, since hydrogels tended to move when pressed by the top electrode. An overall scenario of the selected hydrogels, as well as the molecules embodying, and the bottom electrodes is shown in Figure 3.26.
During the preliminary tests performed to survey the performance of samples A-E dielectric layers, samples B, C and E generated measurable outputs only at about 10 MΩ, this was ascribed to an excessive thickness of the layer itself, causing low EDLCs to be sustainable at the top, dielectric-coated electrode, and thus low voltage drops at parity of load resistance R_L. Electrodes A and D provide measurable outputs and were thus used therefore for VEH.

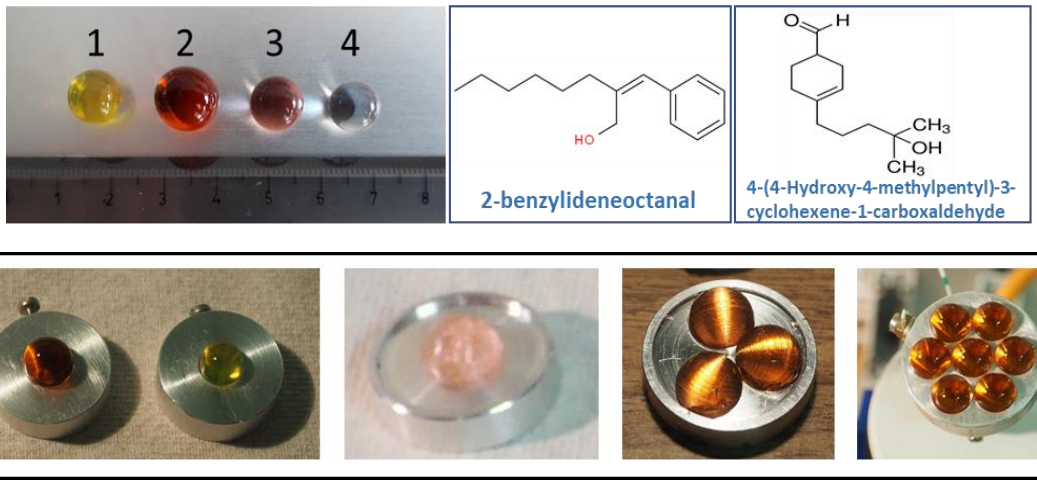

Figure 3.26 – Top: example of commercial PAAm hydrogels initially tested, containing perfumes (1, 2, 3) and water (4), respectively. On the right, two examples of molecules used as smell enhancer in the 1-3 hydrogels. Bottom: examples of the lower electrodes with cavities for holding the hydrogels.

Spherical commercial hydrogels were selected in size and then sliced to obtain a hemispherical hydrogel, by hosting them within appropriate molds. After this, the samples were placed on the lower electrode. To make the various measurements as consistent as possible, in the original apparatus configuration, the vertical position of the upper electrode was calibrated so that it was in contact with the hydrogel with shaker at rest. Each sample was then characterized by applying sinusoidal vibrations of the same amplitude to the system, at different frequencies, *e.g.* 4, 5, 7 Hz.

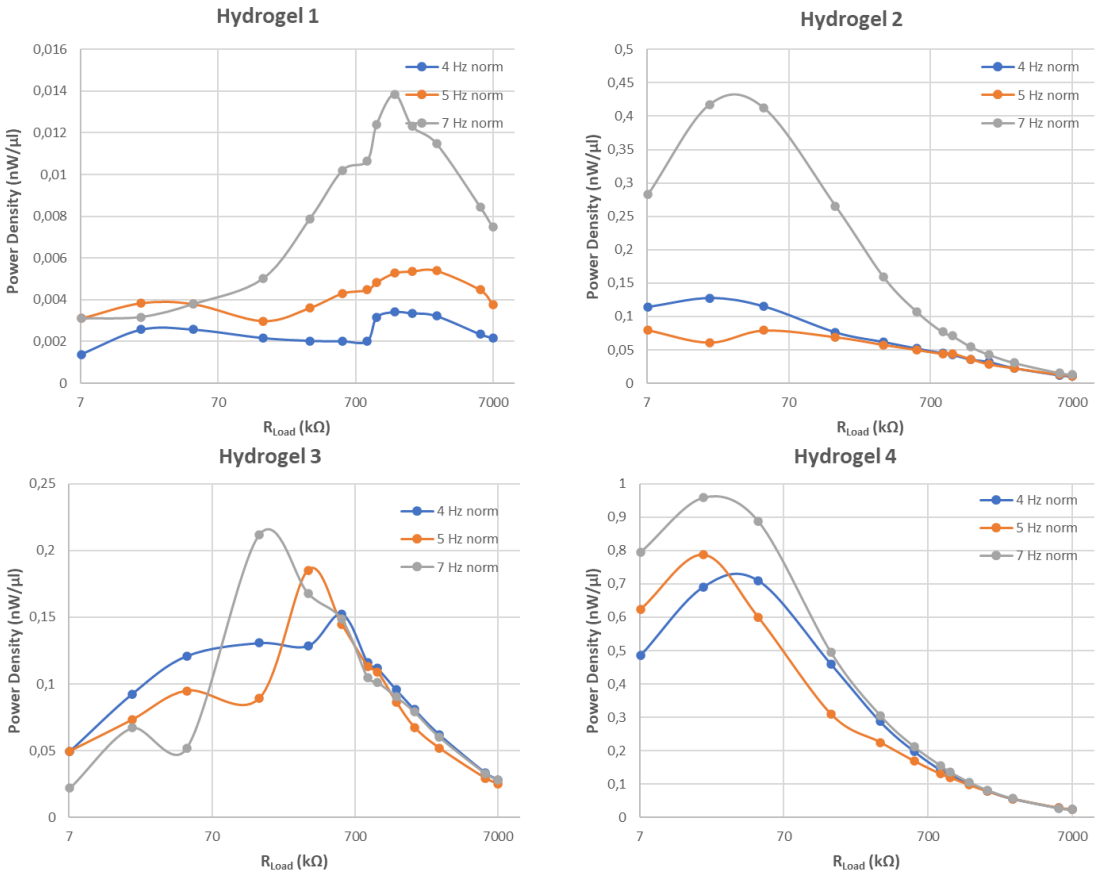

Figure 3.27 – Characterization of power densities harvested as a function of load resistance for different excitation frequencies. Hydrogels containing perfumes (H1, H2, H3) and water (H4). Hydrogels are labelled according to Figure 3.26.

Experimental outputs are reported in Figure 3.27. From this set of measurements, the water-loaded hydrogel (H4) exhibits a higher average power density generated (≈1 nW/µl at 7 Hz, measured at maximum power transfer) at a load resistance of ~20 kΩ. In contrast, hydrogels H1, H2, H3, showed much lower average power densities, and generally the maximum power transfer occurs at higher load resistance. The reason for such behaviour is attributable to the high molecular size of the species with which hydrogels H1, H2, H3 are impregnated, which therefore have reduced mobility within the polymer matrix.

This led to the decision to improve the properties of PAAm hydrogels using D-type hydrogels. The first problem to be solved concerns the speed of evaporation of the liquid from the polymer, which dries completely in about five days, or even faster, depending on environmental humidity.

Indeed, as shown in Figure 3.28, average power densities for dried hydrogels strongly decrease, and most notably, there is an increase in the resistance value at which maximum power transfer occurs, indicating that shrinkage of the polymer matrix causes ionic mobility to reduce within the hydrogel.

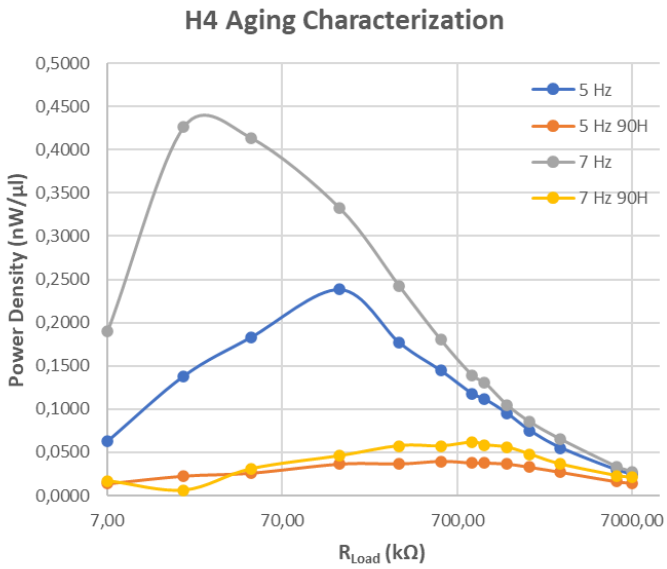

Figure 3.28 – Characterization of average power densities for H4 hydrogels dried for ninety hours, and comparison with the fresh hydrogels. Measurement taken with excitation frequency equal to 5 Hz (as fresh in blue, after 90h in dark orange), and 7 Hz (as fresh in grey, and after 90h in light orange) vibration amplitude equal to 2 mm, and top electrode-hydrogel distance at rest equal to 0.25.

As a first attempt, dried PAAm beads were dipped in a commercially available electrolyte solution of Pb^{2+} ions. However, the spheres grew to a considerably larger size than those soaked in water alone and the elasticity of the polymer lattice was compromised, indicating probable damage to the molecular bonds of the polymeric matrix. This solution was therefore abandoned, and it was decided to use known aqueous saline solutions prepared directly in the laboratory.

Aqueous solutions with different molarities were therefore prepared, using readily available and low-cost salts, as shown in Table 3-4.

In the attempt to increase the adsorption of the solutions at higher concentrations, it was tried to let the beads grow for 24h within the solutions while keeping them at 60°C: this was expected to produce advantages on the growth behaviour, such as i) enlarging the polymer mesh, making easier for solutions to enter it; ii) increasing ionic mobility within the solutions.

Saline Solution	Molar concentration at RT [M]	Molar concentration at 60 °C [M]
LiCl	**5, 3, 1, 0.5, 0.1**	**6.5, 3**
KCl	**4, 3, 2, 1**	**4, 3, 2, 1**
KI	**/**	**0.5**
$MgCl_2$	**/**	**5, 3, 1**
$CaCl_2$	**/**	**4, 2, 1**

Table 3-4: List of prepared solutions for hydrogel swelling

Except for PAAm beads immersed in KCl solutions at room temperature did not show adequate absorption of the solution except at very low concentrations, as evidenced by the final size of the hydrogels. For beads grown in KCl solutions, a comparison of power densities measured is shown in Figure 3.29: despite the non-monotonicity as a function of molarity, a general increase in harvested powers is observed. Hydrogels swollen in intermediate concentrations of KCl solutions, namely 2 and 3 M, proved to be best ones.

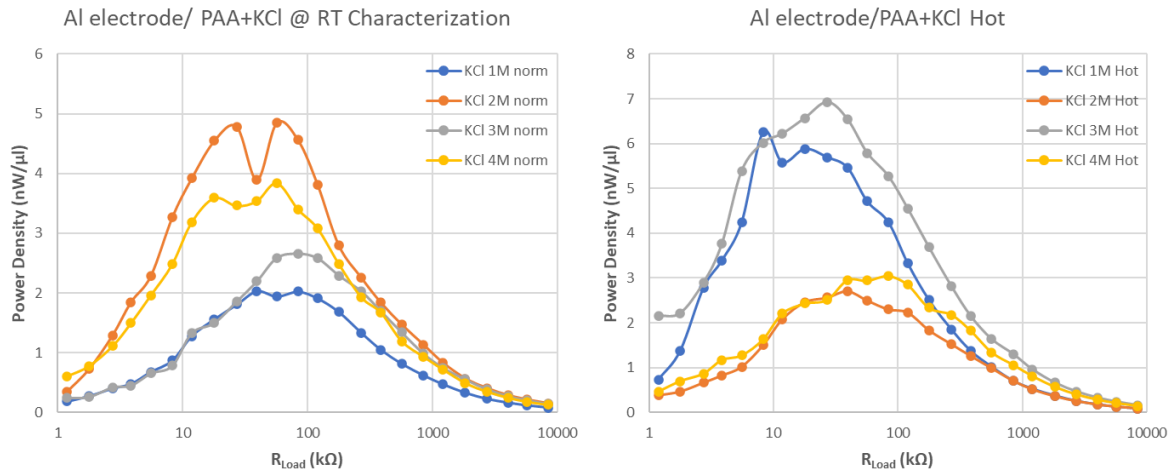

Figure 3.29 – Comparison of the average power densities measured on hydrogels swollen in KCl solutions at RT (left) and at 60°C (right).

Table 3-5 shows the maximum values of the average power densities generated as a function of the salt solution used and the corresponding load resistance. No measurements could be made for $CaCl_2$ because the absorption of the solution was so limited that spheres could not reach a usable size.

PAAm hydrogel loaded with saline solution at 60°C	Average power density [nW/µl]	Load Resistance R_{Load} [kΩ]
KCl 1M	5.88	17
KCl 2M	2.7	39
KCl 3M	6. 92	27
KCl 4M	3.04	56
KI 0.5M	0.52	173
MgCl2 1M	0.65	119
MgCl2 3M	1.16	119
MgCl2 5M	1.31	119
LiCl 3M	0.71	268
LiCl 6.5M	2.16	83

Table 3-5: Power densities measured at the maximum power transfer for the hydrogels swollen in saline solutions at 60°C

From the data in the Table 3-5, it can be seen immediately that the highest average powers are obtained with the hydrogels containing the KCl solutions. However, the development of this system has not been continued for the following reasons:

- High evaporation rate. As can be seen in Figure 3.30, there is rapid evaporation from the surface of the hydrogel as early as three hours after extraction and total evaporation in three days, leaving the salt on the surface and the inside of the sphere completely hollow. For the same reason, it is speculated that the low affinity between the embodied solution and the hydrogel matrix causes part of the liquid to be ejected from the hydrogel itself during the measurement, and to wet the top electrode, thus generating an increase of the surface charge sensed by the latter. Despite this enhances power outputs, it drastically reduces the device lifetime.

Figure 3.30 – On the left, three PAAm hydrogels at different times after being extracted from KCl 0.5 M (at 60°). From left to right, hydrogel as extracted from solution, hydrogel 3 hours from extraction, hydrogel 3 days from extraction. On the right, hydrogel swollen in 6.5 M LiCl solution at 60°C, 5 days after extraction.

- During the salt absorption phase, the hydrogels have reached a larger final size than those grown in other solutions: however, because of the high volatility shown by the embodied solution for this system, it is expected that upon squeezing there is a release of liquid from the hydrogels, positively affecting the measured power densities, but drastically harming hydrogels lifetime.
- KCl is a salt with maximum solubility in water (at 20 °C) equal to 4.55 mol/l. As the final aim is to improve the charge density incorporated in the PAAm sphere, salts with higher solubilities are preferable, e.g., LiCl (maximum solubility at 20°C = 19.87 mol/l).

For LiCl 6.5M at 60°C, the average powers observed were lower than those observed for KCl, but an almost negligible evaporation rate was observed (see Figure 3.30). Leaving some of the spheres in the air in the middle of the summer, unlike all the others, they retained their elastic properties, and no salt crystallisation was observed at the surface even after five days. The average power response generated is slightly reduced but is consistent with those measured previously. This allowed to indicate LiCl as the best salt to incorporate into the spheres both in terms of measured power and longevity.

3.3.3 Development of air-tight prototypal device

To reduce evaporation rate during measurements, an air-tight device was designed and improved. Indeed, the experimental outputs shown in Table 3-5 were obtained by housing the EH unit within an air-tight cylinder, consisting of a transparent Plexiglas tube, threaded at the ends so that two aluminium caps could be screwed on, which acted as supports for the two electrodes housed within the device, as shown in Figure 3.31A.

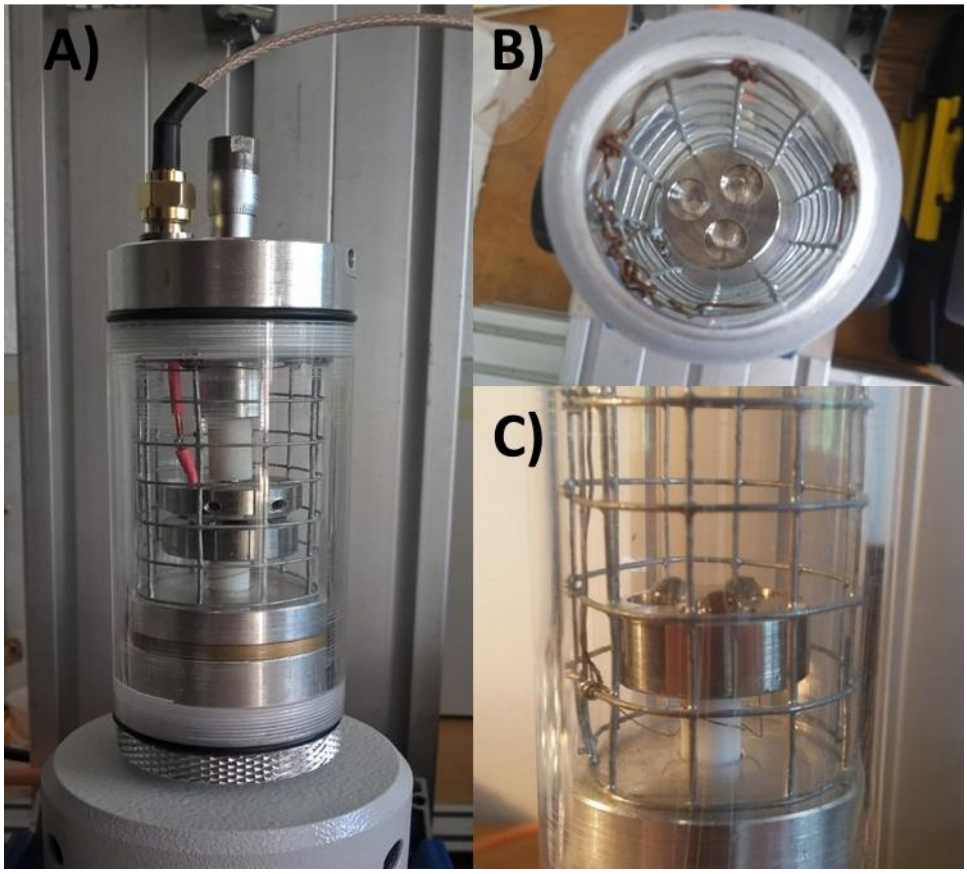

Figure 3.31 – Air-tight cylinder for VEH characterization. A) Side view. B) Top view. C) Side view, with 3 hydrogels hosted.

The watertight container housing the electrodes is directly connected to the vibration system by a screw attachment. The vibration is therefore transmitted by a spring connected to the lower electrode. Once closed, the position of the top electrode is tuneable thanks to a micrometric calibre. The system thus created allows operation in a frequency range of ~5 Hz to ~30 Hz, above which excessive mechanical resonances occur. This solution solved the evaporation problem by allowing the same system to be worked on for several days without any appreciable change in the hydrogels, thus producing reproducible results. However, because the EH unit was housed within that container, it was not possible to determine the excursion of the lower electrode, but only the vibration frequency. This system allowed for measurement of more hydrogels at once, and to tune the best working distance between top electrode and hydrogels.

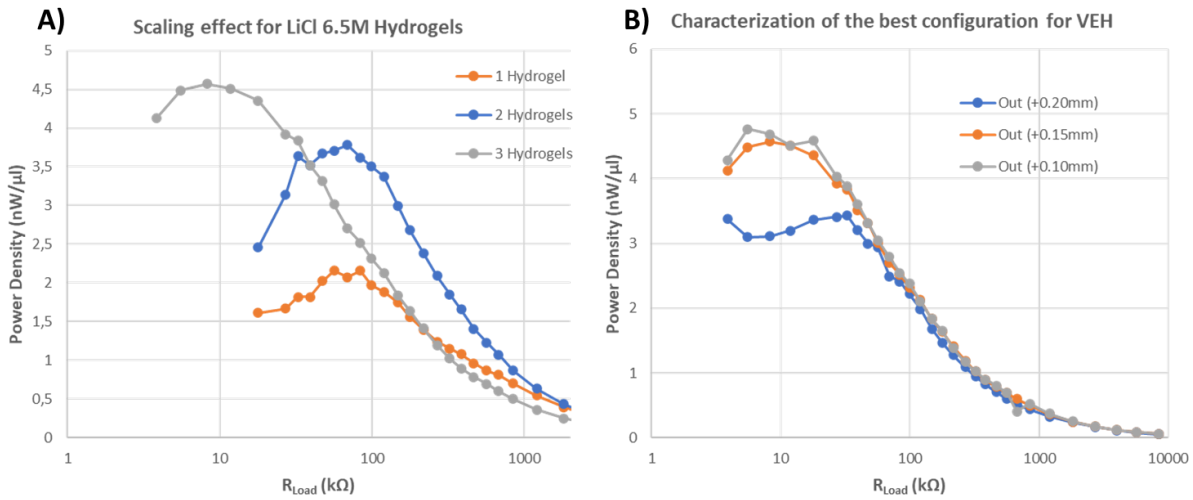

Figure 3.32 – On the left (Panel A), experimental characterization of the scaling effect of EH behaviour. On the right (Panel B), characterization of the best working distance between hydrogels and the top electrode with 0.05 mm increments of the rest position. For both panels, hydrogels swollen in 6.5M LiCl solutions at 60 °C for 60 min were used, and tests were performed at 6 Hz.

Figure 3.32 shows the main results obtained on this system: in the left panel, power densities as high as 3.78 nW/µl with 70 kΩ load resistance were obtained for 2 hydrogels working at the same time, and 4.57 nW/ µl for 3 hydrogels.

Indeed, as can be observed in the right panel of Figure 3.32, for 3 hydrogels the maximum power transfer occurs at about 10 kΩ, this is due to a reduction of the internal resistance due to the parallel connection of the hydrogels. Also, it is worth noting that the distance between the hydrogels and the top electrode at rest is a critical parameter for the proper operation of the device. Even a small change in that distance can lead to a degradation of the VEH performance, as shown in Figure 3.32B, due to desynchronization of the active hydrogels, as already observed in literature [36].

3.3.4 Hydrogel drying curves

In the previous part of PhD, commercially available polymer gels loaded with water and saline solutions were tested to essay the VEH device output performances: Polyacrylamide (PAAm) gels loaded with aqueous LiCl solutions at 60 °C offered the best results for VEH. Since evaporation of the medium contacting the electrode is a significant concern because it impacts power generation, PAAm hydrogels deswelling properties have been further characterized.

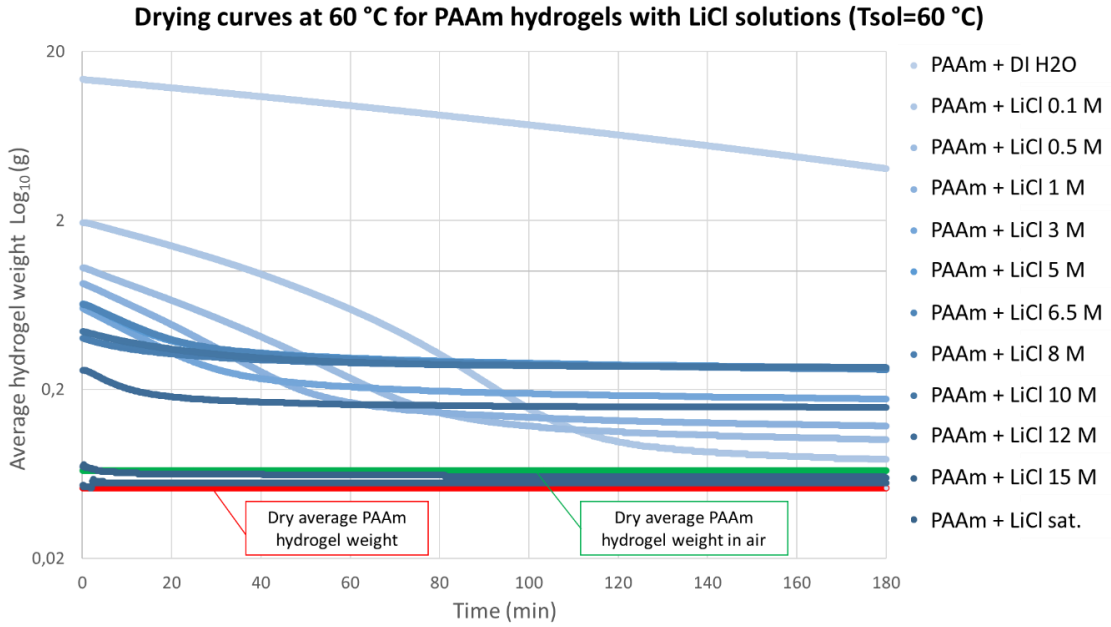

Figure 3.33 – Average hydrogel weight as a function of deswelling time at 60°C, for PAAm hydrogels swollen in LiCl (solution temperature = 60 °C) at different concentrations (see legend on the right). The average weight (over 11 hydrogels) for a dry PAAm hydrogel (red), after drying at 60 °C, and exposed to the humidity of the air (green) are shown as a reference.

Hydrogels were loaded with LiCl solutions at T_{swell} = 60 °C, then dried for three hours within a thermobalance at a constant temperature of 60 °C, to avoid any deterioration of the polymer. The PAAm hydrogel weight curve has been recorded every minute, as reported in Figure 3.33 for different concentration of LiCl solution. A decrease in hydrogel starting weight with the increase in LiCl concentration is evident: the more the water coordinates with ions in the solution, the less it interacts with the hydrogel, thus causing a lower amount of solution to be embodied in the polymer network. Indeed, for very high LiCl concentrations, the hydrogel swelling is minimal. However, at the same time, the increase in concentration causes the swollen hydrogels to be more resistant to evaporation: this confirms that not only water is adsorbed, but also ions in solution are drag by water inside the hydrogels; it also confirms that the ion concentration in the hydrogel scales with the concentration of the solution. When swelling occurs, the weight during drying *p(t)* was found to be following the equation:

$$p(t) = p_0 + Pe^{\frac{-(t-t_0)}{\tau}}$$

Eq. (3.4)

where p_0, P, are the minimum and starting weight, respectively, t_0 is the time at which the hydrogel weight stabilizes.

The drying curves have been fitted according to Eq. (3.4) (see Table 3-6) to determine the deswelling characteristic time τ at a drying temperature of 60 °C, reported as a function of LiCl molarity in Figure 3.34 for different hydrogel hydration temperatures (RT and 60°C).

Hydration Temp. T_{hydr} RT	Mol. LiCl	t_0 (s)	p_0 (g)	τ (s)	τ (min)	P (g)
	0,1	144	-0,004	2181	41	2,143
	1,0	100	0,110	1395	27	0,818
	5,0	10	0,260	1117	19	0,451
	6,5	0	0,303	1284	21	0,410
	8,0	45	0,315	1579	26	0,358
Hydration Temp. T_{hydr} 60 °C	**Mol. LiCl**	**t_0 (s)**	**p_0 (g)**	**τ (s)**	**τ (min)**	**P (g)**
	0,1	200	-0.051	2964	49	2
	0,5	70	0.082	2002	33	0.983
	1,0	60	0.12	1440	24	0.748
	3,0	-10	0,183	1128	19	0,438
	5,0	-70	0,280	1106	18	0,382
	6,5	-50	0,275	1181	20	0,379
	8,0	-100	0,274	1555	26	0,125
	10	15	0,272	1549	26	0,164
	12	-60	0,159	843	14	0,105

Table 3-6: Fit parameters for PAAm hydrogels drying curves according to Eq. (3.4).

The deswelling characteristic time for PAAm hydrogels, hydrated at 60 °C, presents a local maximum between 6-8 M molarity range of LiCl solution (see Figure 3.34).

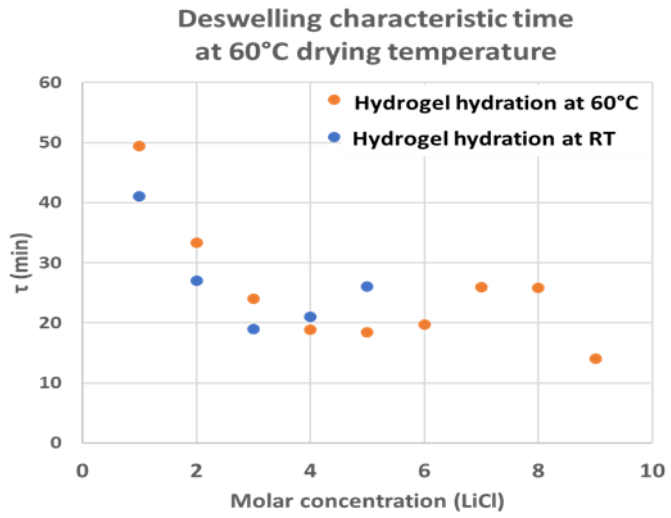

Figure 3.34 – Deswelling characteristic time τ (at 60°C) for different hydration temperatures (RT, 60 °C) as a function of LiCl solution molar concentration

The starting (wet) and the final (dry) weights of PAAm hydrogels, hydrated at RT and 60°C are reported in Figure 3.35 (left panel) as a function of the molarity. To reduce the error of the measurement during drying, the weight of a single hydrogel has been averaged over eleven samples. The hydrogel diameters have been measured as a function of the molarity and the results are reported in Figure 3.35 (right panel). From those data the weight of LiCl salt into PAAm has been determined and reported in Figure 3.36.

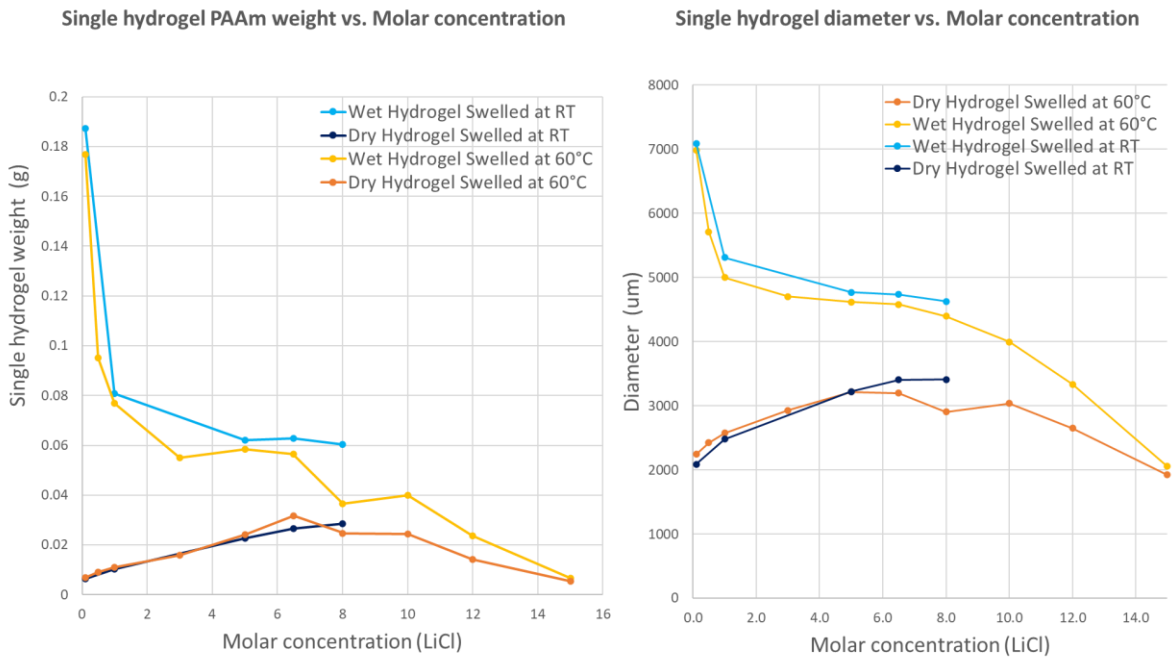

Figure 3.35 – Average single PAAm hydrogel weight (left) and diameter (right) for different hydration temperatures (RT, 60°C) as a function of molar concentration of LiCl solution.

The PAAm hydrogels, hydrated at 60 °C, present a maximum amount of LiCl salt for molarity from 5 to 10 M, while the diameter remains within the range appropriate for VEH up to a concentration of 8 M. Interestingly, the value for which the best VEH has been found in this study is 6.5 M.

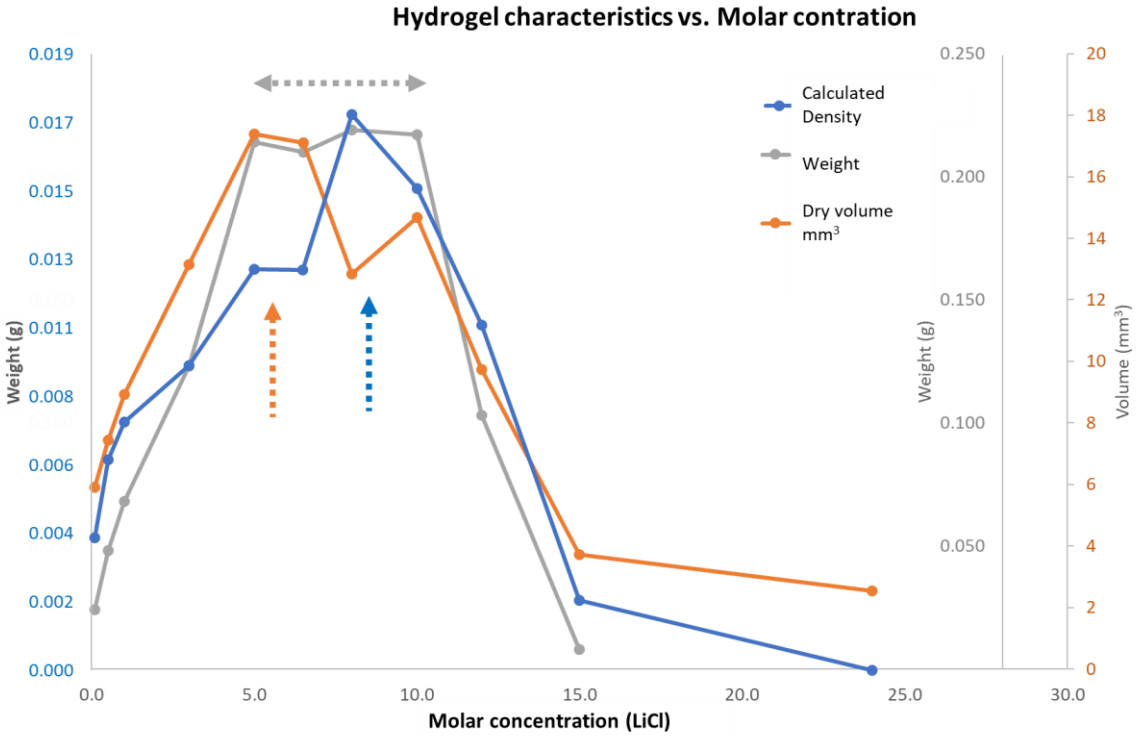

Figure 3.36 – Dried PAAm hydrogel weight, after deswelling at 60°C, as a function of LiCl solution molarity. Measured dried PAAm weight (grey), measured dried PAAm volume (orange), calculated hydrogel density (blue)

3.3.5 Discussion

The behaviour of the liquid soaked PAAm spheres has been attributed mainly to the hydration properties of the ions in aqueous solutions. Water is a strongly structured liquid, due to the strength of its hydrogen bonds [93]. In describing the hydration properties of ions, Samoilov [94, 93] postulated a model for treating hydration of ions in a general way by looking at the ratio between the average residence time of a water molecule near another water molecule in the hydration shell of an ion, thereby named τ_{ion}, and the same value obtainable in pure water (τ_{water}, equal to 1.7 ns), obtaining the following relationships:

$$\tau_{ion} / \tau_{water} = e\text{^} (\Delta E / RT)$$

Eq. (3.5)

where ΔE is the difference in Gibbs free energy of exchange between H_2O molecules, for a molecule in the ion hydration shell and for one in pure water. Based on the sign assumed by this ΔE a distinction is made between *positively hydrated* ions (for $\Delta E>0$, $\tau_{ion} / \tau_{water} > 1$) and *negatively hydrated* ions (for $\Delta E<0$, $\tau_{ion} / \tau_{water} < 1$); another way to classify ions upon their hydration properties in water is between *structure making* and *structure breaking* ions [95], namely between ions that increase the structural order of water and ions which destabilize it.

Ione	**Li^+**	**K^+**	**Cl^-**	**I^-**	**Mg^{2+}**	**Ca^{2+}**
ΔE (kcal/mole)	0,73	-0,25	-0,27	-0,32	2,61	0,45
τ_{ion}/ τ_{water}	3,48	0,65	0,63	0,58	86,3	2,16

Table 3-7: Experimental difference of Gibbs free energies of exchange (ΔE) and ratios τ_{ion}/ τ_{water} for several ion species [94].

The value reported in Table 3-7 for the difference in Gibbs free energy of exchange, as well as their τ_{ion}/ τ_{water} ratios, could help explain the behaviour observed by our hydrogels:

1) For PAAm hydrogels embodying KCl solutions, the highest power outputs are observed. However, it also showed the highest evaporation rate among the PAAm swollen in solutions at 60 °C. This is consistent with the fact that KCl is composed by two ionic species with "negative hydration" behaviour: it is therefore postulated that during VEH measurements, the hydrogel polymeric matrix could not hold the adsorbed solution efficiently, thus causing ejection of the latter and an increase in measured power outputs.

2) For PAAm hydrogels embodying KI solutions, the same tendency to evaporation is observed, but outputs are quite lower. As for KCl, this salt is composed by two negatively hydrated ionic species, but in this case the I^- ion has an ionic radius quite larger than that of Cl^-, making quite hard for the former ion to deepen the polymer bead. Those hydrogels grew more than others, but it is speculated they mainly absorbed water. Such hypothesis is supported by the behaviour of hydrogels swollen in $CaCl_2$ solutions, as discussed later.

3) For PAAm hydrogels embodying LiCl solutions, despite the slightly lower values of power generation, an almost null evaporation rate ensures long operativity lifetimes. For this solution, the action of the positively hydrated Li^+ ionic species guarantees stability within the polymer matrix.

4) For PAAm hydrogels embodying $MgCl_2$ solutions, a behaviour in power output like that observed for hydrogels loaded with LiCl, but not the same resistance to evaporation: again, this was attributed to the larger ionic radius of Mg^{2+}, which caused a lesser absorption of the latter within

the polymer matrix. This assumption is also confirmed by the hydrogels swollen in $CaCl_2$ solutions: in this case, the ionic radius of the positively hydrated species, namely Ca^{2+}, is even larger, and indeed the final size of the swollen hydrogels was very low, indicating that the "structure making" effect of Ca^{2+} was so intense that water preferred to coordinate with the salt than with the polymer beads.

Figure 3.37 shows a comparison of the results obtained with 3 hydrogels (6 mm diameter each) in parallel of PAAm with LiCl and PAAm with DI H_2O only. On the secondary axis on the right, the output voltage at the ends of the electrodes is shown.

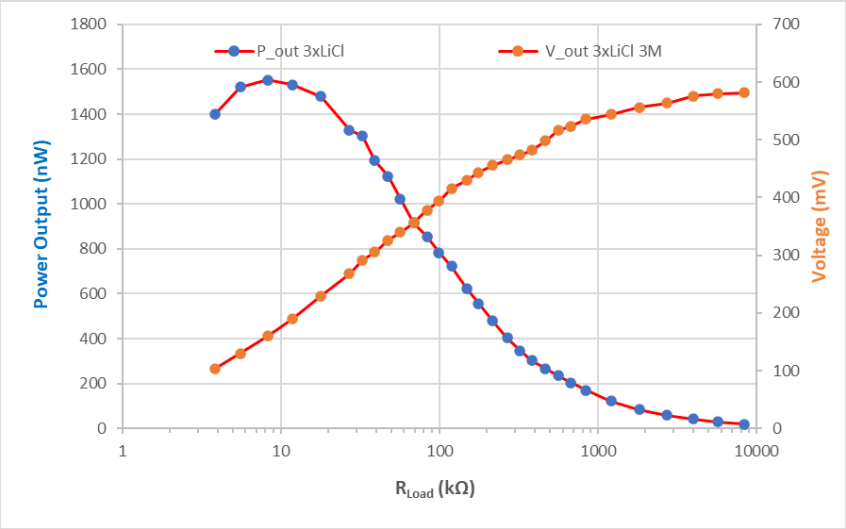

Figure 3.37 – Average power generated and output voltage as a function of load resistance R_{Load}, for 3 hydrogels loaded with 3M LiCl solution at 60°C.

The results achieved so far, although still presenting wide margins for improvement, have already made it possible to generate average micropowers comparable to, and in some cases greater than, those reported in the literature, permanently resolving the problem of evaporation during ageing. This makes it possible to make better use of this technology in devices that are not totally hermetic. PAAm hydrogel has demonstrated good compatibility with LiCl as an ionic conductor. However, the Cl^- ion has so-called *negative hydration* behaviour and is corrosive in nature, which limits the possibility of using low-cost metal electrodes. Thus, it was decided to replace Cl^- with another ionic species, such as SO_4^{2-} which is a borderline case between positive and negative hydration [93].

4 VEH with fluoropolymer-coated electrodes

Results in previous chapter showed that is possible to develop a laboratory-scale prototype by exploiting chemically etched commercial aluminium alloys (6061 series) in combination with PAAm hydrogels embedding LiCl solutions by a thermal treatment allowing to strongly mitigate the water evaporation over time, thus increasing the device lifetime. However, the interaction between hydrogels and micro-structured surfaces leads to a progressive deterioration of the hydrogel itself. In order to improve performance and, at the same time, allow a future miniaturization of the device, it is necessary to create dielectric layers of nanometer thickness with high relative dielectric constant. In addition, the thickness and density of the dielectric film are also important factors in determining the breakdown voltage and the leakage current, which are limiting factors in energy harvesting. It was then considered the use of the thermally treated hydrogels previously discussed with fluoropolymer-coated electrodes, which belong to the wider family of Advanced Engineering ThermoPlastic (AETP).

AETP, or superpolymers, are distinguished by their unparalleled thermal, mechanical, and chemical properties and are at the top of the plastics performance pyramid (see Figure 4.1). Continuous technological advances have had an even greater impact on our lives, and the ETP has further penetrated metal-dominated markets. As metal substituents in the construction of mechanical appliances, ETP offers such advantages as corrosion resistance, transparency, lightness, self-lubrication and economy in production and decoration. Replacing metals with plastic is favoured since the physical properties and operating temperature ranges of plastic reduce cost and increase productivity. The ability to replace metals in many areas has led to huge growth in the ETP. A driving force behind the ETP's growth is the continued expansion of electrical/electronic markets, which requires smaller, lighter components that operate at higher speeds. In addition, the same requirements are driving the automotive market segment. Original equipment manufacturers aim to reduce production costs, style flexibility, reduced maintenance, and more efficient, less polluting vehicles that use materials with better performance under the hood and in exterior components.

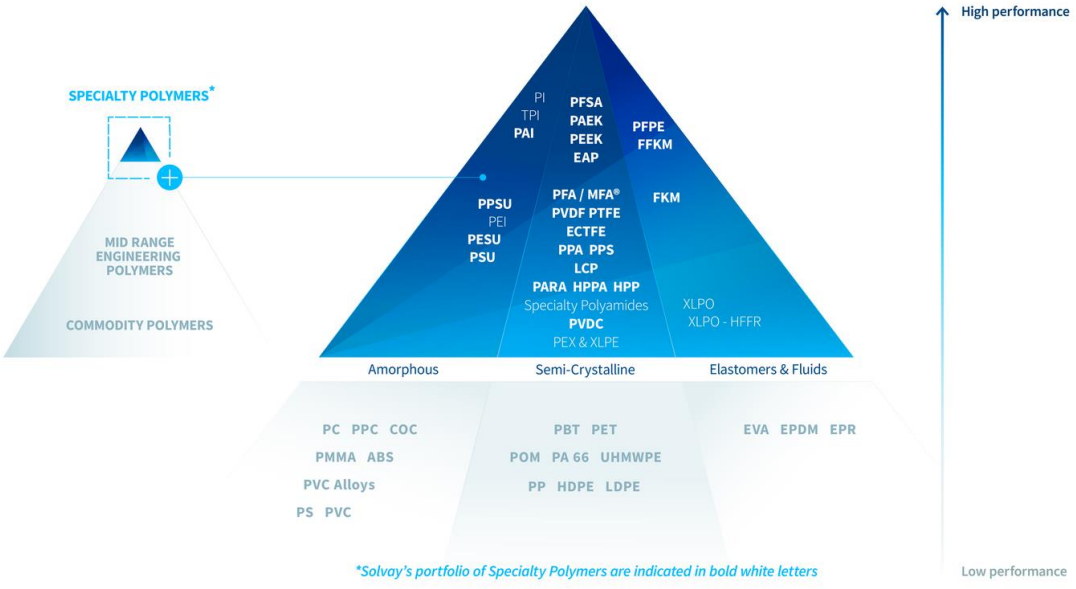

Figure 4.1 – A list of the most relevant "superpolymers" [96].

Fluoropolymers were selected as they are largely known as the most hydrophobic polymers. To select the fluoropolymer for VEH test, several options listed below have been considered:

Poly-Tetra Fluoro Ethylene (PTFE): with monomer chemical formula (C_2F_4), such compound is commonly known under the brand name Teflon™ and represents 60-65% of worldwide fluoropolymers production [97]. Mainly known for its anti-adhesive properties, PTFE is a high-performance polymer: the fluorine group and its properties (such as low electric polarizability, the highest electronegativity, and a short Van der Waals radius of 1.32 Å) combined with the strength of C-F bond (485 $kJ \cdot mol^{-1}$), make PTFE a chemically and thermally stable, hydrophobic fluoroplastics suitable for anti-friction components (lubricants, coatings, etc.) and dedicated industry ranging from aerospace to electronics and textiles.

Fluorinated Ethylene Propylene (FEP): quite similar to Teflon™, FEP is a copolymer formed by TetraFluoroEthylene (see above) and HexaFluoroPropylene (C_3F_6). This fluoropolymer can match Teflon™ chemical inertness but is melt-processable, being suitable for conventional techniques such as injection moulding and extrusion. Its applications include chemical/medical equipment, as well as coating agent for wires and solar panels, due to high weather resistance and optical transparency.

Poly-Vinylidene Fluoride (PVDF): it is a semicrystalline fluoropolymer with repetition unit (CH_2CF_2), and has good mechanical, chemical, and thermal properties, and because of its high dielectric constant (ε_r) and dielectric strength is also of interest as dielectric capacitor film.

PTFE, FEP and PVDF present high hydrophobicity, good dielectric properties. In the present work, it was decided to use as dielectric layer PVDF instead of PTFE, because PVDF offers the advantage of being soluble in green solvents, allowing thus for further functionalization of the thin dielectric layers with additives to enhance the VEH performance. Lastly, its piezoelectric properties could allow for realization of hybrid EH devices, such as Piezo-Tribo-Electric energy transducers.

4.1 PVDF-coated electrodes

4.1.1 PVDF

A polymer of great interest for its excellent chemical and physical properties and for its relatively high relative dielectric constant of average value ε = 12 [98, 99, 100, 101].
PVDF is a linear homo-polymer obtained by the repetition of vinylidene fluoridemonomers (CH_2-CF_2), synthesized through a radical polymerization. It has a dipolar polarization that finds its origin in the orientation of the dipoles or the asymmetry of the functional groups. It is known, in fact, that the atoms of F compared to those of H and C can lead to a strong electric dipole moment of the PVDF monomer. In this way, each VDF unit possesses a dipole moment perpendicular to the polymer chain, which is the predominant polarization of the polymer. Further, it is a partially fluorinated semi-crystalline polymer, whose crystalline phase, which largely contributes to the value of relative dielectric constant, can vary from 35% to 70% depending on the characteristics of the chain, the polymer deposition process or on the subsequent thermal, mechanical or electrical treatments [99]. The crystalline phase of PVDF can take five different conformations, depending on the rotation of the C-C bond. The main phases, briefly described below and shown in Figure 4.2, are α, β, γ while the presence of the δ and ε phases is normally negligible.
Phase α with alternation TGTG' (trans-gauche-trans-gauche) has a unit cell with **a** = 4.96 Å, **b** = 9.64 Å, **c** = 4.62 Å and with all angles equal to 90°. This phase is the most energetically stable. In this crystalline conformation the cellular unit does not show polarization since the alternating chains are packed with their c-shaped dipoles in antiparallel alternation.
Phase β with alternating TTTT (all trans planar zigzag) has a unit cell **a** = 8.58 Å, **b** = 4.91 Å, **c** = 2.56 Å. This phase has the fluorine and hydrogen atoms in the opposite direction, thus forming a high density of dipoles aligned with each other in the same direction. This conformation makes the phase energetically less stable but with higher values of spontaneous polarization, piezoelectric coefficient, and relative dielectric constant.
Phase γ with alternation T_3GT_3G' has a unit cell with **a** = 4.96 Å, **b** = 9.64 Å, **c** = 9.24 Å and all angles at 90° (equal to α but with **c** twice as long). This phase is present more frequently when the polymer has high molecular weights.
Fase δ like α but with an alternation TG'TG.
Fase ε like α but with an alternation $T_3G'T_3G$.

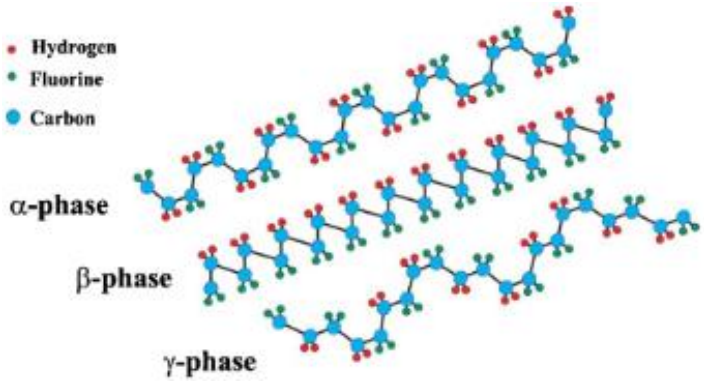

Figure 4.2 – Conformation of the chains for the main crystalline phases α, β and γ of PVDF [102].

It is possible to favour one phase over the others, both in the crystallization stage and after through appropriate post-deposition treatments. A schematic view of some of the possibilities is shown in the Figure 4.3 [98]:

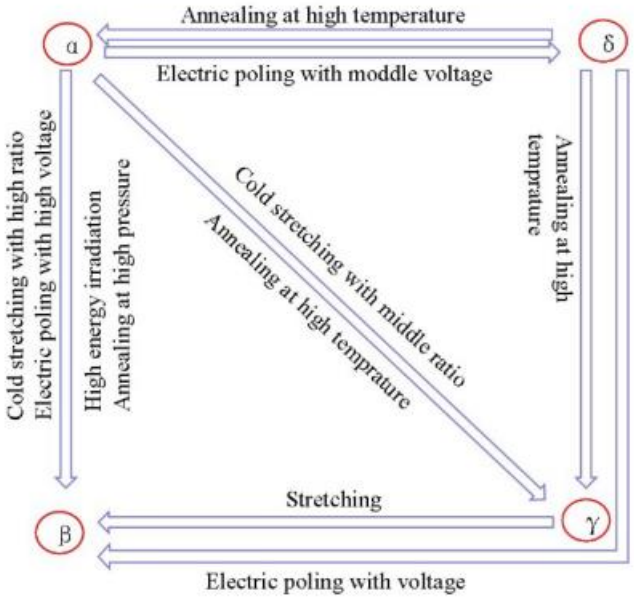

Figure 4.3 – Reversible transformation pathways and different manufacturing methods for PVDF [98].

PVDF is typically dissolved in polar solvents such as Dimethylformamide (DMF), N-Methyl-2-pyrrolidone (NMP) or dimethylacetamide (DMAc) [103].
For this activity a green solvent has been used. Dimethyl sulfoxide (DMSO) is a polar aprotic solvent and is less toxic than other members of this class, such as dimethylformamide, dimethylacetamide, N-methyl-2-pyrrolidone and HMPA. DMSO is often used as a solvent for chemical reactions with salts, especially Finkelstein reactions and other nucleophilic substitutions. It is also widely used as an extractant in biochemistry and cell biology. Since DMSO is only weakly acidic, it tolerates relatively strong bases and is therefore widely used in the study of carbanions. In DMSO solution, a set of non-aqueous pKa values (acidity C-H, O-H, S-H and N-H) was determined for thousands of organic compounds.

4.1.2 PVDF solution deposition techniques

Among the various techniques [104] suitable for producing polymeric thin films, drop casting and spin coating were considered of interest for the purpose of the present Thesis. These techniques were selected because of their compatibility with the polymer of interest, for the availability of the corresponding equipment and for the need to produce films in a short time with good reproducibility.

Drop casting: consists of dropping a few drops of solution onto a substrate, as shown in Figure 4.4. The solvent contained in the solution evaporates spontaneously, resulting in a solid film. The thickness of the film is proportional to the concentration of the solution. The advantages of this technique are its simplicity and the small amount of material required for deposition. Disadvantages include the difficulty in controlling the thickness and the low uniformity of the deposited film.

Figure 4.4 – Schematics of the drop casting method, here for a solution of PVDF in DMSO [104].

Spin-coating: is a simple method that allows direct deposition of the film onto the substrate with facile control of the film thickness from a few nanometres to tens of micrometers, high structural uniformity, and high reproducibility.

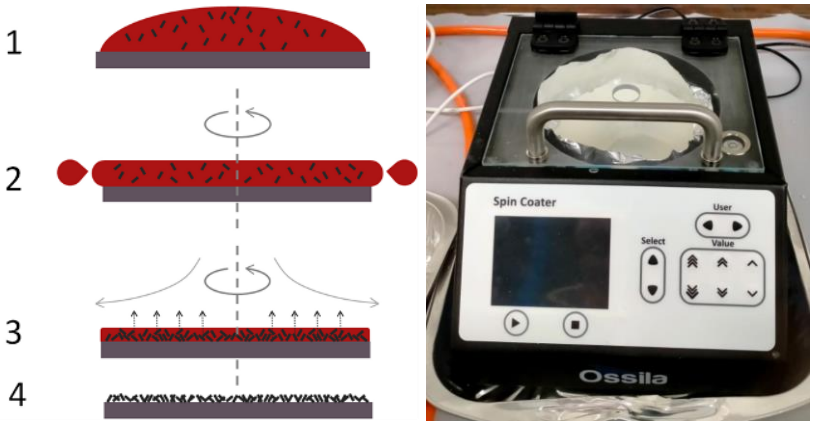

Figure 4.5 – On the left, schematics of the procedural phases during a spin-coating process. On the right, the spin-coater used during this PhD activity. (www.ossila.com)

Spin-coating deposition technique [105, 106] was initially developed for pitch and paint and is now regarded as the main technique for thin films deposition, especially for polymer solutions.

Such technique consists of spreading a liquid phase on a rotating surface, exploiting the centrifugal forces, the viscosity of the liquid, generally a solution, and the evaporation of the solvent, to create layers with thicknesses in the micro/nano-meter range. As shown in the left panel of Figure 4.5, the technique may be described by four procedural phases:

1. *Deposition*: a small drop of solution is dropped onto the substrate, initially still, and starts spreading on the surface. Usually, the solution is dispensed by micro syringes in the form of "bolus" but can also be applied in the form of "heavy rain" or continuous flows.
2. *Spin-up*: here the spinner rotor is activated, and gradually accelerates up to the required speed. In this phase the liquid phase starts to become a layer and to thin, and most of the liquid is ejected from the edges of the substrate as consequence of the gradually growing centrifugal forces.
3. *Spin-off*: the required speed has been reached, and the fluid starts thinning. Here, thinning is ruled by fluidodynamic (or viscous) forces, compelling the liquid mass to spread over the substrate.
4. *Evaporation*: in this phase further thinning of the deposited film mainly occurs due to the evaporation of the solvent: evaporation rate is mainly dependent on the difference in partial pressures (or, better, chemical potentials) of each solvent species between the liquid phase and its surrounding gas phase. Such Stefan-like flow produces migration of solute at the liquid/gas interface, increasing the solute concentration and generating a low-diffusivity "solid skin".

Despite the disadvantages of being hardly scalable, and extremely "material-squandering", since most of the liquid (up to 95-98%) is ejected from the surface during the fluidodynamic thinning regime, it arose as the most used technique not only because of the low cost, the low deposition times, but mainly because the deposited layer uniformity increases during the thinning of the film and because it allows to control accurately the thickness of the film. In the simplest assumption, the thickness profile during the spinning process accords to [105]:

$$h = \frac{h_0}{\sqrt{1 + \frac{4\rho\omega^2 {h_0}^2 t}{3\eta}}}$$

Eq. (4.1)

Where h_0 is the starting thickness of deposited liquid drop, ρ the fluid density, ω the spinner angular speed, η is the fluid absolute viscosity, t the spinning time. Such technique allows for deposition of fluoropolymer films, with good control on their thickness.

4.1.3 PVDF-coated electrodes preparation

Several PVDF grades with different molecular weights are available from Solvay, as shown in the following Table 4.1.

Typical Molecular Weights of Selected Solef® PVDF Grades

Solef® Grade	Mn*	Mw*	Mpeak*	Mw/Mn
Homopolymers				
1010	153	352	237	2.3
1012	180	396	288	2.2
1013	194	434	292	2.2
1015	238	573	418	2.4
6008	135	255	209	1.9
6010	151	322	241	2.1
6012	179	380	296	2.1
6013	201	444	328	2.2
6020	313	687	574	2.2
Copolymers				
11008	127	268	190	2.1
21216	271	596	452	2.2

* g/mol x 10^3

Table 4.1: Solef Solvay PVDF grades with different molecular weight 103 (Mw), Molecular number (Mn), Mpeak, and Polydispersity index Un = Mw/Mn [103].

To minimize the porosity of deposited polymeric films, the PVDF Solef™ 1015 with the highest polydispersity has been used. The PVDF used for all preparations is Solvay Solef™ 1015 with high molecular weight.

The solutions were all prepared by dissolving Solef™ 1015, in powder form, in dimethyl sulfoxide (DMSO), preheated to 60 °C using a 50 ml flask on a heating plate, in constant stirring. Polymer was added gradually until its total dissolving. The solution was then kept at a temperature of 50 °C and stirred for at least 24 hours to ensure complete dissolvement.

To improve the results of energy collection through the REWoD effect, PVDF films had to:

1) show a relative dielectric constant (ε_r) as high as possible.
2) generate a thin, continuous, and hydrophobic film.

The PVDF/DMSO solution was deposited by spin coating on 8 supports for further investigations: 2 supports consist of soda-lime glass (T3 and T4 in Figure 4.6), 2 of copper laminate (C5 and C6, same figure) and 4 of copper tape applied on soda-lime glass (two of which are shown in Figure 4.7), which occupies half the surface of the glass, for better comparison. The rotational speeds used for depositions are 2000 rpm and 5400 rpm for 60 seconds. A drying phase of 1 h at 60 °C in air has been applied for all the samples. The images are made with a black background and at and tilting angle around 60° from the normal to make the deposited layer more visible, recognizable as a patina of colour tending to white.

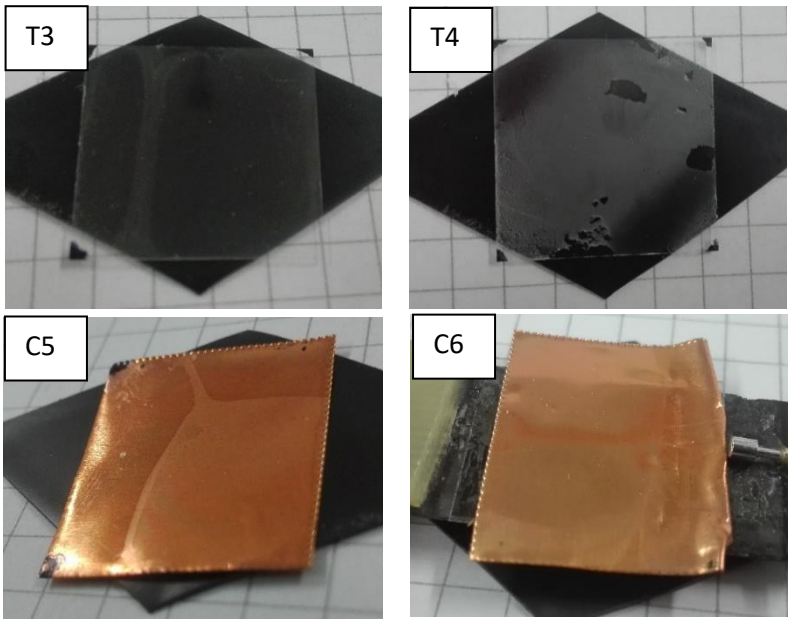

Figure 4.6 – 200 µl of PVDF 10 wt% in DMSO deposited by spin coating on soda-lime glass at 5400 rpm (T3) and 2000 rpm (T4), and on copper foil at 2000 rpm (C5) and 5400 rpm (C6).

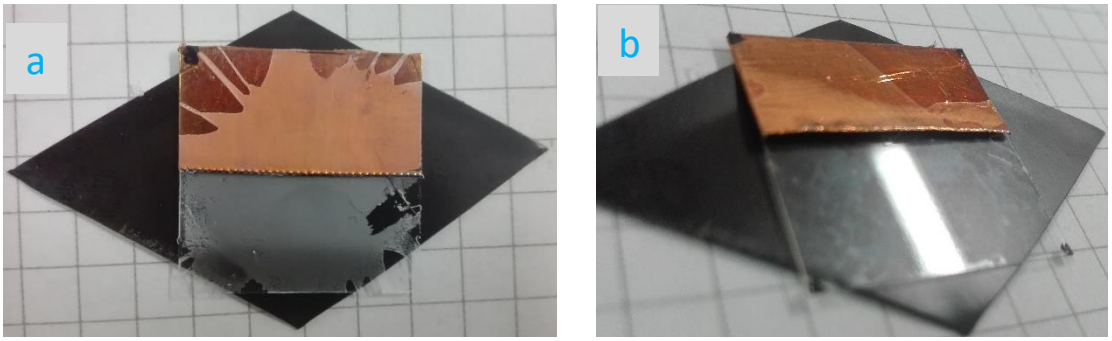

Figure 4.7 – 200 µl of PVDF 10 wt% in DMSO deposited by spin coating on copper tape supported on soda-lime glass at 5400 rpm (a) and 2000 rpm (b).

4.2 Fluoropolymer-coated electrodes characterization

To scope the prepared samples the same techniques described in section 3.2.1, along with those described from here on, were used.

4.2.1 Characterization Techniques

4.2.1.1 Fourier-transform infrared spectroscopy (FTIR)

Fourier transform infrared spectroscopic (FTIR) analysis can simultaneously measure the absorption of a sample across a broad spectrum of infrared (IR) light and the time required is a fraction of that normally required by conventional IR spectrometers. From FTIR studies, it is possible to derive fast and accurate measurements over a wide range with high resolution. By measuring the interference of light intensity, an interferogram is obtained and by applying an inverse Fourier transform to it, the resulting infrared spectrum is graphed as transmittance/absorbance vs. wavelength. Hence the name Fourier transform infrared spectroscopy.
The spectrophotometer used is the "Bruker - IFS66" model with a module for Attenuated Total Reflection (ATR). Figure 4.8 shows the working principle of the ATR.

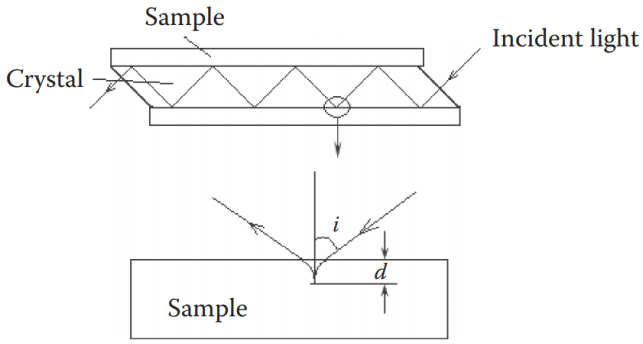

Figure 4.8 – Schematization of the principle of operation of a module for ATR. [107]

The sample is placed on the surface of the ATR crystal. If the refractive index of the crystal is greater than that of the sample, the total reflection of infrared light occurs between the inner surfaces of the crystal when the angle of incidence is at the appropriate distance. During the passage of the standing wave, at each of the reflection points within the crystal, Figure 4.8, some of the energy is absorbed by the sample, so the energy of the reflected light is attenuated, hence the name ATR.

4.2.1.2 Atomic Force Microsocpy (AFM)

The atomic force microscope used is a "Veeco Dimension 3100" AFM, with an acoustic isolation chamber on an anti-vibration table. In measurements with the AFM, the surface is scanned using a nm-sized tip as a probe. The low attractive forces between the material atoms and the tip are detected and controlled to measure the surface contours on an atomic scale. The maximum resolution achievable with this technique is approximately 0.01 nm vertically and 0.1 nm horizontally, although this is highly dependent on the type of tip.

There are three types of AFM measurement modes: contact, noncontact, and tapping.

For soft samples, the contact mode often damages the sample surface causing sample deformation and tip pollution, so the noncontact mode is often used. However, as the distance between the tip and the sample surface is in the order of hundreds of nm, the interaction forces driving the signal are relatively weak and therefore a lower resolution is achieved. To overcome this limitation of the noncontact mode, measurements are often performed in the tapping mode for polymeric materials. For comparison, the surface profile of an example polymeric material obtained with the three modes presented above is shown in Figure 4.9.

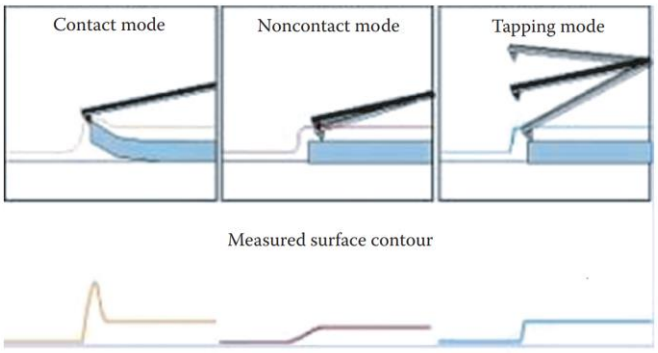

Figure 4.9 – Contours of the surface of a sample surface obtained with the three different scanning modes. [107]

4.2.2 Morphology and Composition

4.2.2.1 PVDF distribution of phases analysis

The ATR FTIR analysis is performed on samples T3, T4 and C5, the former on a glass substrate and the latter on copper foil, respectively, as they present a greater uniformity of the deposited layer. Figure 4.10 shows the relative spectra.

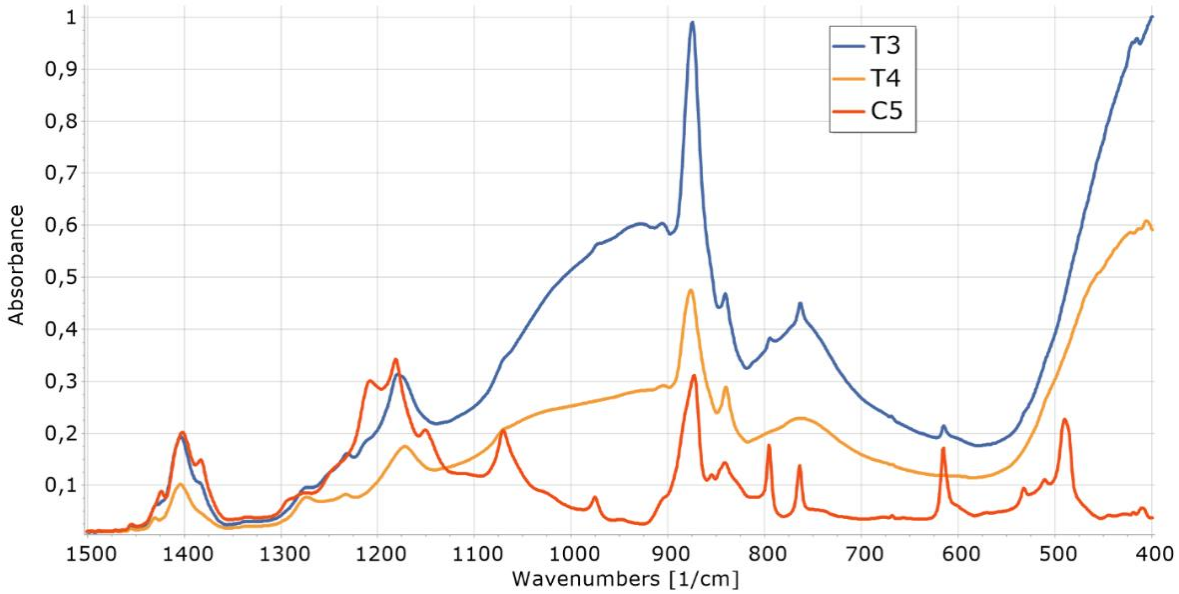

Figure 4.10 – FTIR ATR spectrum of T3-T4-C5 samples

The samples on T3 and T4 glass (orange and blue lines) show spectra with wider and less defined peaks, especially around 900, 760 and 400 cm^{-1}, while the one on C5 copper (red line) has better defined peaks. This could be due to a contribution in the absorption by the glass substrate, given the low thickness of deposited layers. This is confirmed by the evident overlap, shown in Figure 4.11, between the spectra of PVDF on glass, T3 and T4, with the spectrum of the glass substrate alone (light blue line).

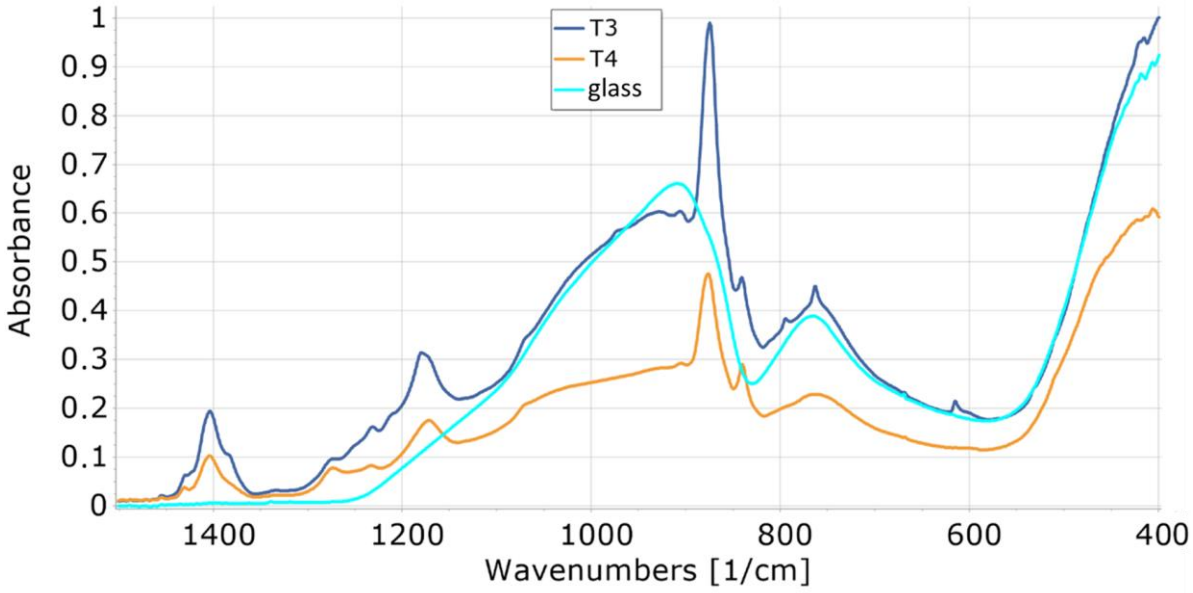

Figure 4.11 – Comparison of ATR FTIR spectrum of T3 and T4 samples with one of soda-lime glass ("vetro", light blue trace).

The consistent absorption observed suggests that the spectra of samples deposited directly on glass may make otherwise easily visible peaks less obvious. The analysis of the spectra, performed by identifying the characteristic peaks of the various α, β and γ phases, was carried out using the methodology proposed by Xiaomei Cai et al. [101]. This research group performed an accurate comparison of the literature, clarified how to identify the various phases in PVDF, and how to quantify them more accurately and reliably.
The typical IR bands are shown in table Table 4.2.

	Wave Number (cm^{-1})	Functional Groups	Type of Vibration
(1)	900	$RR'C=CH_2$	C-H rocking
(2)	909	$RCH=CH_2$	C-CH_2 out of plane bending
(3)	971	(trans) R'CH=CHR	=C-CH bending, R and R' are alkyl groups
(4)	990	$RCH=CH_2$	=C-H out of plane bending, related to (2)
(5)	1068	RCH_2-CHOH-CH_2R'	C-O stretching, corresponding to a secondary alcohol, R and R' are groups with insaturations
(6)	1131	RCH_2-COH(CH_3)-CH_2-	C-O stretching,corresponding to a tertiary alcohol
(7)	1177	-$CH(CH_3)_2$	C-C stretching and C-C-H bending
(8)	1368	-$C(CH_3)_3$	Doblet in C-H bending
(9)	1360	-CO-CH_3	-CH_3 symmetric vibration in a ether
(10)	1375	-CH_3	C-H symmetric bending
(11)	1410	RCH_2-CO-CH_2R	-CH_2- scissoring
(12)	1653	(cis) R'CH=CHR	Terminal bond vibration where R and R' are alkyl chains
(13)	1692	R-CO-OR'	C=C stretching where R and R' are vinyl groups
(14)	1738	R-CO-OR'	C=O stretching where R and R' are alkyl groups

Table 4.2: Spectral FTIR Bands [108].

Three main categories of peaks are identified in the PVDF spectra:

- peaks common to all three phases:
  864-885, 1067-1075, 1171-1182, 1398-1404 cm^{-1}
  are ranges of peaks common to each phase and to mixed systems
- peaks characteristic of a single phase:
  α: 410, 489, 532, 614, 763, 795, 854, 975, 1149, 1209, 1383 and 1423 cm^{-1}
  β: 445, 473 and 1275 cm^{-1}
  γ: 431, 482, 811 and 1234 cm^{-1}
- double peaks that may belong to two different phases:
  837-841 and 508-512 cm^{-1} are typical of the electro active beta-gamma phase.

From this list it is possible to argue the importance of establishing a universal method for tracking the presence of phases. Peaks around 763 and/or 614, 1275 and 1234 cm^{-1} can be consistently used to differentiate and identify α, β and γ phases respectively. The identification procedure can be summarized in the diagram in Figure 4.12.

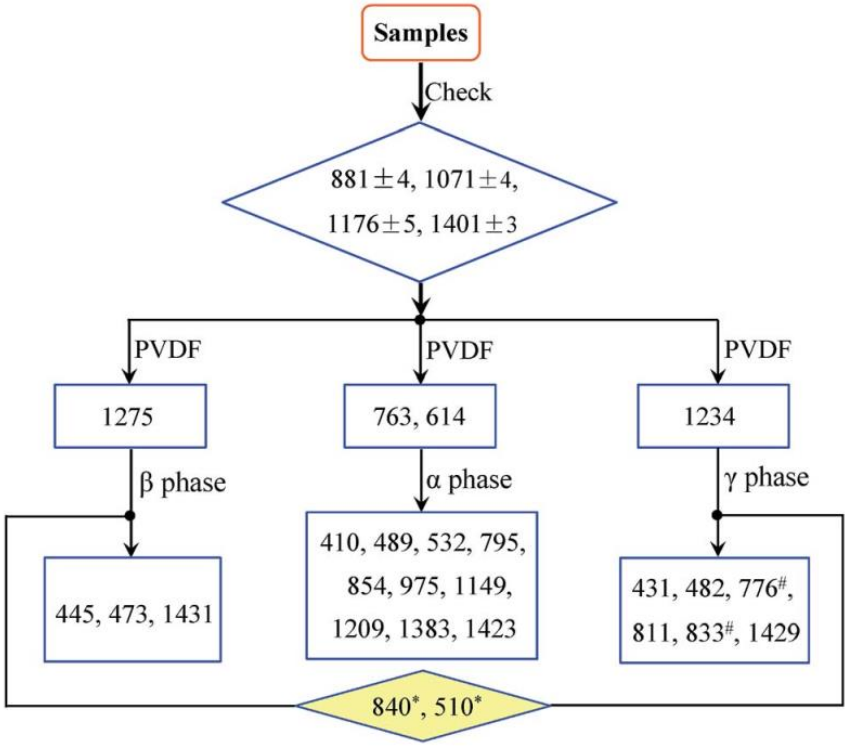

Figure 4.12 – Flowchart for the identification of α, β and γ phases [101].

Applying this procedure to the spectra of Figure 4.10 reveals a greater amount of the β and γ phases (peaks 1275 and 1234 cm^{-1}) in sample T3 (high velocity), and a lower presence of the α phase (peaks 763 and 614 cm^{-1}) in sample T4 (low velocity). For sample C5, a higher amount of the α phase is estimated, as shown in Figure 4.13 and Figure 4.14, where the regions of interest of the spectra of these samples are detailed.

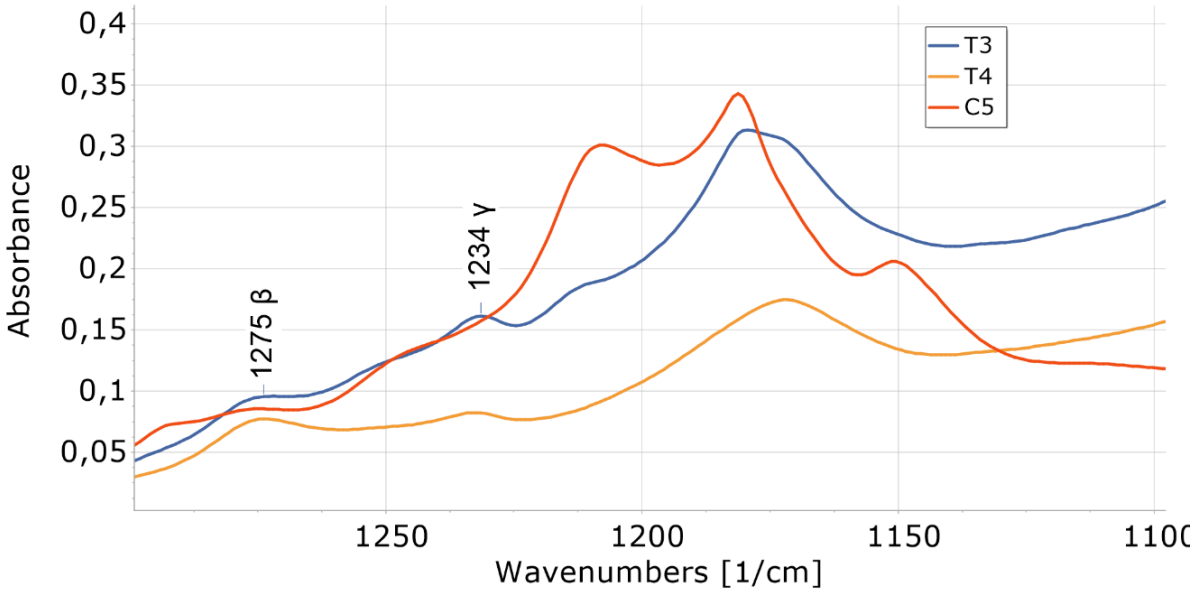

Figure 4.13 – High resolution detail of the ATR FTIR spectrum of Figure 4.10, in the region from 1300 to 1100 cm^{-1}.

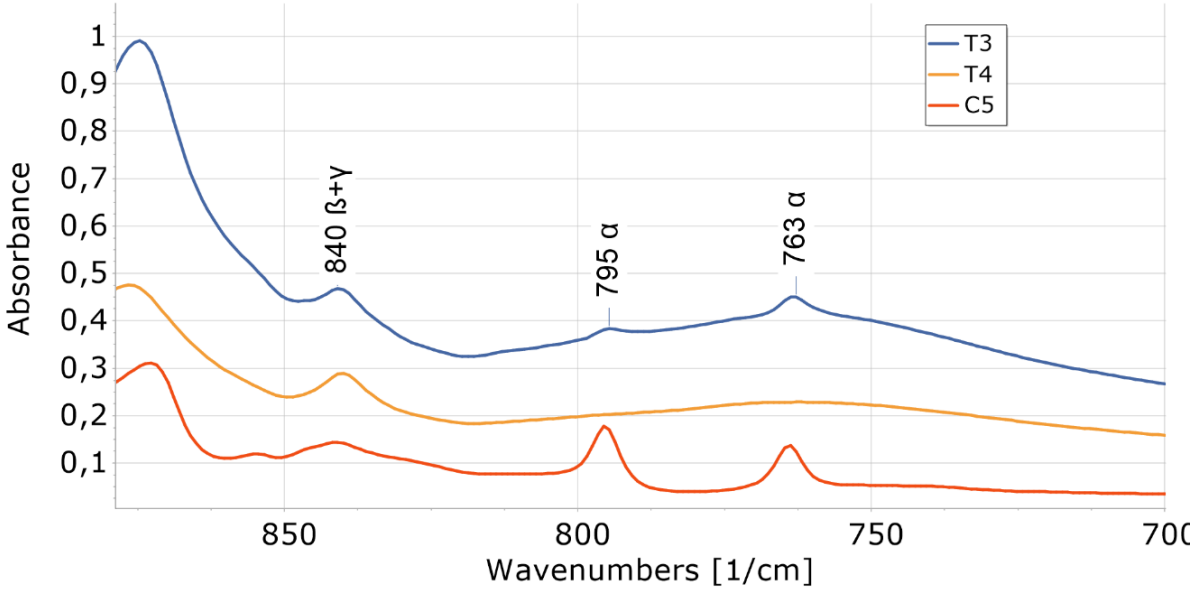

Figure 4.14 – High resolution detail of the ATR FTIR spectrum of Figure 4.10, in the region from 875 to 700 cm^{-1}.

Sample T3 shows a higher crystallinity, identified by the higher absorption peaks [109], showing a greater amount of the crystalline phases than T4. Its higher crystallinity is probably due to a higher evaporation rate of the solvent which, despite the same post-deposition thermal cycle, was caused by the lower thickness of the PVDF layer, a consequence of the higher spin-coating rate and in the case of sample C5 by the excellent thermal conductivity of copper compared to glass. A further fact in favour of this thesis is a more pronounced presence of α phase; indeed, at higher temperatures the greater mobility of polymer chains, inhibits the formation of β phase [110].

The methodology of Cai et al. [101] was used to obtain a more accurate comparison among samples, first quantifying the percentage of electrically active β+γ phase and then deriving from this the percentages of the individual phases.

In fact, since the 840 cm^{-1} band can be assigned either to the β phase, γ phase or both, the relative electro-active fraction of β and γ ($F_{ea,}$), formed by PVDF with α+β, β+γ, α+γ or α+β+γ phases, can be calculated through the following formula:

$$F_{ea} = \frac{I_{ea}}{\left(\frac{K_{840}}{K_{763}}\right) I_{763} + I_{ea}}$$

Eq. (4.2)

where I_{EA} and I_{763} are the absorptions at 840* and 763 cm^{-1}; K_{840*} and K_{763} are the absorption coefficients of the respective absorptions (7.7 10^4 and 6.1 10^4 cm^2 mol^{-1}, respectively) [111]. From such result it was possible to determine the relative amount of the β+γ phase as listed in Table 4.3.

	T3	T4	C5
wt.% β+γ in crystalline phase	45	50	45

Table 4.3 – Calculated percentage weight of the active electrical phase in samples T3, T4 and C5.

The quantification for the single β and γ phases can be calculated by looking at their respective absorption peaks. The most accurate method, according to Cai et al. [101], after several trials was identified in the peak-to-valley height ratio (P2VHR) for the 1275 and 1234 cm^{-1} peaks and applied in the formulas:

$$F(\beta) = F_{ea} * \left(\frac{\Delta H_{\beta'}}{\Delta H_{\beta'} + \Delta H_{\gamma'}}\right)$$

Eq. (4.3)

$$F(\gamma) = F_{ea} * \left(\frac{\Delta H_{\gamma'}}{\Delta H_{\beta'} + \Delta H_{\gamma'}}\right)$$

Eq. (4.4)

Where $\Delta H_{\beta'}$ and $\Delta H_{\gamma'}$ are the height differences between the peak at 1275 cm^{-1} and its closest valley at 1260 cm^{-1} and the peak at 1234 cm^{-1} and its closest valley at 1225 cm^{-1}. Negative P2VHR values were found for sample T3, this is probably due to the presence of glass absorption in the spectrum. To extract the data required for the calculation of the β phase, it was decided to subtract the data from this latter phase using the software "SpectraGryph version 1.2" [112]. This was considered a valid method since the analysis of the spectrum of the glass, without deposition, showed a peak at 950 cm^{-1} which affects the zone surveyed (1280-1220), with the left side of the peak approximating to an increasing straight line. The spectrum of sample T3, the subtracted baseline and the result of the subtraction are shown in Figure 4.15 and are indicated in red, blue, and green, respectively.

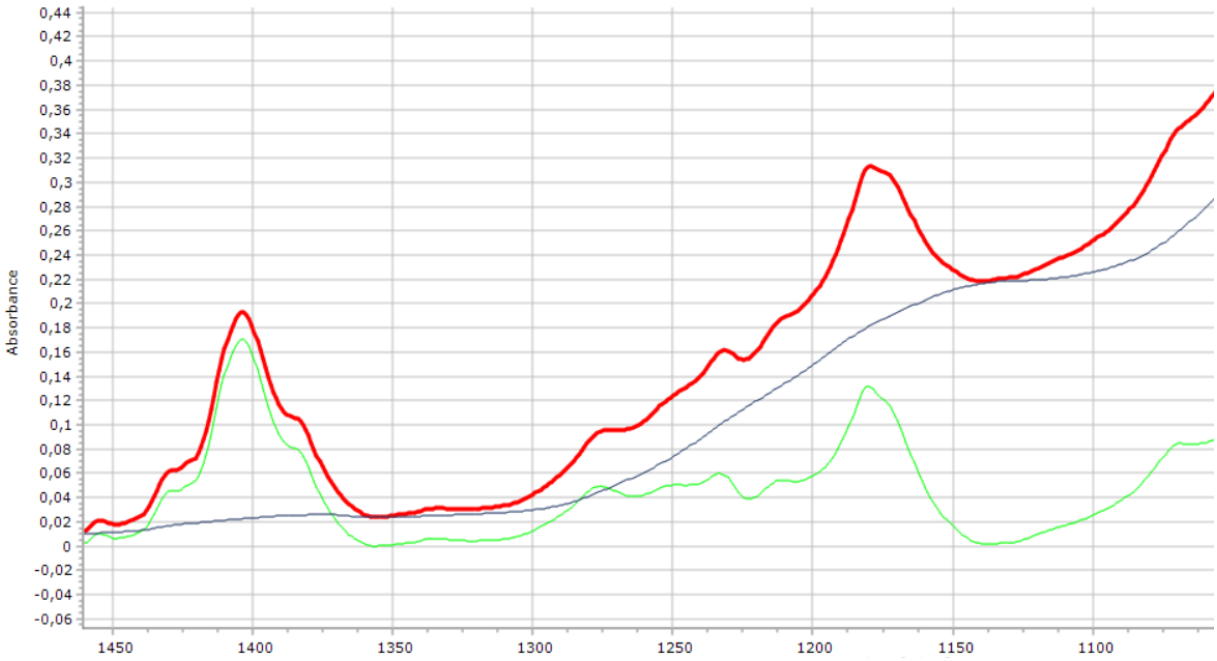

Figure 4.15 – ATR FTIR spectrum of the T3 sample (red), the subtracted baseline (blue) and the resulting spectrum (green).

As a further validation, this same method was applied to sample T4, which is less affected by the presence of glass absorption, obtaining approximately the same result, with a difference of a few percentage points, obtaining then the values enlisted in Table 4.4:

	Deposition (rpm)	Fase β+γ wt%	Fase α wt%	Fase β wt%	Fase γ wt%
T3	5400	45	55	12	33
T4	2000	50	50	30	20
C5	2000	45	55	9	36

Table 4.4: Calculation of the percentage weight presence of PVDF phases in the samples T3, T4, C5.

Those values show a higher relative amount of electro-active β and γ phase in T4, compared to the other samples, which show instead a more pronounced α phase, especially in the case of sample C5. Studies on PVDF have shown that at low concentrations (<20 wt% PVDF), the mechanical stress effect generated during deposition is not relevant for the β phase formation. Other factors have greater effects, such as the film evaporation rate [113], the thickness and the presence of nucleating agents [102, 114]. In conclusion, the fraction of the β phase equals 30, 12, and 9 wt%, for samples T4, T3, and C5 respectively: on this basis, sample T4 is expected to be the most efficient for VEH measurements, due to its higher dielectric properties.

4.2.2.2 *Morphological Analysis*

Since a higher rotational speed during deposition corresponds to a thinner polymer layer, a morphological analysis of the samples was performed, to determine whether an increase in rotational speed could induce a faster evaporation of the solvent and, thus, could affect the crystallization rate. For an evaluation of this, AFM images of samples C5 and C6, both deposited on copper foil at rotational speeds of 2000 and 5400 rpm respectively, were acquired, and shown in Figure 4.16.

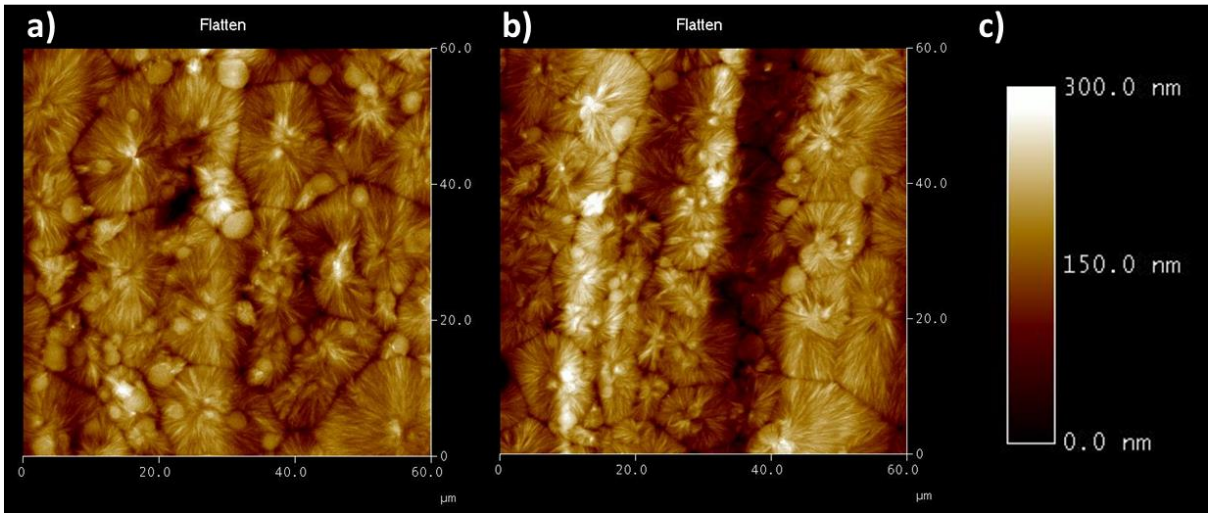

Figure 4.16 – AFM image of (a) C5 sample (2000 rpm) and (b) C6 sample (5400 rpm). In c) the chromatic scale for the height is shown. Average spherulite size is 12.5 µm for (a) and 9.2 µm for (b).

An average diameter of 12.5 µm for spherulites was found for sample C5, while for sample C6 the average diameter is reduced to 9.2 µm. This is a clear indication of a faster primary nucleation phase than C5 and thus a faster crystallisation.

4.2.2.3 *Contact angle measurements*

For each sample analysed, WCAs were acquired at different positions on the surface, applying the same methodology described in 3.2.2.1. Furthermore, to better evaluate the spatial uniformity of the samples, the points were generally taken along the diagonals of the square samples, as shown in Figure 4.17a, except for the samples with copper tape on glass. For the latter type of samples, indeed, four points were chosen, distributed 2 on the copper side and another 2 on the glass, in symmetrical positions with respect to the separation line of the substrates (Figure 4.17b).

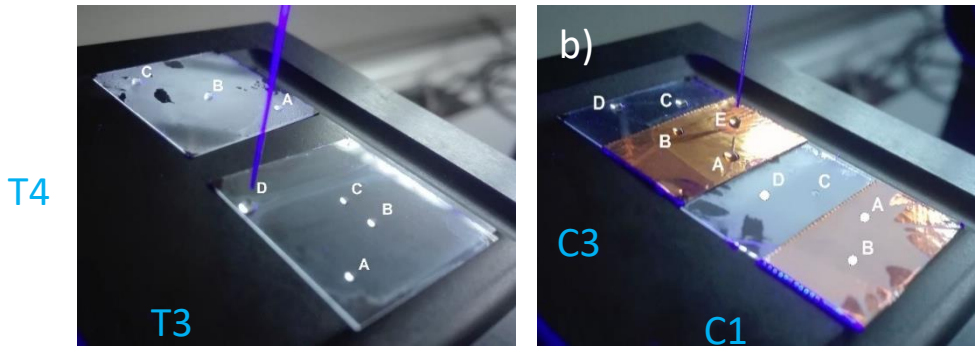

Figure 4.17 – Examples of the positions of the measuring points to evaluate the uniformity of the samples: (a) sample at the top shows the position of the points on the diagonal, the sample at the bottom shows, in addition to the points taken on the diagonal direction, the addition of the point of interest D, in a non-homogeneous area. (b) position of the measuring points of the copper glass samples, in the upper one, point B is an additional point of interest on a non-homogeneous area.

Table 4.5 shows the averaged starting and final WCA values of the samples. Sample T1 showed WCA values across the hydrophilic/hydrophobic transition, the more the distance from the center, the lower WCA. For sample T2 only the central part of the spin-coated layer showed hydrophobic properties, whereas the measurements made in outer parts of the deposition obtained WCA values next to those of the glass (also reported on Table 4.5 as reference), indicating non-homogeneity of the film in those regions. For this sample only the measurement in the central part of the film was reported. For sample T3, C2, C3, C4, and C5 WCA values of about 80° were measured, coherent with those reported from the producers [103]. Sample T4 and C1 showed hydrophobic properties and, most of all, good homogeneity of the deposited films. On optical inspection, these samples show a more homogeneous and better distributed film on the substrate. Concerning the influence of the various phases on the hydrophobicity, a greater presence of crystalline phase, specifically β-phase, seems to lead to an increase of the contact angle. In general, the contact angle seems to increase as the intensity of the peaks increases, especially those corresponding to the β phase. However, this seems to contradict some studies that seem to cite the hydrophilic tendency of the β-phase of PVDF as a known fact [115]. Further, from such analysis a consistent decrease, of about fifteen degrees, between the copper substrate (Figure 4.17b) and the glass substrate (Figure 4.17a): this indicate a non-negligible effect of the substrate on WCA, as evidenced in the last rows of Table 4.5. At the same time though, the films deposited on glass substrate show less homogeneity, perhaps indicating that the PVDF layer is not completely uniform because of the morphology of the substrates.

Sample	Average starting CA (°)	Average final CA (°)
Glass	39.0	30.0
T1	102.0	92.7
T2	103.7	125.0
T3	80.8	77.0
T4	118.7	112.3
C1	124.3	114.3
C2	84.3	80.0
C3	87.4	80.8
C4	84.3	78.0
C5	94.3	74.0
T-type	104.0	101.8
C-type	94.9	85.4

Table 4.5: Lesft - Average starting and final WCAs, for the PVDF thin films, defined as in 3.2.1.

Polymer	Angle of Contact θ (water) [Degrees]	Surface Tension γ_s [mJ/m²]
PTFE	108	19
PCTFE	84	31
PVDF	80	34
HD – PE	88	33
PET	76	47
PA 6.6	72	47

Table 4.6: Right - Table of contact angle from Solvay data sheet [103].

In the literature [115], the factors that mainly influence the WCA, hence the hydrophobic properties, are the morphology of the surface layer and its chemical composition which, in present case, is represented only by the surface variation of the PVDF crystalline phases.
Generally, samples WCAs showed stability during the measurement time (60 sec). However, most of the samples presented a slightly hydrophilic behaviour, in accordance with the tabulated values of the polymer data sheet, shown in Table 4.6, where a WCA value of 80° is reported [103].

4.2.2.4 Dielectric constant estimation

For a theoretical evaluation of the effects of the various phases on the relative dielectric constant of the film, a simple approximate model was used, based on the "volume fraction average", and the relative dielectric constants ε_r of the various phases taken from the literature [116] and shown in Figure 4.18.

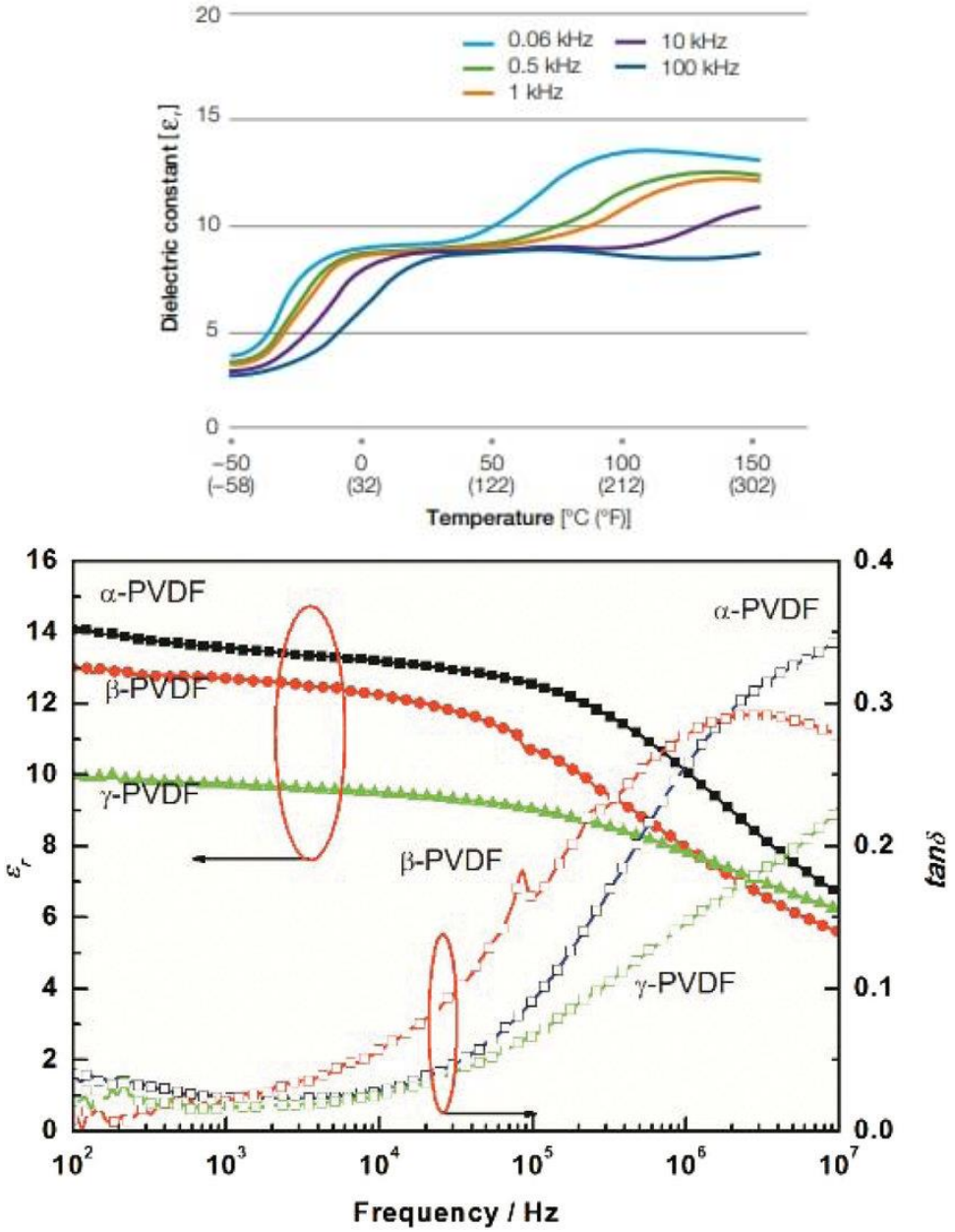

Figure 4.18 – Top) The dielectric constant for amorphous Solef™ PVDF serie 1000 at low frequencies, as a function of temperature [103]. Bottom) Relative dielectric constant and dielectric loss for the crystalline phases of PVDF as a function of the frequency [98].

It is therefore possible to estimate the effective dielectric constant of the polymer layer using the following formula:

$$\varepsilon_{eff} = \sum_n \phi_n \varepsilon_n$$

Eq. (4.5)

where ε_n are the dielectric values of the various polymer phases and φ_n their fractional volume [117]. Not being able to quantify the fraction of the crystalline phase, the case of maximum crystallinity was considered, which for a semi-crystalline polymer is quantified as approximately 60% [103]. This allows a calculation of the optimum conditions we can have for the relative dielectric constant through this model. The following theoretical values were obtained, with the addition of two extreme situations for comparison.

	α wt%	β wt%	γ wt%	Amorphous wt%	ε_{eff}
T3	0,33	0,07	0,20	0,4	10,76
T4	0,30	0,18	0,12	0,4	10,94
C5	0,33	0,05	0,22	0,4	10,68
PVDF 100% amorphous	0	0	0	1,0	8,00
PVDF β Maximal value	0	0,6	0	0,4	11,00

Table 4.7: Estimation of the relative amounts (weight/weight) of the different crystalline phases contribution of the PVDF and effective relative dielectric constant ε_{eff} calculated for various samples.

From the estimates of the relative effective dielectric constant ε_{eff}, shown in Table 4.7, it is possible to conclude that fabricated samples exhibit an increase in the value of ε_{eff} of about 35% with respect to a completely amorphous phase. This value is very close to that which could be obtained if the crystalline phase were entirely β-type, e.g., 40%. Therefore, maximising the presence of well-defined crystalline phases guarantees good dielectric properties to the film.

4.2.2.5 Discussion

In addition, WCAs show considerable improvement as the crystalline phase increases. The values measured in the most promising samples show an increase of about 50% in WCA with respect to that of the amorphous phase reported in Table 4.6. As already reported in section 4.2.2.3, from the analysis of the areas and their peaks it is possible to conclude that:

- The spin-coated PVDF films showed generally an increase of WCAs with respect to bare PVDF, as reported in [103].
- The samples in Figure 4.17 show a non-negligible effect of the substrate morphology on the layer hydrophobic properties; higher WCAs were measured for soda-lime glass surfaces with respect to copper ones.

The control of the crystalline phases of the polymer layer therefore makes it possible to improve the morphological properties and obtain much better WCAs. However, to significantly increase the dielectric constant of the film it is necessary to intervene in other ways, such as the addition of metal oxides of size in the micro/nano-metric range.

4.2.3 PVDF on Aluminium foils

After the preliminary characterizations of PVDF film deposited on glass and copper, the same PVDF/DMSO solution was deposited by spin coating on aluminium foil supports with the purpose to exploit them in a future prototype device, analogous to the prototype reported in 3.3.3.

4.2.3.1 Contact angle measurement on PVDF

WCAs measurements were taken as described in 3.2.2.1. For the different PVDF films on Al foils made, different static WCA measurements were performed at different points of the sample. In the images in Figure 4.19, a resume of WCAs measurements is shown. They vary from 111° to 142°, just below the superhydrophobic regime. The samples with higher WCAs were then selected for characterization of VEH performance.

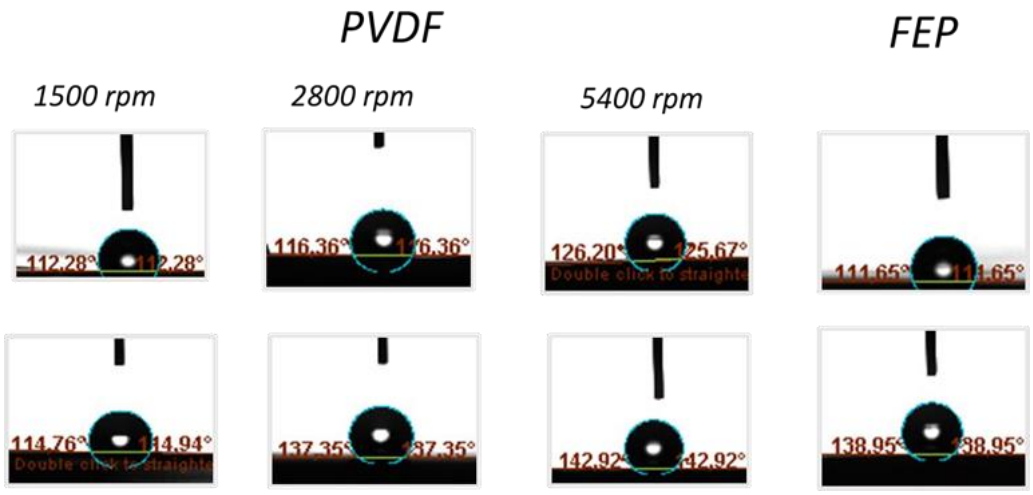

Figure 4.19 – WCA measurements on some representative PVDF samples deposited by spin coating on Al foils The first three columns represent contact angle measurements of some PVDF samples deposited on Al substrates by different spin coating rotation speeds (rpm). For each deposition speed tested the minimum (top line) and maximum values (bottom line) of contact angle obtained on several samples are shown. As a reference the last column shows the measurement of the water contact angle acquired on of the commercial 25 µm FEP sheet provided to us by DuPont.

From the previous investigations of all the dielectric films prepared, the most promising were chosen for uniformity of deposition, thickness, and hydrophobicity of the PVDF film. In the following, the results of the measurements carried out at varying the ionic solution are reported for the PVDF films deposited on aluminium foils, that proved to be the best candidate, made by depositing 30 µL of PVDF in DMSO at 5% concentration by spin coating at 5400 rpm for 60 sec.

4.2.4 PVDF film embedding TiO_2 NPs

Given the purpose of maximizing the relative dielectric constant in PVDF depositions, it was decided to add one of several additives to the polymer solution that are known for their ability to raise the relative dielectric constant ε_r [118]. Extensive research has been carried out to combine the high relative dielectric constants of the various metal oxides with the excellent chemical, physical and processing properties of the polymers. In this specific case, TiO_2 was chosen because of its low cost and toxicity. This additive has a relative dielectric constant ε = 80, namely up to eight times higher than PVDF, which varies in an ε range between 8 and 14, depending on the phases present and the degree of crystallinity, as summarised in the following table.

ε_α	14
ε_β	13
ε_γ	10
ε_{amorfo}	8
ε_{TiO2}	80

Table 4-8: Values of ε from Figure 4.18 [103].

Properly shaped soda lime microscope slides with rectangular regions of copper deposited by thermal evaporation have both characteristics necessary to be able to perform EH (electrical conductivity) measurements and to support better and more consistent characterisations and analyses. In addition to this, it was evaluated to test the use of a solution of PDVF in DMSO at 5 wt%, to have an easier manual processability. This was accomplished by means of preparation of samples C7, C8, C9, namely three samples deposited on glass/copper substrate and reported (except for sample C7, unfortunately lacking) in Figure 4.20. For these substrates, a 5% PVDF solution in DMSO with different weight concentrations of TiO_2 was deposited by spin coating [119].

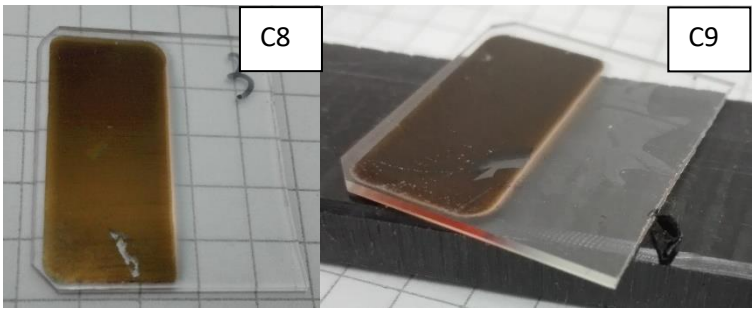

Figure 4.20 – PVDF (5 wt%) deposited by spin-coating at 2000 rpm with 0.01 wt% (C8) and 0.005 wt% (C9) of TiO_2

All samples were made using the same deposition parameters (2000 rpm) but with TiO_2 weight percentages of 0%, 0.01%, and 0.005% for samples C7, C8, and C9, respectively. The use for such low concentrations was chosen because of two reasons. The first is because it is reported in the literature that under the percentage of 0.45% the phenomenon of aggregation of TiO_2 particles is negligible, if not completely absent [120]. The second is to fall within the infinite dilution condition that allows us to use Maxwell's equation for the theoretical evaluation of the dielectric value [117].

The samples were then subjected to optical microscopy, FE-SEM and ATR FTIR analysis to get a more precise idea of the effects of TiO_2 on the other characteristics of the films.

4.2.4.1 Film thickness estimation

The viscosity of the concentrated polymer solution at 5 wt% is $\eta_{10\%}$ = 0.24 P. From the literature on rheological characterisation, considering the high rotational speed of the spin-coater (2000-5400 rpm), the relative short deposition of tens of seconds and the low volatility of DMSO at room temperature, it is possible to assume negligible solvent evaporation, and the viscosity of the solution is approximately constant during deposition. Thus, the thickness of the deposited layer can be estimated in a first approximation with Eq. (4.1) previously described and is given below for convenience:

$$h = \frac{h_0}{\sqrt{1 + \frac{4\rho\omega^2 {h_0}^2 t}{3\eta}}}$$

The h_0 value depends on the wettability of the substrate, the viscosity of the solution and the initial angular acceleration of the plate, which causes a torque force on the polymer. Based on previous studies [113] it was estimated that for PVDF 5 wt% the h_0 value can vary in a range from 8 to 20 µm. However, one must add the contribution due to TiO_2 to the density of the solution, which is calculated using the following expression:

$$\rho = M_{\text{solution}}\, V_{\text{solution}} \qquad \text{Eq. (4.6)}$$

where $M_{\text{solution}} = m_{\text{PVDF}} + m_{\text{DMSO}} + m_{\text{TiO2}}$ is the sum of the measured masses of PVDF, DMSO and TiO_2 respectively, and $V_{\text{solution}} = m_{\text{PVDF}}/\rho_{\text{PVDF}} + m_{\text{DMSO}}/\rho_{\text{DMSO}} + m_{\text{TiO2}}/\rho_{\text{TiO2}}$, considering the density of PVDF ρ_{PVDF} = 1.78 g/cm^3, that of DMSO ρ_{DMSO} = 1.1 g/cm^3 and of ρ_{TiO2} = 4.23 g/cm^3.

From the calculated density ρ_{solution} = 1.120 g/cm^3 and the Eq. (4.6) it is possible to estimate the thickness of the deposited layer, as reported in Table 4-9:

	h_0 min = 8 µm	h_0 max = 20 µm
Estimated thickness for PVDF 5%	Thickness [µm]	Thickness [µm]
2000 rpm	1,1	1,7

Table 4-9: Estimated thickness values of the deposited films of the C7-C8-C9 samples.

4.2.4.2 ATR FTIR Analysis

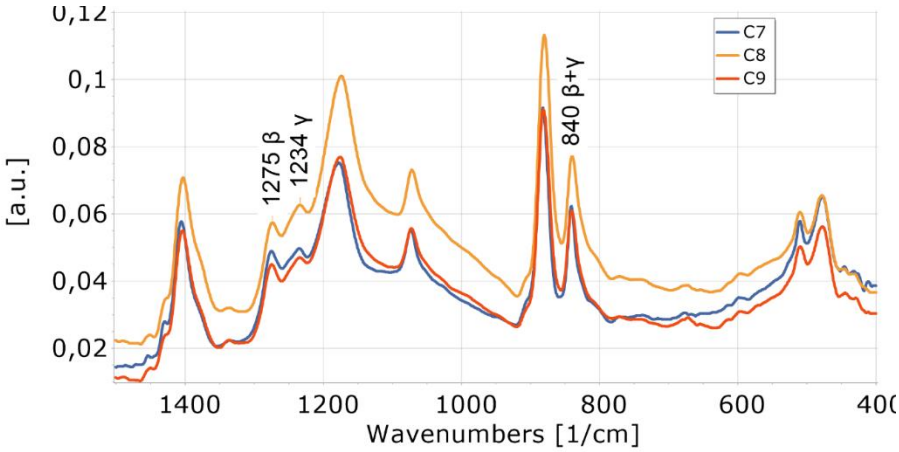

Figure 4.21 – FTIR ATR spectra of C7-C8-C9 samples

The measured ATR FTIR spectra, Figure 4.21, show, compared to the previous samples, lower absorption values but better-defined peaks. This is due to the use of a lower concentration PVDF solution (PVDF 5% in DMSO) and to the new deposited copper substrate, which unlike glass substrates does not contribute to the measured spectrum. Continuing to use the previously used methodology, summarised in Figure 4.22 with the ε values for the various PVDF phases as reported in Table 4-8, the relative amount of the different crystalline phases can be calculated as reported in Table 4.10.

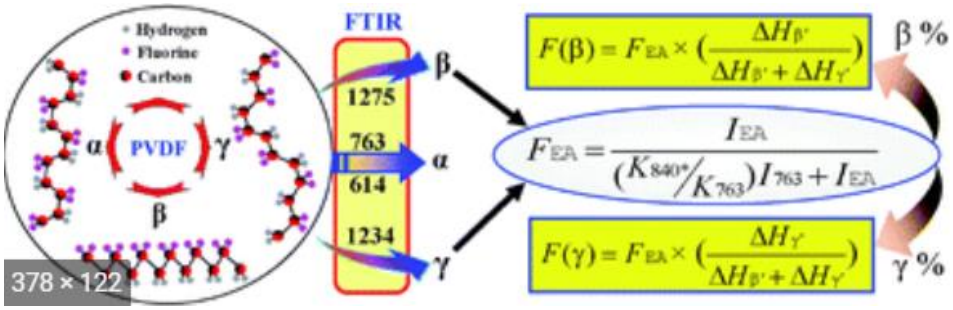

Figure 4.22 – Schematization of calculations to derive wt% of the various phases [101].

The addition of TiO_2 to the PVDF solution already seems to have visible effects at these low concentrations. However, as it was not possible to survey samples with a larger amount of TiO_2, this remains an assumption. The additive may be the cause of the increase in the percentage of the crystalline phase since, by lowering the activation energy in the nucleation phase, it allows TiO_2 to become the centre of the PVDF spherulite, causing the phenomenon of heterogeneous nucleation. It was therefore hypothesized that the increase in α phase, to a modest extent, accompanied by obvious changes in morphology, is in fact due not directly to the addition of TiO_2 [120] but to its ability to modify the crystallization rate.

Sample ID	TiO_2 wt%	α wt%	β+γ wt%	β wt%	γ wt%
C7	0	37	63	44	19
C9	0,005	37	63	49	14
C8	0,01	40	60	40	20

Table 4.10: Calculation of the percentage weight presence of PVDF phases in C7 C8 C9 samples

4.2.4.3 Morphological Analysis

FE-SEM images of C7, C8 and C9 samples were acquired using a Zeiss "Crossbeam FIB-SEM" electron microscope with both a standard secondary electron analyser (SE*II*) and an In-Lens analyser, described in 3.2.1.2. These images show the morphology of the deposited PVDF.

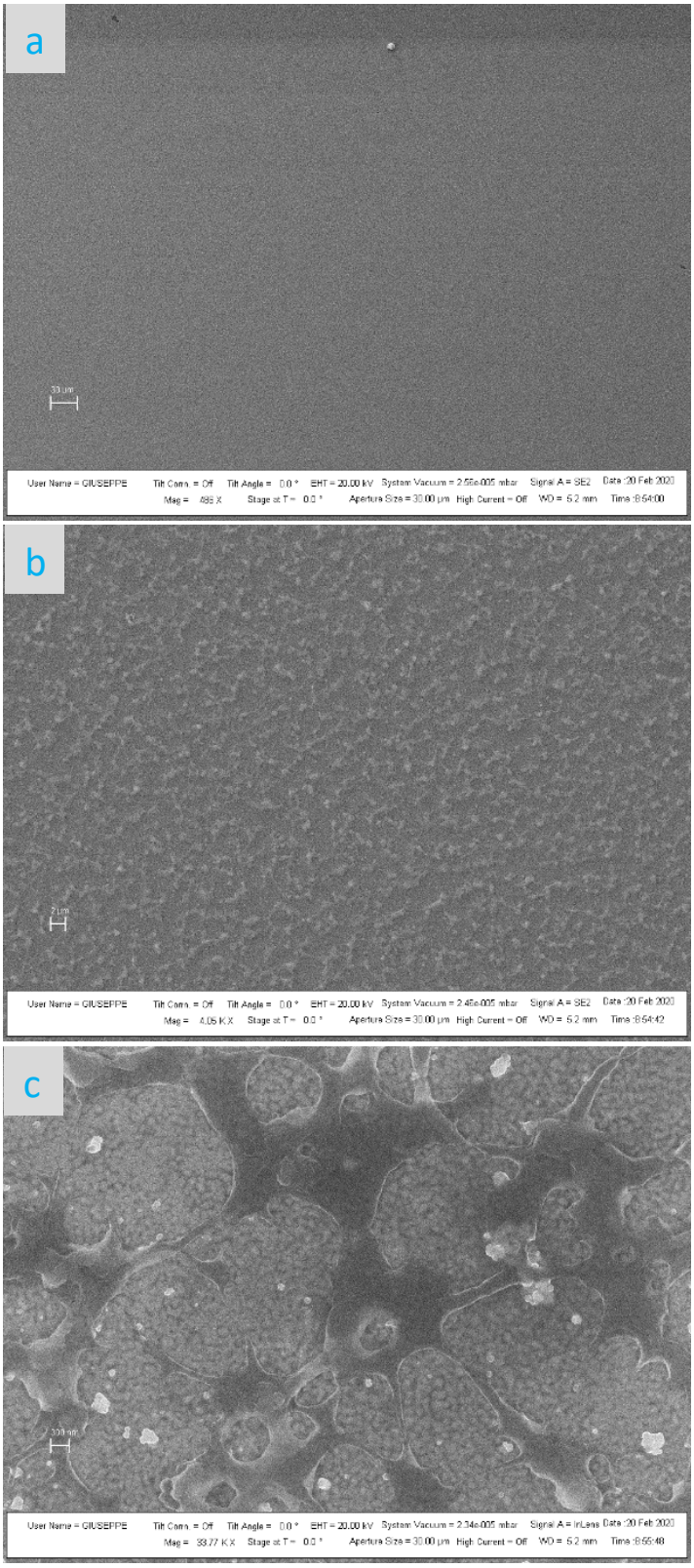

Figure 4.23 – FE-SEM images of sample C7, recorded by SEII anaylser (a, b) and by In-Lens analyzer (c). Scale bar is 33um (a), 2um (b), 300 nm (c).

At the maximum magnification of the optical microscope (500X), no polymeric spherulites can be observed in sample C7 and no differences can be seen in the film deposited on glass compared to that deposited on copper, an indication that this substrate does not significantly influence the deposition of PVDF, also because the deposited copper has a very low surface roughness, comparable to that of the glass supporting it, estimated by AFM at around 10nm. Continuing the analysis at higher magnifications by means of the FE-SEM electron microscope, from the images in it is possible to recognise the same pattern observed with the optical microscope, showing a certain regularity of dispersion of PVDF agglomerates on the metallic substrate. From the analysis with the In-Lens detector, these agglomerates seem to be formed by PVDF between 1 and 6 µm in size with a filamentous shape and an almost spherical central body and connected to other neighbours by small filaments, a few hundred nanometres thick (Figure 4.24 c). The dark parts are the PVDF, and the light grey spherical "dots" are the copper substrate.

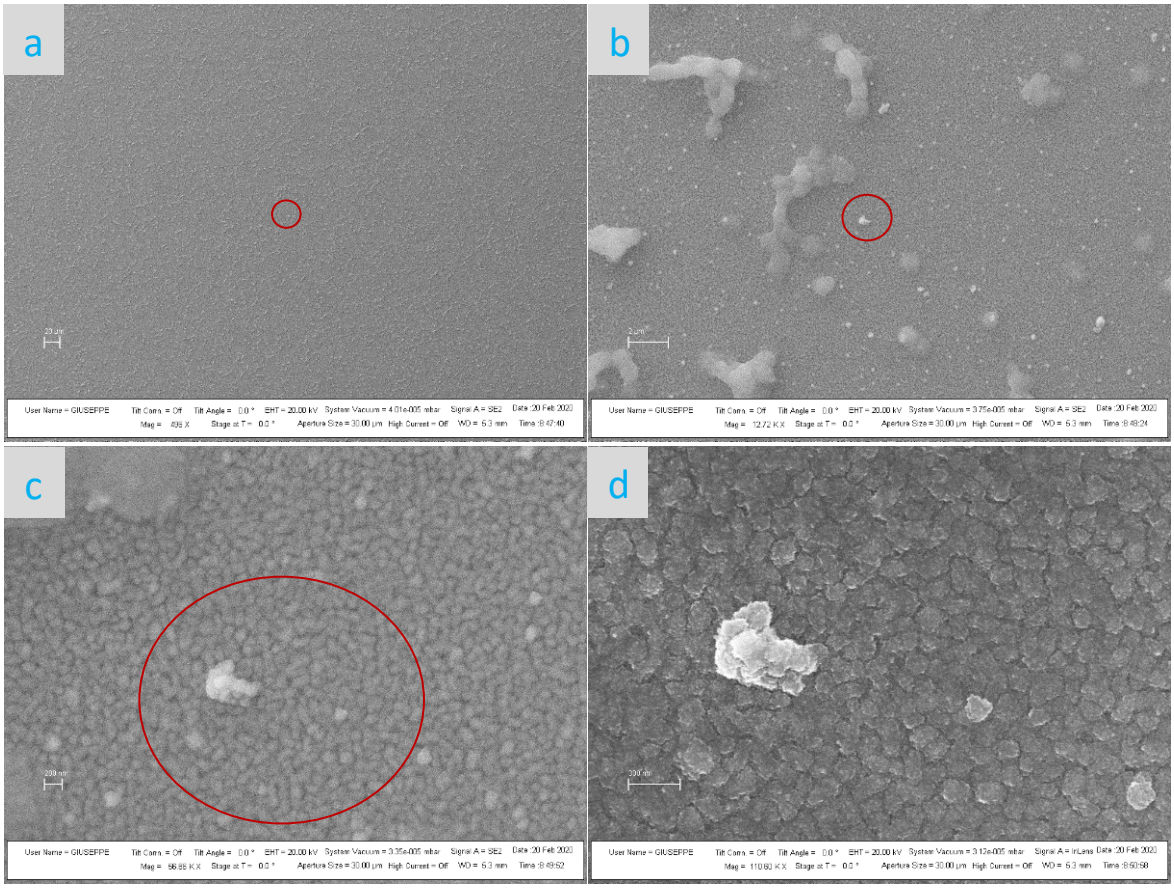

Figure 4.24 – FE-SEM images of the sample C9 in SEII (a-b-c) and in In-Lens (d) mode. The regions circles in red correspond to subsequent images of increasing magnification. C and D show an enlargement of Cu particles with a TiO2 particle (white).

Also, in the C9 sample there is a non-uniform PVDF layer but jagged with areas covered by the polymer with a pattern of microscopic white grains that seem to be ascribable to not well dissolved TiO_2 lumps, highlighted with red circles. There are no visible polymeric spherulites.

Such features are confirmed by the analysis at higher magnifications: indeed, FE-SEM images (Figure 4.24) and the optical microscope images show the same pattern. Agglomerates of PVDF particles a few µm in size are clearly visible in Figure 4.24 b. From the subsequent images at higher magnification, it is still possible to notice light grey spherical "dots" of the copper substrate, as well as sporadic white dots representing TiO_2.

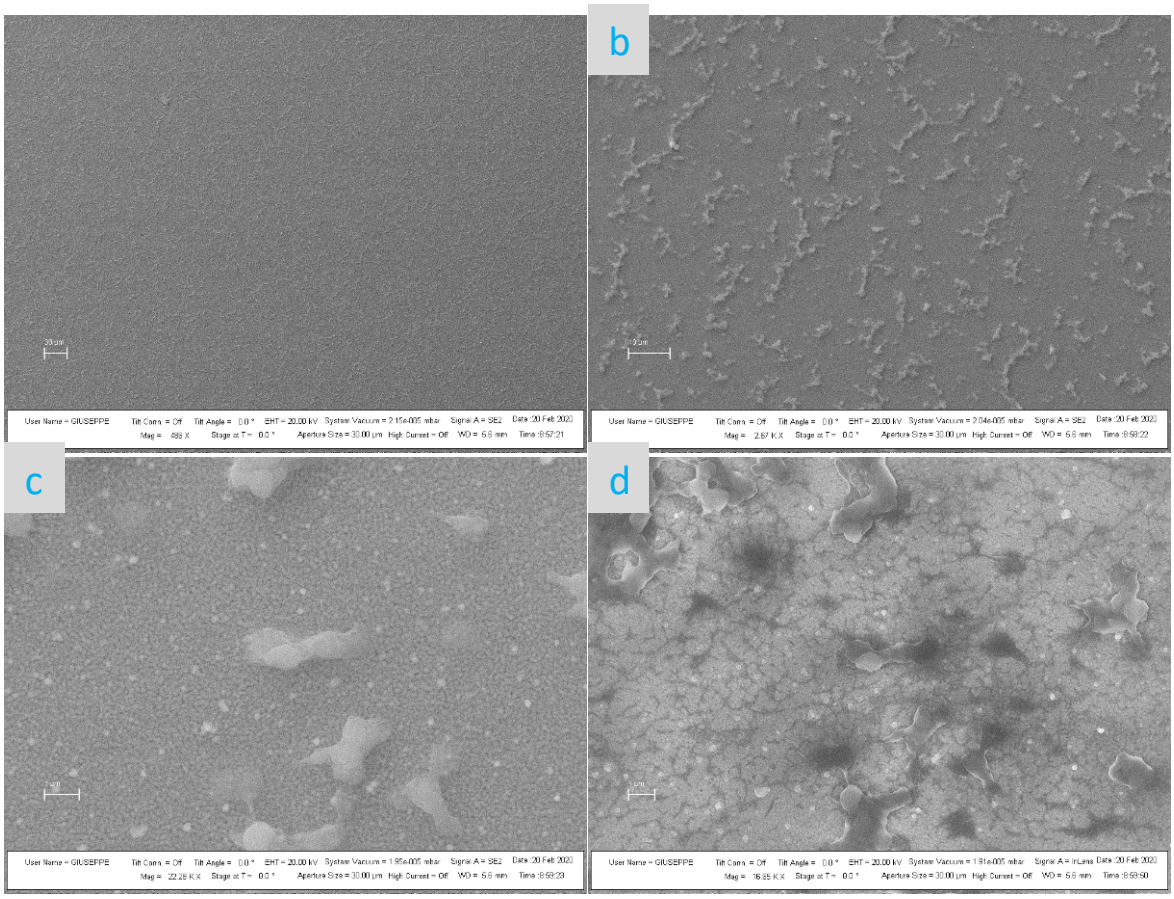

Figure 4.25 – FE-SEM images of C8 sample (PVDF with TiO_2) at different magnifications with SE2 (a) (b) (c) and with In-Lens (d).

In sample C8 (Figure 2.4) a non-uniform layer of PVDF can be seen, but it is indented by areas covered by the polymer with a pattern present and more numerous than in C9, microscopic white grains that can be traced back to TiO_2 lumps. There are no visible polymeric spherulites.
Continuing the analysis at higher magnifications, the FE-SEM microscope images, Figure 4.28, still show the same pattern of dispersed PVDF agglomerated in particles a few microns in size. Always present, the light grey spherical "dots" of the copper substrate. A greater presence of TiO_2 not dissolved in the polymer is shown, which is however quite uniformly distributed (white dots).

4.2.4.4 *Water Contact Angle Measurements*

For samples C7-C9 it was chosen to take the measurement points along the median parallel to the longest sides of the copper deposition, as shown in Figure 4.26.

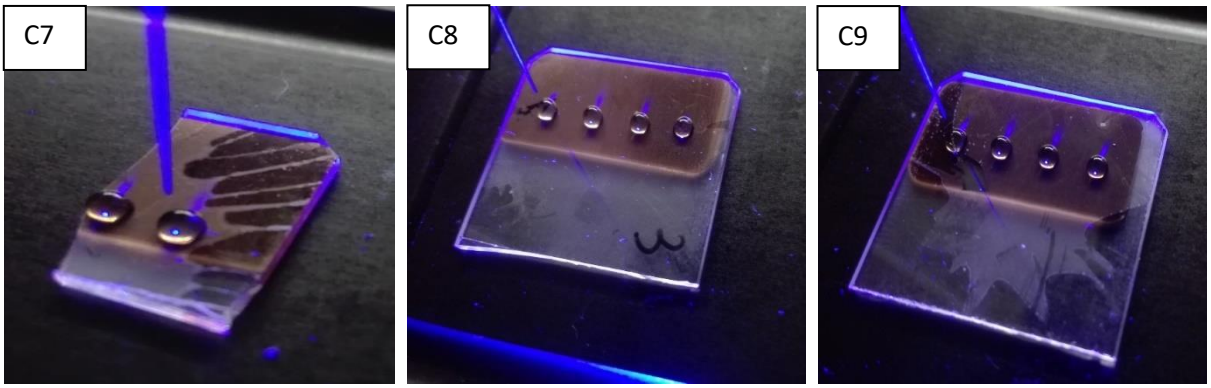

Figure 4.26 – Position of WCA measuring points in samples C7, C8 and C9.

This since the main purpose is to determine the hydrophobicity properties of deposited above the copper layer, moreover, as already seen also in WCA measurements for samples C1-C5, Figure 4.15, it seems that the substrate affects the contact angle measurements. The contact angle measurements on the C7 sample were only two due to failure of the substrate during the ATR FTIR measurements (the ATR module requires you to exert some pressure on the sample being measured).

Sample	Average starting WCA (°)	Starting WCA St. Dev. (°)	Average final WCA (°)	Final WCA St. Dev. (°)
C7	114.5	3.54	103.5	4,95
C8	98	8.04	94	11.52
C9	102.8	3.59	100.5	4.04

Table 4.11: Starting and final Average WCAs for samples C7, C8 and C9, along with the respective standard deviations.

4.2.4.5 *Dielectric constant evaluation*

For a theoretical evaluation of the effects of TiO_2 on the dielectric constant, a simple although not so accurate model has been used, the so-called "volume fraction average" equation:

$$\varepsilon_{eff} = \phi_1 \varepsilon_1 + \phi_2 \varepsilon_2$$

Eq. (4.7)

Again, since it was not possible to make measurements of the amount of crystalline versus amorphous phase, the situation of maximum crystallinity (a semi-crystalline being quantified as approximately 60%) was considered in estimating the dielectric constant:

	0,01 Wt% TiO_2	0,005 Wt% TiO_2
VFA model	12,68	12,34

Table 4.12: Calculation of the dielectric constant of the layers deposited for samples C7, C8, C9, assuming a VFA Model.

4.2.4.6 Discussion

The morphological images show non-homogeneous films under the experimental conditions used. This is probably due to the high-humidity environmental conditions to which the polymer was subjected prior to the passage through the oven. Indeed, it is reported in the literature that the temperature and especially the humidity conditions are an essential factor in the formation of continuous and low roughness films. The surface morphology is determined by the phase separation that occurs in the ternary solution polymer-solvent-water(air) during the evaporation of the polymer. In fact, the water present in the air humidity is miscible with DMSO and penetrates the films by diffusion. Since the evaporation of DMSO is slower than that of water [121] and since the latter is a non-solvent for PVDF, phase separation occurs. In the absence of water, however, phase separation does not occur, and the film is dense and homogeneous. For comparison, FE-SEM images (Figure 4.32) of substrates made by depositing PVDF at various temperature and humidity conditions are shown from the literature [122].

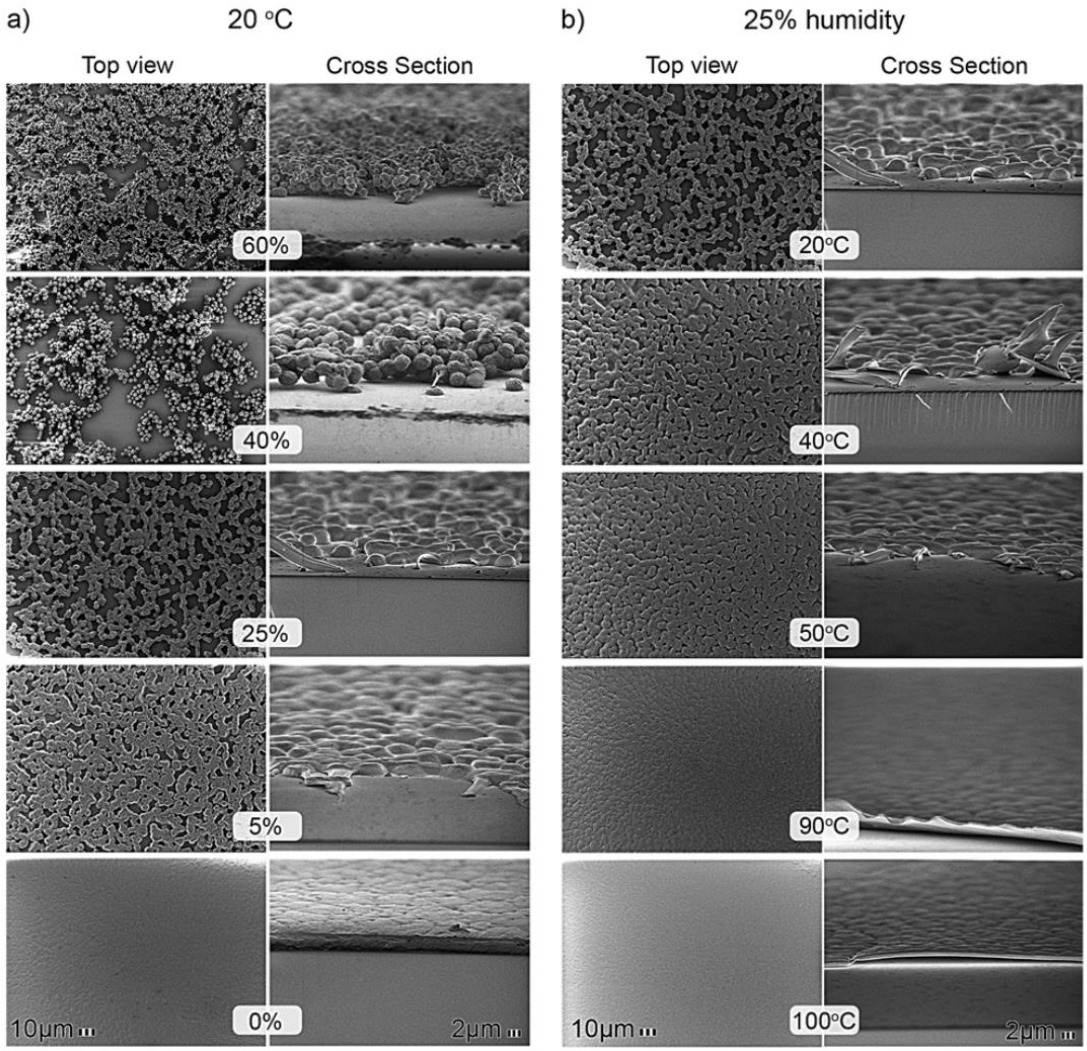

Figure 4.27 – Morphology of the evolution of PVDF thin film surface (a) Top view and cross-section of SEM micrographs of PVDF films presented as a function of relative humidity between 0% and 60%. The films have been deposited at room temperatures. (b) Top and cross-section view of SEM micrographs of PVDF thin films presented as a function of deposition temperatures between 20 °C and 100 °C. The relative humidity has been set at 25%. [122].

It is possible to estimate that the humidity in the laboratory where the film was deposited was reasonably between 30 % and 60 %. As shown in Figure 4.27 the humidity has a range that prevents the formation of a homogeneous film, which occurs instead for humidity values lower than 5%. Since it was not possible to reduce the laboratory humidity or perform the deposition inside a controlled atmosphere glovebox, an additional heating treatment at 60° for 1 hour immediately after the deposition was performed for every sample.

Another factor that should not be excluded as a possible cause of the non-uniformity of the layer is the low percentage of dissolved PVDF. The use of the spin-coating technique, however, seems to maintain in the deposited layer a certain regular dispersion of the PVDF agglomerates as well as of the TiO_2 microparticles, confirming it still as a reliable technique to produce reproducible samples.

From the WCA analysis shown in Figure 4.27 it is possible to state that the WCAs are stable after 60 s and that they take uniform values over the sample. More importantly, thanks to the higher crystallinity of samples, WCAs insist at values ~20° higher than that reported from the producer [103].

The work presented so far provides many ideas for investigations aimed at achieving the stated goals of improving energy collection. Unfortunately, the block imposed by the COVID-19 emergency has clearly interrupted the experimental work in the most productive phase of this study. By comparing those results with literature, it was tried to obtain useful indications to suitably direct the work of the experimental investigation which, hopefully, will be able to resume without too many constraints in the months to come. In identifying the next improvements, future work will focus on:

- Improved film thickness measurement. Despite equipment for thin film thickness measurements is expensive, there are alternative possibilities, which can be pursued in the future, given the possibility of exploiting the PVDF deposited on the glass part of the substrate. Indeed, the thickness can be related to the absorption coefficient, through the formula [123]:

$$a_{SC} = \frac{1}{d}\left(\frac{2\pi(n_f - n_a)\sigma_{rms}}{\lambda}\right)$$

  where a_{SC} is the absorption coefficient, σ_{rms} the average surface roughness, n_f and n_a the refraction coefficients of material and air, respectively, and d the film thickness. This will allow us in the future, with simple absorption and AFM measurements, to measure the thickness of deposited films.
- Improved control of ambient humidity. A key factor, left to a good approximation stable but uncontrolled, is the humidity during deposition and evaporation of PVDF films. Indeed, as mentioned earlier, water has a major effect on the surface morphology of the layers. Moisture control in this respect will be regulated by injections of inert gas (nitrogen) into glovebox until the desired value is reached.
- Improvement of electrical properties by means of TiO_2 nanoparticles. Another possible future development is the introduction of TiO_2 nanoparticles and/or other oxides to replace the microparticles used so far. The motivation is since the addition of microparticles in a polymer matrix raises the relative dielectric constant ε while at the same time lowering the breakdown voltage [118]. This is due to the aggregation of the oxide particles which distort and amplify local electric fields, inducing a reduction of the breaking strength. The lowering of this value is not conducive to the need to use layers that are as thin as possible, which is why the move to nanoparticles allows us to mitigate this problem to some extent. In fact, given their size and the predominant effect of the role of the interface, the distorting effects of the local electric field are considerably mitigated [117].

4.3 VEH Results

In parallel with the improvements to the instrumentation apparatus, I was involved in the testing phase of new materials and technologies for the preparation of the top electrodes, namely those covered with the dielectric layer. As regards the dielectric layer, micrometer-thick sheets of various fluoropolymers were used, a list of which is given in Table 4.13 – List of purchased fluoropolymeric thin films, along with their thickness.:

Material	**Supplier**	**Thickness [μm]**
Fluorinated Ethylene Propylene (FEP)	Teflon FEP (DuPont)	25, 50, 76
Poly Vinylidene Fluoride (PVDF)	SOLEF (Solvay)	25
Ethylene CloroTriFluoroEthylene (ECTFE)	HALAR (Solvay)	8.25, 25

Table 4.13 – List of purchased fluoropolymeric thin films, along with their thickness.

On these systems, various attempts have been made to deploy a conductive layer to act as an electrode:

1) Spraying of commercial conductive coatings (graphite, copper)
2) Al thermal evaporation
3) Au deposition via RF Magnetron Sputtering

For the application of conductive layers, commercial spray lacquers based on graphite and copper were purchased. The first attempts at deposition were unsuccessful: the high hydrophobicity of the fluoropolymer surface limited interaction with the spray lacquers, preventing good adhesion at the fluoropolymer/conductive coating interface (instead of spreading evenly over the fluoropolymer, the lacquer merely formed isolated droplets on it). I solved this problem by applying a simple pre-treatment used in the paint industry: to improve the adhesion between a paint and the application surface, the roughness of the latter is increased. Attempts were made both by hand and with lapping machines, using abrasive paper, and once this was done, the conductive coating was applied.

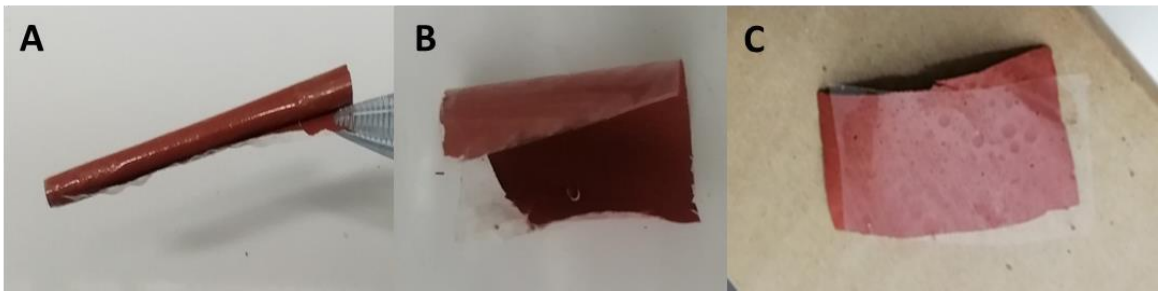

Figure 4.28 – Examples of Fluorinated Ethylene Propylene (FEP, 25 um) covered with conductive coating. A and B correspond to stable adhesion, C to unstable one.

Examples of the result obtained are shown in Figure 4.28. Increasing the surface corrugation by lapping made the adhesion stable, as shown in A, B. In C, an example of detachment of the coating from the fluoropolymer can be seen once the lacquer has been applied, its solvent evaporates, and this leads to tension at the interface between the fluoropolymer and

the lacquer, which contracts. This effect is also visible for the samples shown in Figure 4.28A and Figure 4.28 B (in A, it is so intense that the coating, as it contracts, wraps around itself as if it were a cigar, but the adhesion was so stable that the fluoropolymer behaved in the same manner), but in C, there was a detachment between the coating and fluoropolymer because more of the coating was applied than in samples A and B. However, due to the mechanical brittleness of the coatings, as well as its unsatisfactory electrical transport properties, the energy harvesting properties of these electrodes were not investigated further.

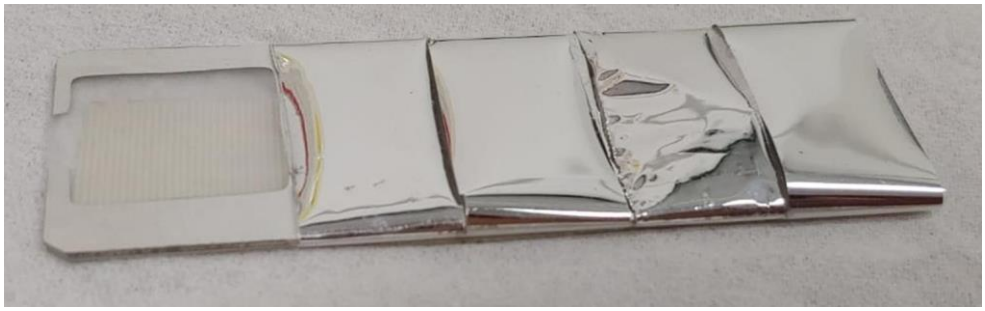

Figure 4.29 – Samples of fluoropolymer films on which aluminum deposition was made. From left to right: ECTFE (25 µm), PVDF (25 µm), ECTFE (8 µm), FEP (25 µm).

By means of an aluminium hot filament vacuum deposition system, aluminium films were deposited on the three types of fluoropolymers described in Table 4.13.

The adhesion at the interface fluoropolymer/aluminium layer deposited was satisfactory from the mechanical point of view, however, problems due to the chemical instability of the aluminium layer did not allow its use in the measurement phase.

In addition to these attempts, gold (about 80 nm) was deposited via RF Magnetron Sputtering on FEP with a thickness of 25 µm, the result of which is shown in Figure 4.32:

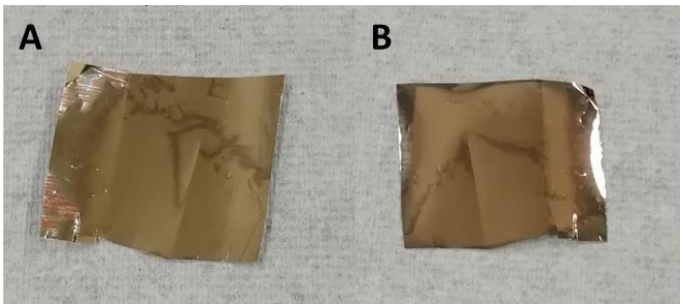

Figure 4.30 – FEP (25 µm) covered in Au deposited via RF Magnetron Sputtering. In A) is shown the fluoropolymer side, in B) the side showing the Au deposition.

From this system, an electrode was obtained, and its energy harvesting properties were measured by REWoD using both the old acquisition method (e.g., measuring the voltage signal at the output of the oscilloscope to estimate the power transferred to the load) and the new automated acquisition system.

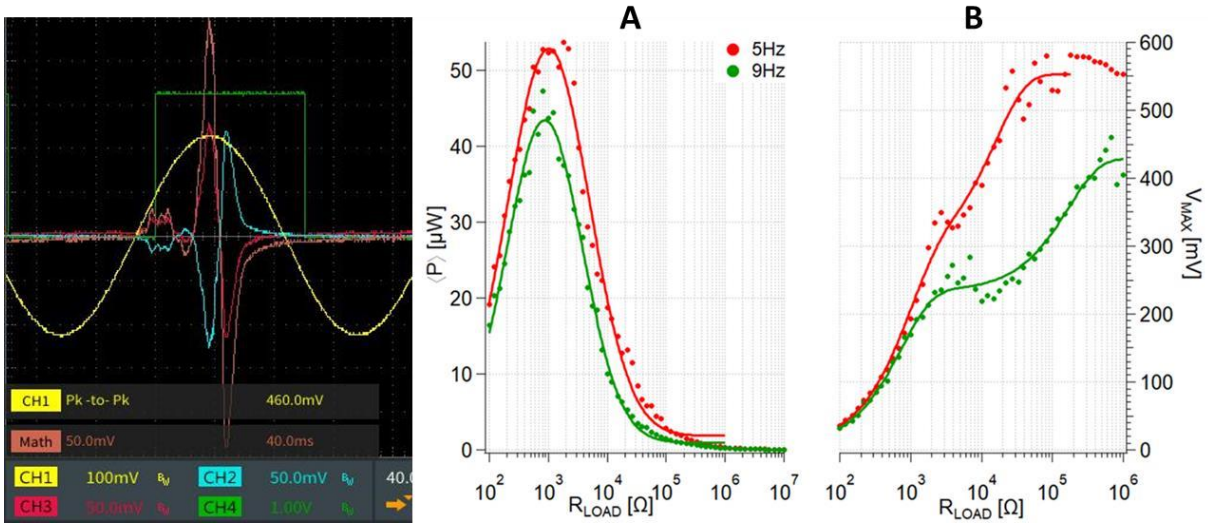

Figure 4.31 – Left panel: open circuit voltage image of the open circuit voltage measured with the FEP/Au electrode with 50uL of deionized water at 5 Hz oscillation, with the old acquisition system. The yellow channel expresses the extent of the shaker's stroke, the red and blue channels the potential at the top and bottom electrode respectively, the salmon-pink channel represents the difference between the red channel and the blue channel, i.e., the potential difference across the resistor load. On the right, graph A and B are shown, which represent respectively the average power transferred to the load as a function of the resistance for two different excitation frequencies, and the respective output voltage values, obtained with FEP/Au and a 10 µl of saturated solution. The LiCl saturation condition refers to the maximum molarity at RT (about 19.6 M).

An example of the experimental output obtained with this system is shown on the right in Figure 4.31. It can be observed that around 1 kΩ there is a power transfer to the load of about 52 uW and 44 uW, for frequencies of 5 Hz and 9 Hz respectively. Considering the droplet size of 10 ul, corresponding to a contact area of 0.4 cm^2, the generated powers become 130 uW/cm^2 (5 Hz) and 110 uW/cm^2 (9 Hz).
The data were analysed using Igor Pro v8.0. The maximum output voltage and the average power as a function of R_{LOAD} are respectively fitted with a double exponential decay and with the lognormal distribution function, which makes it possible to determine a Gaussian-shaped peak in the presence of a logarithmic x-axis. The continuous line curves indicate the fits performed.

Article	Year	Average power calculated for µl of eletrolyte and relative R_{Load}	Average power calculated for cm^2 of eletrolyte and relative R_{Load}
Electrical power generation by mechanically modulating electrical double layers. [28]	2013	1.5 nW (10 MΩ)	0.3 µW (10MΩ)
Water-solid surface contact electrification and its use for harvesting wave energy. [124]	2013	/	5 µW (88 MΩ)
Ionic liquid based vibrational energy harvester by periodically squeezing the liquid bridge [30]	2014	0.8 nW (30 MΩ)	12 nW (30 MΩ)
Contact Electrification and Energy Harvesting using periodically contacted and squeezed water droplets. [125]	2015	3.5 nW (100 MΩ)	/
Liquid-FEP-based U-tube triboelectric nanogenerator for harvesting water-wave energy. [126]	2018	2.0 nW (1 MΩ)	/
3-Dimensional broadband energy harvester based on internal hydrodynamic oscillation with a package structure. [52]	2015	/	2.65 µW (200 MΩ)
Exponential energy harvesting through repetitive reconfigurations of a system of capacitors. [60]	2018	10 nW (1 MΩ)	/
A study of sustainable green current by the fluid based triboelectric nanogenerator (FluTENG) with a comparison of contatct and sliding mode. [54]	2017	/	212 nW (21 KΩ)
FEP (25 um) / LiCl a saturazione (10 µL)	**2019**	**5.2 uW (1KΩ, 5Hz) 4.4 uW (1KΩ, 9Hz)**	**130 µW (1kΩ, 5 Hz) 110 µW (1 kΩ, 9 Hz)**

Table 4.14: Comparison of the most relevant results in literature for fluid-based VEH (without external pre-polarization bias voltage). Last line reports the results obtained in this study.

This is a very good result when compared to what has been published so far in the literature (a list of the most interesting results for systems like ours is given in Table 4.13). A possible reason explaining such result is a thinning of the fluoropolymer in contact with the liquids placed on the electrodes has occurred, thus causing a considerable thinning of the FEP layer compared to the declared one of 25 µm.

4.3.1 PVDF coated electrode with LiCl aqueous solutions at different concentration

The first case presented uses a 10 µl drop of 0.2 M LiCl as the electrolyte.

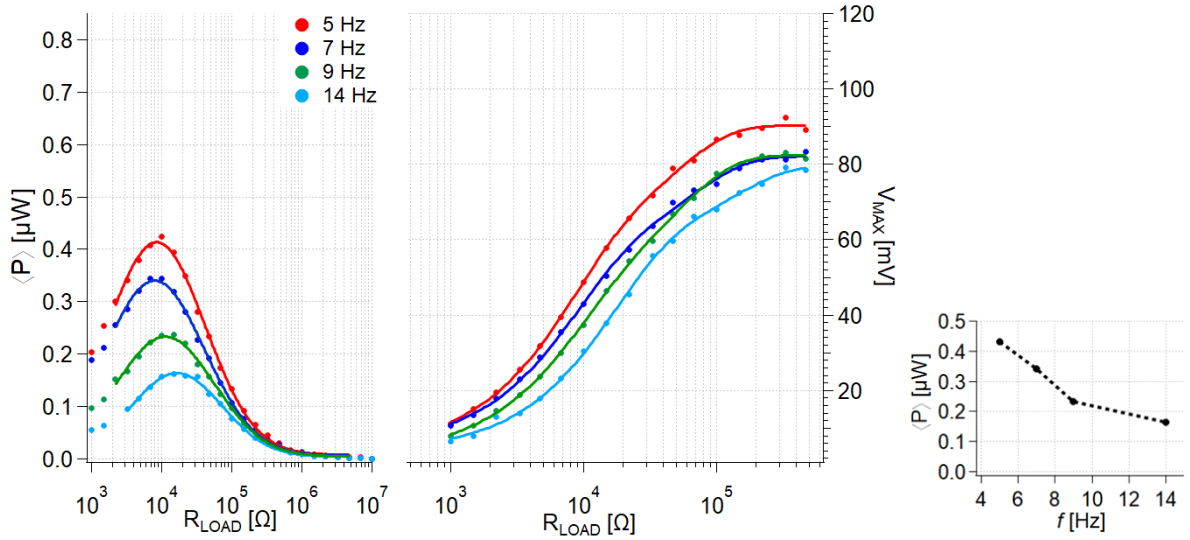

Figure 4.32 – Graph of the average power (left panel), the corresponding average output voltage (central panel) vs. the load resistance R_{LOAD} generated by a 10 µl drop of LiCl at 0.2 M at different excitation frequencies. In right panel, the maximum of the average power generated as a function of excitation frequency.

From the left panel in Figure 4.32 it is possible to see that the average power transferred to the load resistance had its maximum at about 10 kΩ. The highest value obtained was around 0.4 W at the frequency of 5Hz and decreases as the frequency increases, as shown in the right panel of Figure 4.32. The voltage corresponding to the maximum applied load resistance (10 MΩ) is also considered in the following as open circuit voltage and is between 80-90 mV. At maximum power transfer, the generated voltage decreases to 30-50 mV.

The second case presented uses a 10 µl drop of 0.5 M LiCl as the electrolyte.

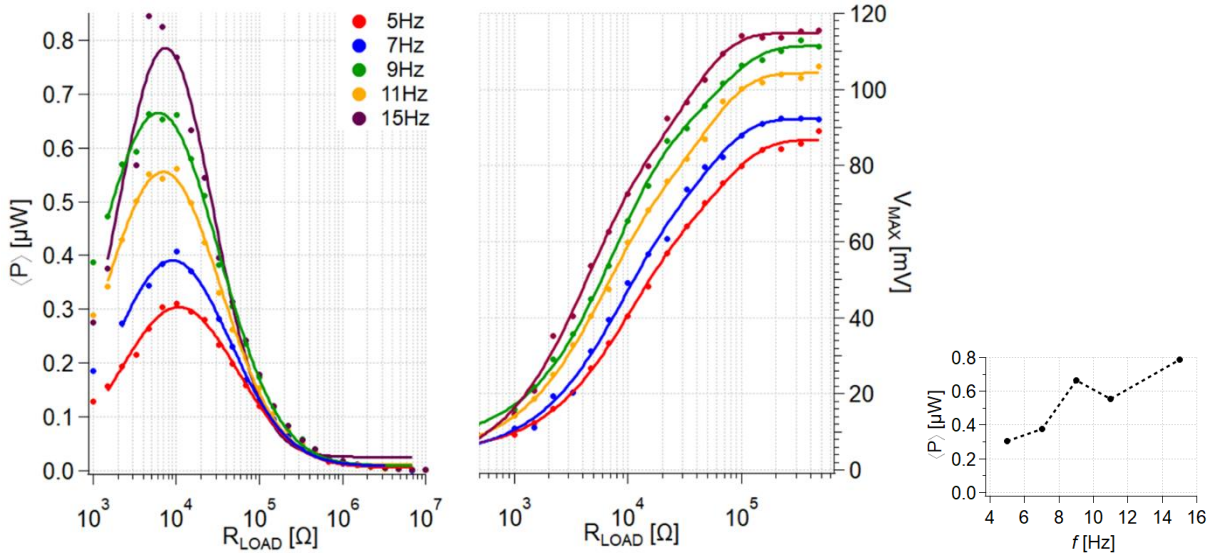

Figure 4.33 – Graph of the average power (left panel), the corresponding output voltage (central panel) as a function of the load resistance R_{LOAD} generated by a 10 µl drop of LiCl at 0.5 M at different excitation frequencies. In right panel, the maximum of the average power generated as a function of excitation frequency.

From the average power graph (Figure 4.35), it can be seen that it has its maximum at about 10 kΩ for all curves. The highest value of the power maximum is around 0.8 W at the frequency of 15 Hz and decreases as the frequency increases, as shown in Figure. The open circuit voltage is between 90 and 120 mV. At maximum power transfer, the generated voltage decreases to 40 -70 mV.

The third case presented uses a 10 µl drop of 2.0 M LiCl as the electrolyte.

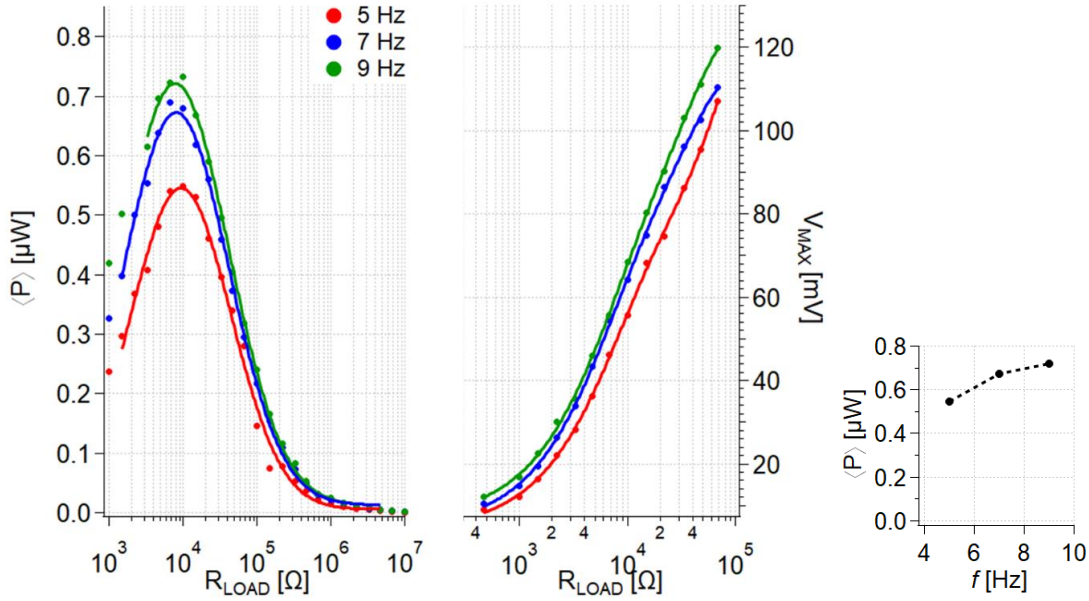

Figure 4.34 – Graph of the average power (left panel), the corresponding output voltage (central panel) as a function of the load resistance R_{LOAD} generated by a 10 µl drop of LiCl at 2 M at different excitation frequencies. In right panel, the maximum of the average power generated as a function of excitation frequency.

From the average power graph (Figure 37), it has its maximum at about 10 k for all curves. The highest value of the power maximum is around 0.7 W at the frequency of 9 Hz and decreases as the frequency increases, as shown in Figure 38. The open circuit voltage is between 110 and 130 mV. At maximum power transfer, the generated voltage decreases to 50-70 mV.

A further measurement with liquid electrolyte, 10 µl of a saturated LiCl solution was used, which, according to the literature, corresponds to a concentration at RT of 19.4 M.
From the right panel of Figure 4.35 it has its maximum at about 30 kΩ but shows a more complex trend as the frequency increases. The highest value of the power maximum is around 0.6 µW at the frequency of 14 Hz and decreases away from it, as shown in Figure 40. The open circuit voltage is between 40 and 180 mV. At maximum power transfer, the generated voltage decreases to 25-125 mV.

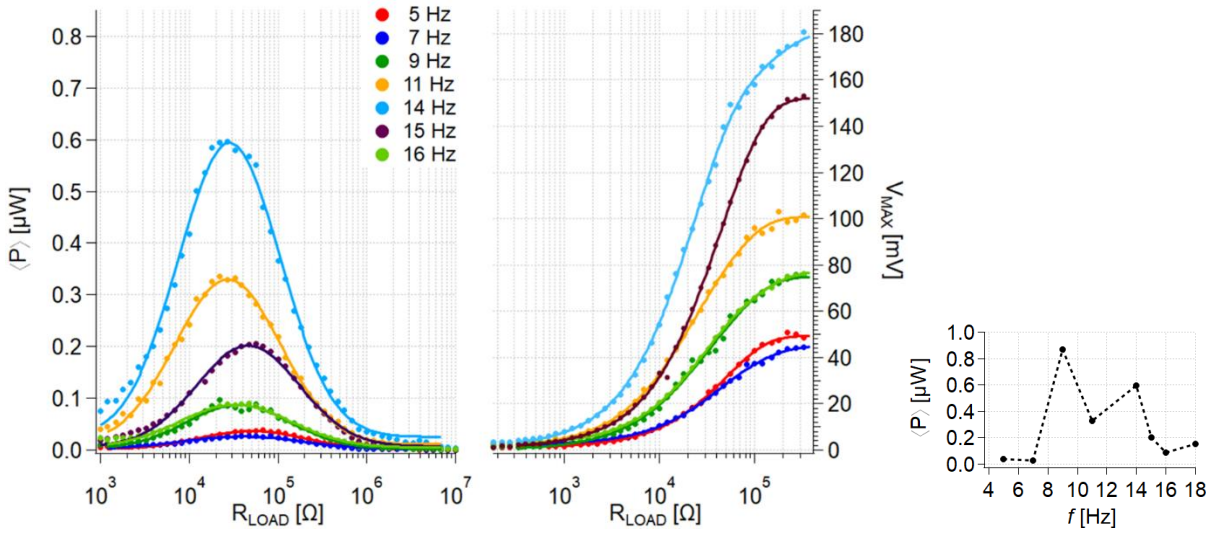

Figure 4.35 - Graph of the average power (left panel), the corresponding output voltage (central panel) as a function of the load resistance R_{LOAD} generated by a 10 µl drop of a saturated LiCl solution at different excitation frequencies. In right panel, the maximum of the average power generated as a function of excitation frequency.

4.3.2 PVDF coated electrode with PAAm hydrogel loaded with LiCl 6.5 M aqueous solution

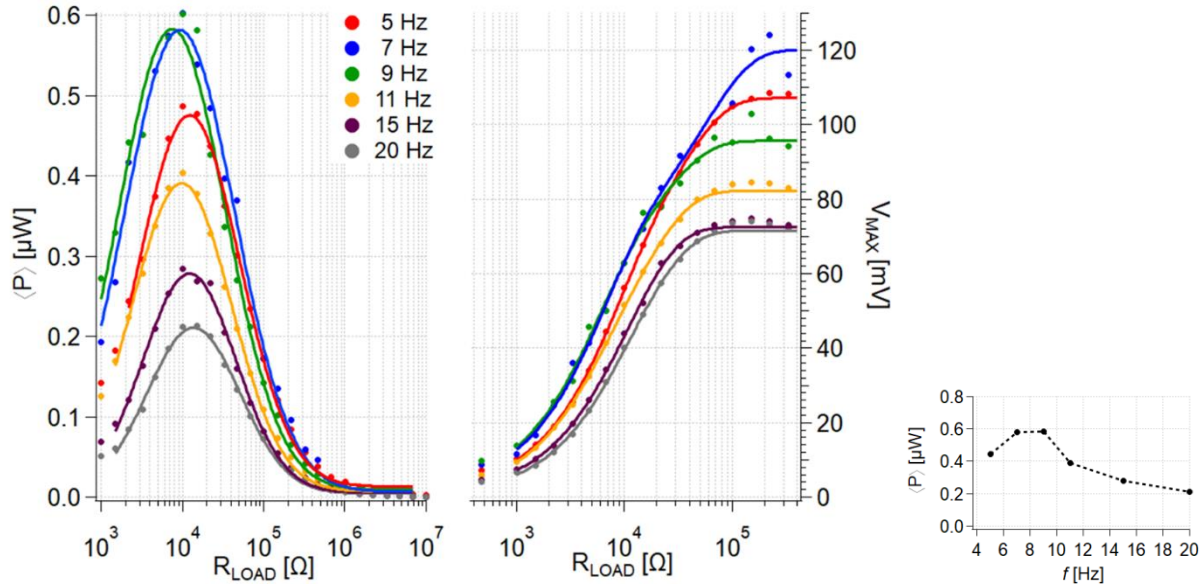

Figure 4.36 - Graph of the average power (left panel), the corresponding output voltage (central panel) as a function the load resistance R_{LOAD} generated by a PAAm hydrogel loaded with LiCl 6.5M at 60 °C for different excitation frequencies. In right panel, the maximum of the average power generated as a function of excitation frequency.

Figure 4.36 shows VEH performance for a PAAm hydrogel swollen in a 6.5 M LiCl solution at 60 °C. From left panel it is possible to see that the average power has its maximum is of 0.6 µW at about 10 kΩ at the frequency of 7-9 Hz, and then it decreases in a regular manner as the frequency increases, as shown in the right panel. The open circuit voltage is between 70 and 120 mV. At maximum power transfer, the generated voltage decreases to 40-70 mV.

4.4 Discussion

The Ph.D. activity took place within the framework of a wider project aimed at developing materials for energy harvesting from low-frequency vibrations (< 100 Hz) using the REWoD principle. In particular, the following activities were carried:

- ✓ With a view to using low-cost industrial materials for energy harvesting from low-frequency vibrations by REWOD, some commercial fluoropolymers (FEP and PVDF) were used as a possible dielectric layer of the device, exploiting their hydrophobic and dielectric properties.
- ✓ Different PVDF films were deposited by spin coating, which are highly hydrophobic with contact angles between 111° and 142°.
- ✓ In all cases, good power values of the order of W were obtained, comparable with those reported in the literature for other systems and with those measured in the same laboratory with microstructured superhydrophobic aluminium electrodes.
- ✓ Very interesting results were obtained with corrugated FEP with a reduced thickness compared to the initial 25 µm, which need further investigation.
- ✓ The use of a commercial hydrogel (PAAm) loaded with LiCl at high molarity shows an improved frequency response.
- ✓ As described by EDL theory, the capacity of the metal-electrolyte interface increases with the concentration of the latter. This seems to be true up to a certain concentration beyond which the maximum achievable power decreases (PVDF). As the concentration of the solution increases, interactions between the ions, between ions and solvent molecules and steric hindrance effects must also be considered, which have a strong dependence on surface charge density, ion valence and size, and concentration. These correlations are very important and can influence the distribution of ions at the electrolyte-solution interface and its thickness (of the EDL itself). In the case of the FEP film, where a strong reduction in thickness is assumed, this dominates the system response.

5 Perspectives and conclusions

Due to the limitations on the activities experienced due to the Covid19 pandemic, some activities have been interrupted and are presented below as possible future developments and suggestions for the continuation of the activity.

5.1 Perspectives

I foresee the following directions to improve the development of VEH devices:

1) To improve the surface wettability of the electrodes by direct electrospinning of PVDF

An innovative perspective is to use electrospinning to deposit a thin layer of PVDF-based non-woven fabric directly on the electrodes, exploiting the high hydrophobicity given by the so obtained morphology [127]. In this additive manufacturing (AM) technique, a jet of polymeric material is spun on a target by a high intensity electric field, forming a network of polymeric fibres ranging from the nanoscale to microscale depending on the deposition parameters. A scheme of the electrospinning setup is shown in Figure 5.1.

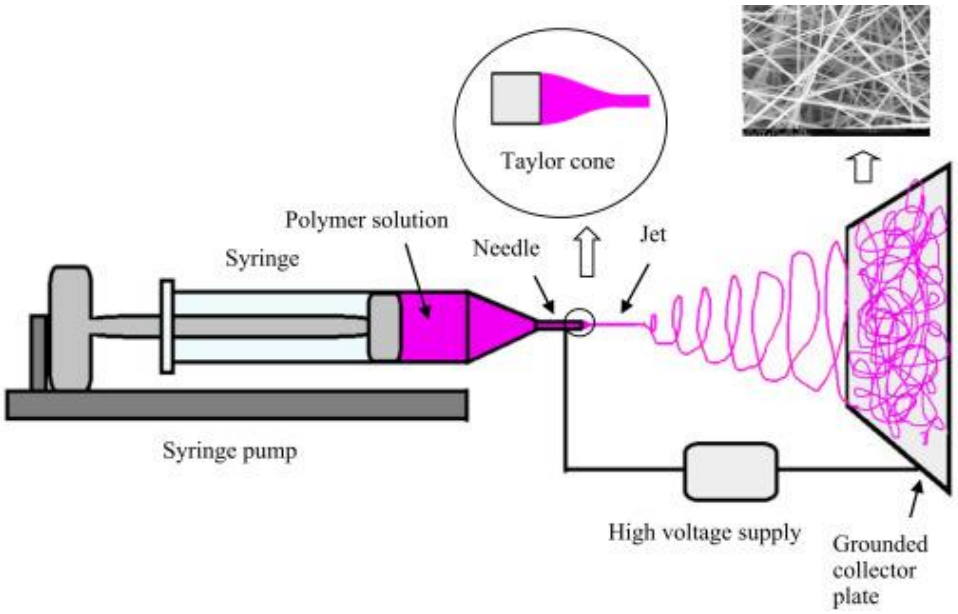

Figure 5.1 – Scheme of the electrospinning setup [128].

A laboratory grade electrospinning setup has been developed and it is shown in Figure 5.2

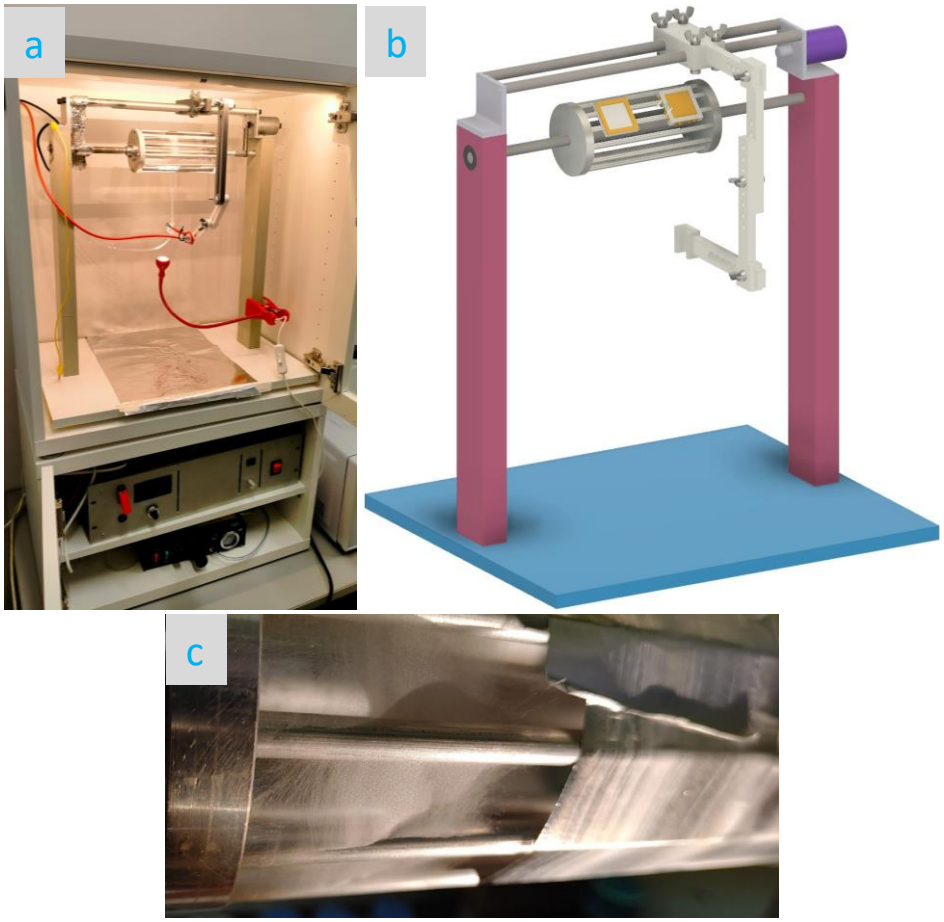

Figure 5.2 – Picture (a), Scheme (b) of the home-made electrospinning apparatus. A detail of the fibre collector (c) with PVDF fibres on aluminium foil. With the correct lighting, the layer of fibres formed between the collector bars on the sides of the aluminium foil is visible.

The electrospinning system includes:

- a fibre collector consisting of a cylindrical aluminium cage that can rotate at up to 1000 rpm
- a voltage generator up to 30 kV, connected to the needle (positive pole) and the collector (ground)
- a syringe pump unit, with the syringe connected to the needle by means of a flexible PTFE tube

This configuration allows the production of large-area non-woven tissue (25x17 cm^2) with uniform deposition of the fibres, which can be aligned by exploiting the speed of rotation up to 1000 rpm. This configuration is flexible because it allows the use of smaller samples (up to 3x3 cm^2), by means of interlocking supports designed and manufactured ad hoc through 3D printing. The use of these supports makes it possible to use targets of a size suitable for the measurement and characterisation techniques previously used, avoiding handling procedures that could damage the film. They can be easily detached from the cage without deforming soft substrates and it can be positioned with orientation parallel or perpendicular to the axis of rotation. They have been designed to produce a thin layer of fibres adhering to the substrate to create an alternation of fibres aligned at 90°.

A preliminary test has been performed with PVDF/DMSO solution. The PVDF solution, 8 wt%, was obtained by dissolving the polymer powders with a mixture of DMSO/acetone in a 6:4 ratio in volume, with LiCl (0.45 wt%), at 70 °C for 30 minutes, followed by degassing at room temperature for 2 hours [129].

Several samples were made by varying the electrospinning parameters until the optimal ones were found, (10 kV, d = 10 cm) allowing for proper deposition, as shown in Figure 5.2(c). The low rotation speed (100 rpm) of the cylindrical cage allows obtaining uniform samples as for a static target.

The morphology of the so obtained sample was studied with the electron microscope to determine the average diameter of the fibres, which was found to be sub-micrometric (800-1000 nm), as shown in Figure 5.3.

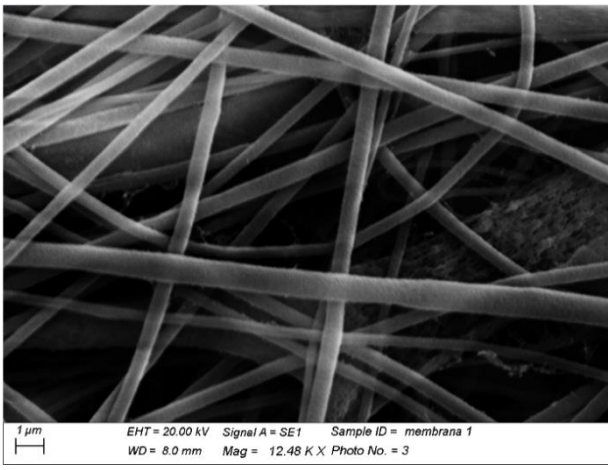

Figure 5.3 – Morphology of electrospun PVDF fibers. The size of the fibers is a few hundred nm.

From WCA measurements, reported in Figure 5.4, a contact angle of about 145° is determined, which is significantly greater than that observed for the samples deposited by spin-coater, due to the right combinations of surface chemistry and topology [130].

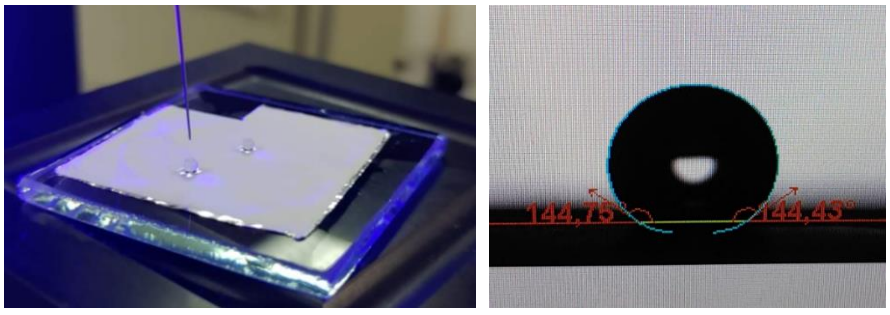

Figure 5.4 – Measurement of the contact angle of the electrospun PVDF layer on aluminium.
The square shape of the sample is due to the use of the adapter system for mounting the slip ring.

2) To improve the VEH prototype

An improved version of the sealed VEH prototype is under development. The relative 2D schematics and images of partially assembled device are shown in Figure 5.5. With respect to previous version (see 3.3.3), in this new device the oscillating mass is connected using a softer and larger spring with has a better response at the working frequencies.

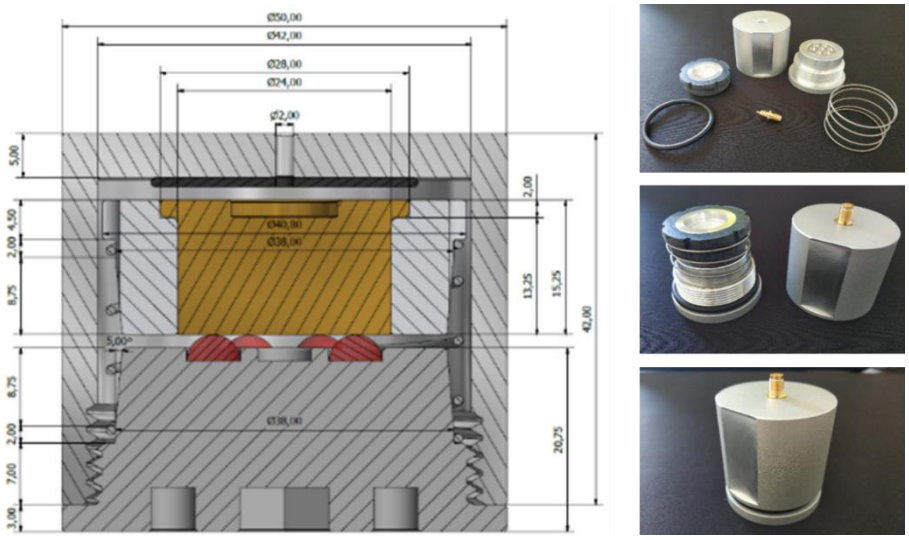

Figure 5.5 – Improved VEH prototype: 2D cross-section diagram, disassembled, partially assembled and mounted prototype.

3) To improve electrodes by use of PCB

A further improvement is to develop a setup for exploiting VEH devices base on PVDF, deposited by spin coating or electrospinning directly on commercial grade printed circuit board (PCB) electrodes. To investigate that possibility an upgrade of the VEH measurement setup has been performed (see Figure 5.6A) and a PCB compatible with the spin coater inside glovebox (to control humidity) and with the electrospinning apparatus has been developed (see Figure 5.6B). The size of such PCB is set to fit inside small portable devices. A gold surface finish (ENIG) has been used for a better passivation of the PCB copper layer (thickness 35 µm).

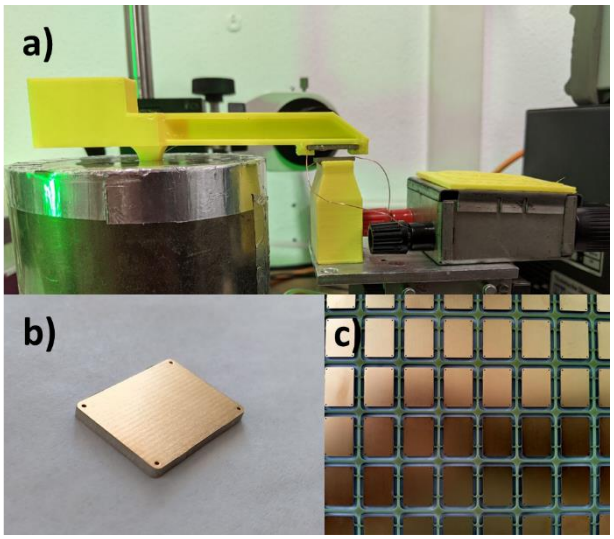

Figure 5.6 – A) Upgraded VEH measurements setup with 3D printed electrodes support and transmission beam. B) Gold-plated ENIG PCB electrode with size 20 mm x 15 mm.

5.2 Conclusions

This PhD activity is in the field of energy harvesting from renewable sources. Recently proposed techniques for capacitive EH from fluids, such as Reverse ElectroWetting-on-Dielectric (ReWoD), were exploited to develop a device for VEH at low frequency, suitable for powering low consumption wearable electronics and for environmental EH. To do so, commercially available, and low-cost materials were investigated. The output power of fluid-based VEH devices is mainly ruled by the properties of the dielectric layer in contact with the fluid, namely thickness, dielectric constant, and hydrophobicity. It was decided to directly exploit Al oxide surfaces, tuning their properties by means of a chemical treatment: this choice is unprecedented in literature, as far as I know, since EH from fluids, such as liquid droplets or hydrogels, has been generally investigated by coating electrodes with fluoropolymers, or by coupling dielectric and fluoropolymers layers. The first part of my activity has been focused on the characterization of Al oxide based electrodes for VEH. Chemical etching induces a surface micro-texturization, which generates a dielectric layer thicker than natural Al passivation layer, and at the same time strongly enhances hydrophobic behaviour. For those samples, by means of microscopic as well as spectroscopic characterization, the hydrophobic behaviour has been related to surface morphological and compositional properties.

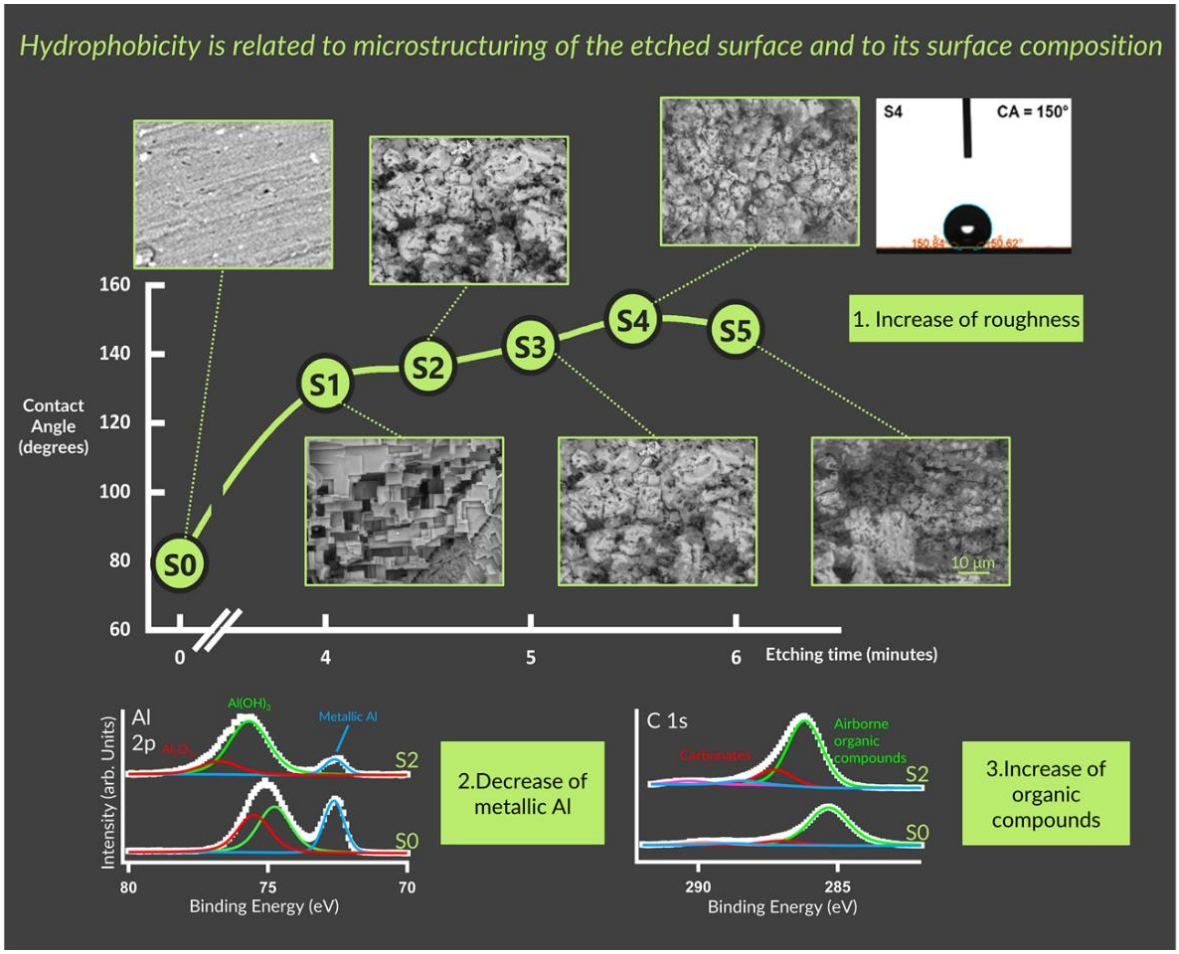

Figure 5.7 – (1) Graphic of relationship between wettability behaviour and morphological properties for S_0-S_5 samples. Below, XPS spectra showing the comparison between untreated (S_0) and treated (S_2) samples, showing a decrease of metallic Al component (2) and an increase in organic compounds (3) at the surface.

In Figure 5.7 a schematic overview of the experimental results expressing the relationship between hydrophobic behaviour and morphological (upper panel) and compositional (lower panels) properties of the chemically treated Al samples. Such characterization allowed to conclude that:

1. The morphological changes, due to chemical etching, turns aluminium surfaces from naturally hydrophilic up to the lower limit of superhydrophobicity (WCA=150°), related to a transition from a Cassie-Baxter to a Wenzel wettability state.
2. The hydrophobicity anti-correlates with the relative amount of metallic Al and is also favoured by the adsorption of organic compounds onto the oxide surface from the surrounding atmosphere.

This electrode has been tested for VEH using a specific standalone setup developed for this purpose, shown in Figure 5.8 A, using commercial PAAm hydrogels, loaded with several saline solutions at different molarities, as electrolyte. Such device was able to generate the power output shown in Figure 5.8 B as a function of the load resistance with 3 hydrogels loaded simultaneously.

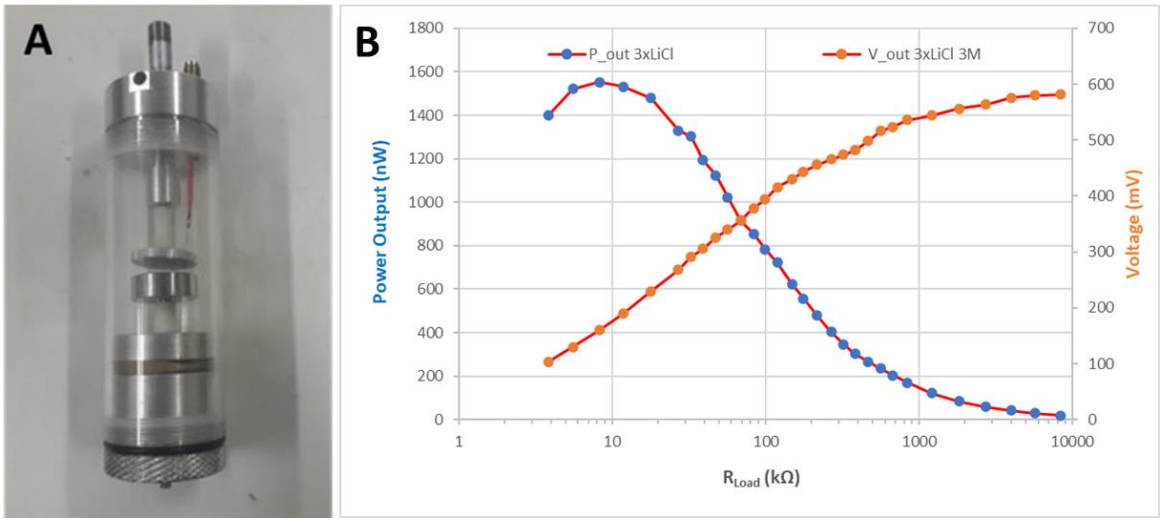

Figure 5.8 – A) Air-tight VEH prototype. B) Experimental output power as a function of R_L, measured with 3 hydrogels loaded with a solution of LiCl (3 M) at 60 °C.

This VEH prototype has a great potential for further applications, but its lifetime is limited by the hydrogel degradation due the prolongated friction with such micro-structured electrodes. To overcome this limitation an alternative electrode coated with PVDF has been developed and investigated. In Figure 5.9, the electrical power output as a function of load resistance is shown for three different electrolytes: aqueous LiCl solution at 0.2 M concentration (panel A) and at saturation (around 19M) (panel B), and with PAAm hydrogel loaded with LiCl at 6.5 M (panel C).

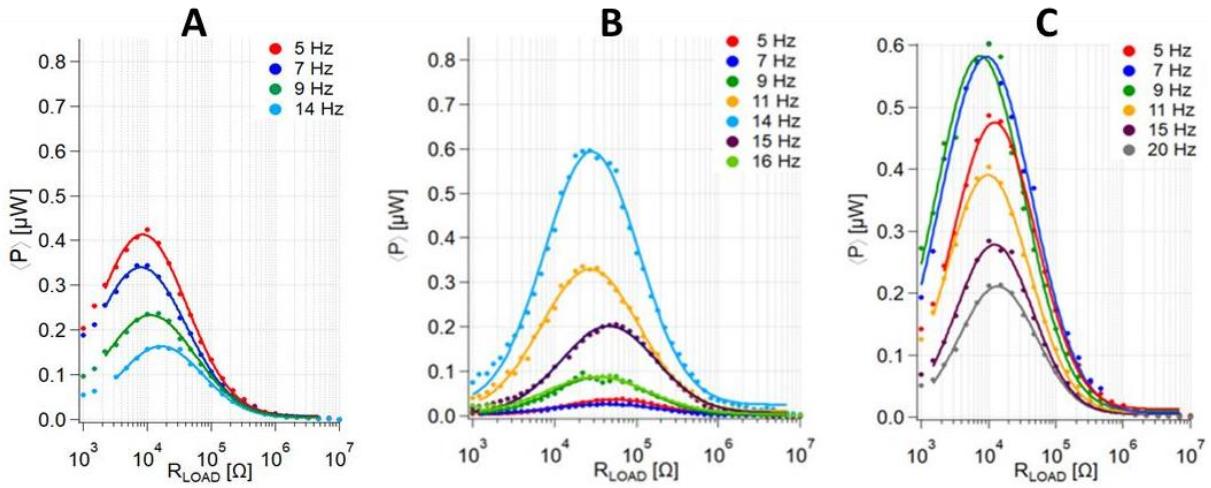

Figure 5.9 – Experimental graphs of the average power output for various oscillation frequencies.

These results show that the maximum average power transferred to the load is approximately 600 nW, both using the drops of aqueous LiCl solution at high concentration and using the hydrogels loaded with aqueous salt solution, allowing to conclude that:

1) The use of hydrogel allows to harvest vibrational energy with an internal resistance of 10^4 Ω, significantly lower than reported in the literature, allowing for a higher power generation, and enabling at the same time a better integration into electronic devices.

2) The thermal treatment applied to the hydrogel at 6.5 M strongly reduces water evaporation, thus increasing the VEH lifetime, enabling its use in real life devices.

3) This power generation fits the needs of several small electronic components, thus enabling its use in self-powered sensors, such as accelerometer suitable for WSN and wearable devices.

4) The very low frequency, typical of human movement, of the harvested mechanical vibrations covers a range not easily accessible to other VEH techniques.

6 Bibliography

[1] I. Akyildiz, “Wireless Sensor Networks: A Survey,” *Computer Networks,* vol. 38, pp. 393-422, 2002.

[2] V. Kempe, “Inertial MEMS,” 2009.

[3] L. Mateu and F. Moll, “Review of energy harvesting techniques and applications for microelectronics,” June 2005.

[4] S. Dey, D. Roy, S. Patra and T. Santra, “Performance of a modified magnetostrictive energy harvester in mechanical vibration,” *Heliyon,* vol. 5, p. e01135, January 2019.

[5] Z. L. Wang, “Triboelectric Nanogerators (TENG)- Sparking an Energy and Sensor Revolution,” *Adv. Energy Mater.,* 2020.

[6] Z. L. Wang and A. C. Wang, “On the origin of contact-electrification,” *Materials Today,* vol. 30, p. 34–51, November 2019.

[7] C. Xu, Y. Zi, A. C. Wang, H. Zou, Y. Dai, X. He, P. Wang, Y.-C. Wang, P. Feng, D. Li and Z. L. Wang, “On the Electron-Transfer Mechanism in the Contact-Electrification Effect,” *Advanced Materials,* vol. 30, p. 1706790, March 2018.

[8] S. Lin, L. Xu, A. C. Wang and Z. L. Wang, “Quantifying electron-transfer in liquid-solid contact electrification and the formation of electric double-layer,” *Nature Communications,* vol. 11, January 2020.

[9] O. Stern, “Zur Theorie der Elektrolytischen Doppelschicht.,” *Z Elektrochem, 30,* pp. 508-16, 1924.

[10] D. C. Grahame, “The Electrical Double Layer and the Theory of Electrocapillarity.,” *Chemical Reviews,* vol. 41, p. 441–501, December 1947.

[11] J. O. BOCKRIS, M. A. V. DEVANATHAN and K. MÜLLER, “ON THE STRUCTURE OF CHARGED INTERFACES,” *Proceedings of the Royal Society of London. Series A. Mathematical and Physical Sciences,* vol. 274, p. 832–863, June 1965.

[12] Shahzeb, “Extended Stern Model,” *Journal of Applied Solution Chemistry and Modeling,* 2012.

[13] G. Lippmann, “Relation entre les phenomenes electriques et capillaries.,” *Annales De Chimie Et De Physique,* vol. 5, p. 494–549, 1875.

[14] G. Beni and S. Hackwood, “Electro-wetting displays,” *Applied Physics Letters,* vol. 38, p. 207–209, 1981.

[15] F. Mugele and J.-C. Baret, “Electrowetting: from basics to applications,” *Journal of Physics: Condensed Matter,* vol. 17, p. R705–R774, July 2005.

[16] B. Berge, “Electrocapillarity and wetting of insulator films by water,” *Comptes Rendus Acad. Sci.,* 1993.

[17] C. Quilliet and B. Berge, “Electrowetting: A recent outbreak,” *Curr. Opin. Colloid Interface Sci.,* vol. 6, p. 34–39, 2001.

[18] Y.-P. Zhao and Y. Wang, “Fundamentals and Applications of Electrowetting,” *Reviews of Adhesion and Adhesives,* vol. 1, p. 114–174, February 2013.

[19] J. Berthier, Micro-Drops and Digital Microfluidics, Elsevier Science & Techn., 2008.

[20] B. Berge and J. Peseux, “Variable focal lens controlled by an external voltage: An application of electrowetting,” *The European Physical Journal E,* vol. 3, p. 159–163, October 2000.

[21] T. Krupenkin, S. Yang and P. Mach, “Tunable liquid microlens,” *Applied Physics Letters,* vol. 82, p. 316–318, January 2003.

[22] S.-K. Fan, H. Yang and W. Hsu, “Droplet-on-a-wristband: Chip-to-chip digital microfluidic interfaces between replaceable and flexible electrowetting modules,” *Lab Chip,* vol. 11, p. 343–347, 2011.

[23] H. You and A. J. Steckl, “Three-color electrowetting display device for electronic paper,” *Applied Physics Letters,* vol. 97, p. 023514, July 2010.

[24] V. Srinivasan, V. K. Pamula and R. B. Fair, “An integrated digital microfluidic lab-on-a-chip for clinical diagnostics on human physiological” *Lab on a Chip,* vol. 4, p. 310, 2004.

[25] A. R. Wheeler, H. Moon, C.-J. \. Kim, J. A. Loo and R. L. Garrell, “Electrowetting-Based Microfluidics for Analysis of Peptides and Proteins by Matrix-Assisted Laser Desorption/Ionization Mass Spectrometry,” *Analytical Chemistry,* vol. 76, p. 4833–4838, July 2004.

[26] D. M. Ratner, E. R. Murphy, M. Jhunjhunwala, D. A. Snyder, K. F. Jensen and P. H. Seeberger, “Microreactor-based reaction optimization in organic chemistry—glycosylation as a challenge,” *Chem. Commun.,* p. 578–580, 2005.

[27] T. Krupenkin and J. A. Taylor, “Reverse electrowetting as a new approach to high-power energy harvesting,” *Nature Communications,* vol. 2, August 2011.

[28] J. K. Moon, J. Jeong, D. Lee and H. K. Pak, “Electrical power generation by mechanically modulating electrical double layers,” *Nature Communications,* vol. 4, February 2013.

[29] J. K. Moon, M. W. Song and H. K. Pak, “Investigation of surface charge density on solid–liquid interfaces by modulating the electrical double layer,” *Journal of Physics: Condensed Matter,* vol. 27, p. 194102, April 2015.

[30] W. Kong, P. Cao, X. He, L. Yu, X. Ma, Y. He, L. Lu, X. Zhang and Y. Deng, “Ionic liquid based vibrational energy harvester by periodically squeezing the liquid bridge,” *RSC Adv.,* vol. 4, p. 19356–19361, 2014.

[31] J. J. Segura, A. Elbourne, E. J. Wanless, G. G. Warr, K. Voïtchovsky and R. Atkin, *Adsorbed and near surface structure of ionic liquids at a solid interface,* vol. 15, Royal Society of Chemistry (RSC), 2013, p. 3320.

[32] Q. Jiang, H. Barkan, A. Menner and A. Bismarck, “Micropatterned, macroporous polymer springs for capacitive energy harvesters,” *Polymer,* vol. 126, p. 419–424, September 2017.

[33] C. Zhong, Y. Deng, W. Hu, J. Qiao, L. Zhang and J. Zhang, “A review of electrolyte materials and compositions for electrochemical supercapacitors,” *Chemical Society Reviews,* vol. 44, p. 7484–7539, 2015.

[34] R. Li, K. Zhang, L. Cai, G. Chen and M. he, “Highly stretchable ionic conducting hydrogels for strain/tactile sensors,” *Polymer,* vol. 167, p. 154–158, March 2019.

[35] J.-Y. Sun, C. Keplinger, G. M. Whitesides and Z. Suo, “Ionic skin,” *Advanced Materials,* vol. 26, p. 7608–7614, October 2014.

[36] X. Wu, G. Li and D.-W. Lee, “A novel energy conversion method based on hydrogel material for self-powered sensor system applications,” *Applied Energy,* vol. 173, p. 103–110, July 2016.

[37] X. Wu, G. Li and D. W. Lee, “A hydrogel-based energy harvester with broad bandwidth driven by ambient vibrations,” *Transducers, 2015, Alaska,* June 2015.

[38] G. Allegretto, “INVESTIGATION OF AQUEOUS DROPLET-BASED ELECTROSTATIC TRANSDUCTION,” *University of British Columbia,* November 2017, DOI:10.14288/1.0355200.

[39] G. Allegretto, Y. Dobashi, K. Dixon, J. Wyss, D. Yao and J. D. W. Madden, “Frequency domain analysis of droplet-based electrostatic transducers,” in *Smart Materials and Structures*, 2018.

[40] A. G. Banpurkar, Y. Sawane, S. M. Wadhai, C. U. Murade, I. Siretanu, D. van den Ende and F. Mugele, “Spontaneous electrification of fluoropolymer–water interfaces probed by electrowetting,” *Faraday Discussions,* vol. 199, p. 29–47, 2017.

[41] Z. L. Wang, J. Chen and L. Lin, “Progress in triboelectric nanogenerators as a new energy technology and self-powered sensors,” *Energy & Environmental Science,* vol. 8, p. 2250–2282, 2015.

[42] Z.-H. Lin, G. Cheng, S. Lee, K. C. Pradel and Z. L. Wang, “Harvesting Water Drop Energy by a Sequential Contact-Electrification and Electrostatic-Induction Process,” *Advanced Materials,* vol. 26, p. 4690–4696, May 2014.

[43] S. Niu, Y. Liu, S. Wang, L. Lin, Y. S. Zhou, Y. Hu and Z. L. Wang, “Theoretical Investigation and Structural Optimization of Single-Electrode Triboelectric Nanogenerators,” *Advanced Functional Materials,* vol. 24, p. 3332–3340, February 2014.

[44] Y. Yang, G. Zhu, H. Zhang, J. Chen, X. Zhong, Z.-H. Lin, Y. Su, P. Bai, X. Wen and Z. L. Wang, “Triboelectric Nanogenerator for Harvesting Wind Energy and as Self-Powered Wind Vector Sensor System,” *ACS Nano,* vol. 7, p. 9461–9468, September 2013.

[45] Q. Liang, X. Yan, Y. Gu, K. Zhang, M. Liang, S. Lu, X. Zheng and Y. Zhang, *Highly transparent triboelectric nanogenerator for harvesting water-related energy reinforced by antireflection coating,* vol. 5, Springer Science and Business Media LLC, 2015.

[46] H. Guo, J. Chen, M.-H. Yeh, X. Fan, Z. Wen, Z. Li, C. Hu and Z. L. Wang, *An Ultrarobust High-Performance Triboelectric Nanogenerator Based on Charge Replenishment,* vol. 9, American Chemical Society (ACS), 2015, p. 5577–5584.

[47] H. Guo, Q. Leng, X. He, M. Wang, J. Chen, C. Hu and Y. Xi, “A Triboelectric Generator Based on Checker-Like Interdigital Electrodes with a Sandwiched PET Thin Film for Harvesting Sliding Energy in All Directions,” *Advanced Energy Materials,* vol. 5, p. 1400790, August 2014.

[48] S. Wang, S. Niu, J. Yang, L. Lin and Z. L. Wang, *Quantitative Measurements of Vibration Amplitude Using a Contact-Mode Freestanding Triboelectric Nanogenerator,* vol. 8, American Chemical Society (ACS), 2014, p. 12004–12013.

[49] M. Mariello, F. Guido, V. M. Mastronardi, M. T. Todaro, D. Desmaële and M. D. Vittorio, “Nanogenerators for harvesting mechanical energy conveyed by liquids,” *Nano Energy,* vol. 57, p. 141–156, March 2019.

[50] Z. L. Wang, T. Jiang and L. Xu, “Toward the blue energy dream by triboelectric nanogenerator networks,” *Nano Energy,* vol. 39, p. 9–23, September 2017.

[51] Q. Shi, H. Wang, H. Wu and C. Lee, “Self-powered triboelectric nanogenerator buoy ball for applications ranging from environment monitoring to water wave energy farm,” *Nano Energy,* vol. 40, p. 203–213, October 2017.

[52] S.-B. Jeon, D. Kim, M.-L. Seol, S.-J. Park and Y.-K. Choi, "3-Dimensional broadband energy harvester based on internal hydrodynamic oscillation with a package structure," *Nano Energy,* vol. 17, p. 82–90, October 2015.

[53] X. Zhang, Y. Zheng, D. Wang and F. Zhou, "Solid-liquid triboelectrification in smart U-tube for multifunctional sensors," *Nano Energy,* vol. 40, p. 95–106, October 2017.

[54] S. A. Nahian, R. K. Cheedarala and K. K. Ahn, "A study of sustainable green current generated by the fluid-based triboelectric nanogenerator (FluTENG) with a comparison of contact and sliding mode," *Nano Energy,* vol. 38, p. 447–456, August 2017.

[55] W.-S. Jung, M.-G. Kang, H. G. Moon, S.-H. Baek, S.-J. Yoon, Z.-L. Wang, S.-W. Kim and C.-Y. Kang, "High Output Piezo/Triboelectric Hybrid Generator," *Scientific Reports,* vol. 5, March 2015.

[56] Hassan, "A flat-panel-shaped hybrid piezo/triboelectric nanogenerator for ambientenergy harvesting," *nanotechnology,* vol. 28, p. 175402, April 2017.

[57] X. Wang, Z. Wen, H. Guo, C. Wu, X. He, L. Lin, X. Cao and Z. L. Wang, "Fully Packaged Blue Energy Harvester by Hybridizing a Rolling Triboelectric Nanogenerator and an Electromagnetic Generator," *ACS Nano,* vol. 10, p. 11369–11376, November 2016.

[58] D. Jiang, Y. Su, K. Wang, Y. Wang, M. Xu, M. Dong and G. Chen, "A triboelectric and pyroelectric hybrid energy harvester for recovering energy from low-grade waste fluids," *Nano Energy,* vol. 70, p. 104459, April 2020.

[59] J. Yu, E. Ma and T. Ma, "Harvesting energy from low-frequency excitations through alternate contacts between water and two dielectric materials," *Scientific Reports,* vol. 7, December 2017.

[60] J. Yu, E. Ma and T. Ma, "Exponential energy harvesting through repetitive reconfigurations of a system of capacitors," *Communications Physics,* vol. 1, March 2018.

[61] D. Paul, ICT - Energy Concepts for Energy Efficiency and Sustainability, Erscheinungsort nicht ermittelbar: IntechOpen, 2017.

[62] P.-G. de Gennes, F. Brochard-Wyart and D. Quéré, *Capillarity and Wetting Phenomena,* Springer New York, 2004.

[63] T. Onda, S. Shibuichi, N. Satoh and K. Tsujii, "Super-Water-Repellent Fractal Surfaces," *Langmuir,* vol. 12, p. 2125–2127, January 1996.

[64] Y. Gu, W. Zhang, J. Mou, S. Zheng, L. Jiang, Z. Sun and E. Wang, "Research progress of biomimetic superhydrophobic surface characteristics, fabrication, and application," *Advances in Mechanical Engineering,* vol. 9, p. 168781401774685, December 2017.

[65] L. E. Helseth, "The Influence of Microscale Surface Roughness on Water-Droplet Contact Electrification," *Langmuir,* June 2019.

[66] C. Vargel, Corrosion of aluminium, Amsterdam Boston: Elsevier, 2004.

[67] A. M. Abyzov, "Aluminum Oxide and Alumina Ceramics (review). Part 1. Properties of Al2O3 and Commercial Production of Dispersed Al2O3," *Refractories and Industrial Ceramics,* vol. 60, p. 24–32, May 2019.

[68] P. Moazzam, G. Luciano, A. Razmjou, E. Akbari, P. G. Ul'yanov and S. Mahanty, "Effect of molecular-scale surface energy alteration of aluminium on its corrosion resistance behaviour," *Colloids and Surfaces A: Physicochemical and Engineering Aspects,* vol. 562, p. 26–33, February 2019.

[69] Z. Chen, Y. Guo and S. Fang, “A facial approach to fabricate superhydrophobic aluminum surface,” *Surface and Interface Analysis,* p. n/a–n/a, 2009.

[70] L. Savio, K. B. Bhavitha, G. Bracco, G. Luciano, D. Cavallo, G. Paolini, S. Passaglia, G. Carraro, L. Vattuone, R. Masini and M. Smerieri, “Correlating hydrophobicity to surface chemistry of microstructured aluminium surfaces,” *Applied Surface Science,* vol. 542, p. 148574, March 2021.

[71] M. Ran, W. Zheng and H. Wang, “Fabrication of superhydrophobic surfaces for corrosion protection: a review,” *Materials Science and Technology,* vol. 35, p. 313–326, January 2019.

[72] A.-M. Kietzig, S. G. Hatzikiriakos and P. Englezos, “Patterned Superhydrophobic Metallic Surfaces,” *Langmuir,* vol. 25, p. 4821–4827, March 2009.

[73] S. Barthwal, Y. S. Kim and S.-H. Lim, “Mechanically Robust Superamphiphobic Aluminum Surface with Nanopore-Embedded Microtexture,” *Langmuir,* vol. 29, p. 11966–11974, September 2013.

[74] A. Suri, A. Pratt, S. Tear, C. Walker, C. Kincal, U. Kamber, O. Gurlu and M. El-Gomati, “Analysis and detection of low-energy electrons in scanning electron microscopes using a Bessel box electron energy analyser,” *Journal of Electron Spectroscopy and Related Phenomena,* vol. 241, p. 146823, May 2020.

[75] K. U. O. WINSON C. H., M. A. R. T. H. A. BRICENO and D. O. G. A. N. OZKAYA, “Characterisation of Catalysts Using Secondary and Backscattered Electron In-lens Detectors,” *Platinum Metals Review,* vol. 58, p. 106–110, April 2014.

[76] N. Smith, “Science with Soft X Rays,” *Physics Today,* vol. 54, p. 29–34, January 2001.

[77] W. Zhao, S. M. Kozlov, O. Höfert, K. Gotterbarm, M. P. A. Lorenz, F. Viñes, C. Papp, A. Görling and H.-P. Steinrück, “Graphene on Ni(111): Coexistence of Different Surface Structures,” *The Journal of Physical Chemistry Letters,* vol. 2, p. 759–764, March 2011.

[78] unknown, “No Title, (n.d.). https://www.makeitfrom.com/material-group/AA-6000-Series-Aluminum-Magnesium-Silicon-Wrought-Alloy,” n.d..

[79] J. Long, M. Zhong, H. Zhang and P. Fan, “Superhydrophilicity to superhydrophobicity transition of picosecond laser microstructured aluminum in ambient air,” *Journal of Colloid and Interface Science,* vol. 441, p. 1–9, March 2015.

[80] C. Powell, "X-ray Photoelectron Spectroscopy Database XPS,Version 4.1, NIST Standard Reference Database 20," 1989.

[81] S.-L. Chang, J. W. Anderegg and P. A. Thiel, “Surface oxidation of an Al□Pd□Mn quasicrystal, characterized by X-ray photoelectron spectroscopy,” *Journal of Non-Crystalline Solids,* vol. 195, p. 95–101, February 1996.

[82] M. W. R. A.F. Carley, “An X-ray photoelectron spectroscopic study of the interaction of oxygen and nitric oxide with aluminium,” *Proceedings of the Royal Society of London. A. Mathematical and Physical Sciences,* vol. 363, p. 403–424, November 1978.

[83] P. Marcus, C. Hinnen and I. Olefjord, “Determination of attenuation lengths of photoelectrons in aluminium and aluminium oxide by angle-dependent x-ray photoelectron spectroscopy,” *Surface and Interface Analysis,* vol. 20, p. 923–929, October 1993.

[84] X. P. S. Thermo Scientific, *https://xpssimplified.com/elements/aluminum.php,* 2015.

[85] J. R. Lindsay, H. J. Rose, W. E. Swartz, P. H. Watts and K. A. Rayburn, “X-Ray Photoelectron Spectra of Aluminum Oxides: Structural Effects on the \textquotedblleftChemical Shift\textquotedblright,” *Applied Spectroscopy,* vol. 27, p. 1–5, January 1973.

[86] J. A. Rotole and P. M. A. Sherwood, “Corrundum (α-Al2O3) by XPS,” *Surface Science Spectra,* vol. 5, p. 11–17, January 1998.

[87] C. Sun, R. Zeng, J. Zhang, Z.-J. Qiu and D. Wu, “Effects of UV-Ozone Treatment on Sensing Behaviours of EGFETs with Al2O3 Sensing Film,” *Materials,* vol. 10, p. 1432, December 2017.

[88] H. Piao and N. S. McIntyre, “Adventitious carbon growth on aluminium and gold-aluminium alloy surfaces,” *Surface and Interface Analysis,* vol. 33, p. 591–594, 2002.

[89] C. T. Campbell and M. T. Paffett, “The interactions of O2, CO and CO2 with Ag(110),” *Surface Science,* vol. 143, p. 517–535, August 1984.

[90] L. Savio, A. Gerbi, L. Vattuone, R. Pushpa, N. Bonini, S. de Gironcoli and M. Rocca, “Subsurface Oxygen Stabilization by a Third Species: Carbonates on Ag(210),” *The Journal of Physical Chemistry C,* vol. 111, p. 10923–10930, June 2007.

[91] A. J. Kinloch, Adhesion and Adhesives, Springer Netherlands, 2012.

[92] P. M. A. Sherwood, “Introduction to Studies of Phosphorus-Oxygen Compounds by XPS,” *Surface Science Spectra,* vol. 9, p. 62–66, December 2002.

[93] Y. Marcus, “Effect of ions on the structure of water,” *Pure and Applied Chemistry,* vol. 82, p. 1889–1899, June 2010.

[94] O. Y. Samoilov, “A new approach to the study of hydration of ions in aqueous solutions,” *Discussions of the Faraday Society,* vol. 24, p. 141, 1957.

[95] “R. W. Gurney. Ionic Processes in Solution, McGraw-Hill, New York (1953).”.

[96] https://www.solvay.com/en/chemical-categories/specialty-polymers.

[97] G. J. Puts, P. Crouse and B. M. Ameduri, “Polytetrafluoroethylene: Synthesis and Characterization of the Original Extreme Polymer,” *Chemical Reviews,* vol. 119, p. 1763–1805, January 2019.

[98] W. Xia and Z. Zhang, “PVDF-based dielectric polymers and their applications in electronic materials,” *IET Nanodielectrics,* vol. 1, p. 17–31, April 2018.

[99] D. C. Bassett, Developments in Crystalline Polymers-1, Dordrecht: Springer Netherlands, 1982.

[100] S. P. S. Satapathy and K. B. R. Varma, “Crystallization of Beta-phase Poly (vinylidene fluoride) films using dimethyl sulfoxide (DMSO) solvent and at suitable annealing condition”.

[101] X. Cai, T. Lei, D. Sun and L. Lin, “A critical analysis of the alpha, beta and gamma phases in poly(vinylidene fluoride) using FTIR,” *RSC Advances,* vol. 7, p. 15382–15389, 2017.

[102] P. Martins, A. C. Lopes and S. Lanceros-Mendez, “Electroactive phases of poly(vinylidene fluoride): Determination, processing and applications,” *Progress in Polymer Science,* vol. 39, p. 683–706, April 2014.

[103] “https://www.solvay.com/sites/g/files/srpend221/files/2018-08/Solef-PVDF-Design-and-Processing-Guide_EN-v2.7_0.pdf.”.

[104] C. Ribeiro, C. M. Costa, D. M. Correia, J. Nunes-Pereira, J. Oliveira, P. Martins, R. Gonçalves, V. F. Cardoso and S. Lanceros-Méndez, “Electroactive poly(vinylidene fluoride)-based structures for advanced applications,” *Nature Protocols,* vol. 13, p. 681–704, March 2018.

[105] N. Sahu, B. Parija and S. Panigrahi, “Fundamental understanding and modeling of spin coating process: A review,” 2009.

[106] J. Danglad-Flores, S. Eickelmann and H. Riegler, “Deposition of polymer films by spin casting: A quantitative analysis,” *Chemical Engineering Science,* vol. 179, p. 257–264, April 2018.

[107] R. Y. Albena Lederer, “Analytical methods for polymer characterization,” *Analytical and Bioanalytical Chemistry,* vol. 410, p. 4773–4774, May 2018.

[108] P. Pages, “Characterization of polymer materials using FT-IR and DSC techniques.,” pp. https://ruc.udc.es/dspace/bitstream/handle/2183/11499/CC-80%20art%208.pdf, 2005.

[109] B. Mahale, D. Bodas and S. A. Gangal, “Study of β-phase development in spin-coated PVDF thick films,” *Bulletin of Materials Science,* vol. 40, p. 569–575, June 2017.

[110] J. Liu, X. Lu and C. Wu, “Effect of Preparation Methods on Crystallization Behavior and Tensile Strength of Poly(vinylidene fluoride) Membranes,” *Membranes,* vol. 3, p. 389–405, November 2013.

[111] J. Rinaldo Gregorio and M. Cestari, “Effect of crystallization temperature on the crystalline phase content and morphology of poly(vinylidene fluoride),” *Journal of Polymer Science Part B: Polymer Physics,* vol. 32, p. 859–870, April 1994.

[112] https://www.effemm2.de/spectragryph/about_descr_hist.html.

[113] Fortunato, Cavallini, D. Bellis, Marra, Tamburrano, Sarto and Sarto, “Phase Inversion in PVDF Films with Enhanced Piezoresponse Through Spin-Coating and Quenching,” *Polymers,* vol. 11, p. 1096, June 2019.

[114] A. J. Kinloch and R. J. Young, “Crystalline Polymers,” p. 324–369, 1995.

[115] S. M. Aqeel, Z. Wang, L. Than, G. Sreenivasulu and X. Zeng, “Poly(vinylidene fluoride)/poly(acrylonitrile) – based superior hydrophobic piezoelectric solid derived by aligned carbon nanotubes in electrospinning: fabrication, phase conversion and surface energy,” *RSC Advances,* vol. 5, p. 76383–76391, 2015.

[116] J. R. Gregorio and E. M. Ueno, “Effect of crystalline phase, orientation and temperature on the dielectric properties of poly (vinylidene fluoride)(PVDF),” *Journal of Materials Science,* vol. 34, p. 4489–4500, 1999.

[117] P. Barber, S. Balasubramanian, Y. Anguchamy, S. Gong, A. Wibowo, H. Gao, H. Ploehn and H.-C. Z. Loye, “Polymer Composite and Nanocomposite Dielectric Materials for Pulse Power Energy Storage,” *Materials,* vol. 2, p. 1697–1733, October 2009.

[118] J. Li, S. I. Seok, B. Chu, F. Dogan, Q. Zhang and Q. Wang, “Nanocomposites of Ferroelectric Polymers with TiO2Nanoparticles Exhibiting Significantly Enhanced Electrical Energy Density,” *Advanced Materials,* vol. 21, p. 217–221, January 2009.

[119] S. M. Kramer, I. G. Gorichev, Y. A. Lainer, I. V. Artamonova and M. V. Terekhova, “Calculation of the solubility of TiO2 and titanates in sulfuric acid solutions,” *Russian Metallurgy (Metally),* vol. 2014, p. 704–707, September 2014.

[120] F. Shi, Y. Ma, J. Ma, P. Wang and W. Sun, “Preparation and characterization of PVDF/TiO2 hybrid membranes with different dosage of nano-TiO2,” *Journal of Membrane Science,* vol. 389, p. 522–531, February 2012.

[121] https://data.biotage.co.jp/products/turbovap/tv96_evaporation_rate.pdf.

[122] M. Li, I. Katsouras, C. Piliego, G. Glasser, I. Lieberwirth, P. W. M. Blom and D. M. de Leeuw, “Controlling the microstructure of poly(vinylidene-fluoride) (PVDF) thin films for microelectronics,” *Journal of Materials Chemistry C,* vol. 1, p. 7695, 2013.

[123] A. Poruba, A. Fejfar, Z. Remeš, J. Špringer, M. Vaněček, J. Kočka, J. Meier, P. Torres and A. Shah, "Optical absorption and light scattering in microcrystalline silicon thin films and solar cells," *Journal of Applied Physics,* vol. 88, p. 148–160, July 2000.

[124] Z.-H. Lin, G. Cheng, L. Lin, S. Lee and Z. L. Wang, "Water-Solid Surface Contact Electrification and its Use for Harvesting Liquid-Wave Energy," *Angewandte Chemie International Edition,* vol. 52, p. 12545–12549, October 2013.

[125] L. E. Helseth and X. D. Guo, "Contact Electrification and Energy Harvesting Using Periodically Contacted and Squeezed Water Droplets," *Langmuir,* vol. 31, p. 3269–3276, March 2015.

[126] L. Pan, J. Wang, P. Wang, R. Gao, Y.-C. Wang, X. Zhang, J.-J. Zou and Z. L. Wang, "Liquid-FEP-based U-tube triboelectric nanogenerator for harvesting water-wave energy," *Nano Research,* vol. 11, p. 4062–4073, February 2018.

[127] J. Xue, T. Wu, Y. Dai and Y. Xia, "Electrospinning and Electrospun Nanofibers: Methods, Materials, and Applications," *Chemical Reviews,* vol. 119, p. 5298–5415, March 2019.

[128] S. Y. Quek, J. Hadi and H. Tanambell, "Application of Electrospinning as Bioactive Delivery System," p. 145–149, 2019.

[129] F. Russo, C. Ursino, E. Avruscio, G. Desiderio, A. Perrone, S. Santoro, F. Galiano and A. Figoli, "Innovative Poly (Vinylidene Fluoride) (PVDF) Electrospun Nanofiber Membrane Preparation Using DMSO as a Low Toxicity Solvent," *Membranes,* vol. 10, p. 36, February 2020.

[130] N. Nuraje, W. S. Khan, Y. Lei, M. Ceylan and R. Asmatulu, "Superhydrophobic electrospun nanofibers," *J. Mater. Chem. A,* vol. 1, p. 1929–1946, 2013.

[133] K. A. Abdullah, M. A. Batal, R. Hamdan, T. Khalil, J. Zaraket, M. Aillerie and C. Salame, "The Enhancement of PVDF Pyroelectricity (Pyroelectric Coefficient and Dipole Moment) by Inclusions," *Energy Procedia,* vol. 119, p. 545–555, July 2017.

[134] G. Kalimuldina, N. Turdakyn, I. Abay, A. Medeubayev, A. Nurpeissova, D. Adair and Z. Bakenov, "A Review of Piezoelectric PVDF Film by Electrospinning and Its Applications," *Sensors,* vol. 20, p. 5214, September 2020.

[135] B. Mohammadi, A. A. Yousefi and S. M. Bellah, *Effect of tensile strain rate and elongation on crystalline structure and piezoelectric properties of PVDF thin films,* vol. 26, Elsevier BV, 2007, p. 42–50.

[136] F. Mokhtari, M. Latifi and M. Shamshirsaz, "Electrospinning/electrospray of polyvinylidene fluoride (PVDF): piezoelectric nanofibers," *The Journal of The Textile Institute,* p. 1–19, September 2015.

[137] Z. L. Wang, "Triboelectric Nanogenerator (TENG)—Sparking an Energy and Sensor Revolution," *Advanced Energy Materials,* vol. 10, p. 2000137, March 2020.

[138] C. V. Boys, "On the Production, Properties, and some suggested Uses of the Finest Threads," 1887.

[139] P. R. Adhikari, N. T. Tasneem, R. C. Reid and I. Mahbub, "Electrode and electrolyte configurations for low frequency motion energy harvesting based on reverse electrowetting," *Scientific Reports,* vol. 11, March 2021.

[140] "Adhesion & Adhesives - Science & Technology", A J Kinloch, Chapman & Hall, London, 1987